



Novel nanowire structures and devices for nanoelectronic bioprobes

Citation

Jiang, Zhe. 2015. Novel nanowire structures and devices for nanoelectronic bioprobes. Doctoral dissertation, Harvard University, Graduate School of Arts & Sciences.

Permanent link

<http://nrs.harvard.edu/urn-3:HUL.InstRepos:17467307>

Terms of Use

This article was downloaded from Harvard University's DASH repository, and is made available under the terms and conditions applicable to Other Posted Material, as set forth at <http://nrs.harvard.edu/urn-3:HUL.InstRepos:dash.current.terms-of-use#LAA>

Share Your Story

The Harvard community has made this article openly available.
Please share how this access benefits you. [Submit a story](#).

[Accessibility](#)

Novel nanowire structures and devices for nanoelectronic bioprobes

A dissertation presented

by

Zhe Jiang

to

The Department of Chemistry and Chemical Biology

in partial fulfillment of the requirements

for the degree of

Doctor of Philosophy

in the subject of

Chemistry

Harvard University

Cambridge, Massachusetts

April 2015

© 2015 – Zhe Jiang

All rights reserved.

Novel nanowire structures and devices for nanoelectronic bioprobes

Abstract

Semiconductor nanowire materials and devices provide unique opportunities in the frontier between nanoelectronics and biology. The bottom-up paradigm enables flexible synthesis and patterning of nanoscale building blocks with novel structures and properties, and nano-to-micro fabrication methods allow the advantages of functional nanowire elements to interface with biological systems in new ways. In this thesis, I will focus on the development of bottom-up nanoscience platforms, which includes rational synthesis and assembly of semiconductor nanowires with new capabilities, as well as design and fabrication of the first free-standing three-dimensional (3D) nanoprobes, with special focus on applications in intracellular recording and stimulation.

I will first introduce kinked p-n junction nanowires as a new and powerful family of high spatial resolution biological and chemical sensors with proof-of-concept applications. Next, I will discuss a variety of functional kinked nanowires with synthetically controlled properties and the potential of achieving more detailed and less invasive cellular studies. Furthermore, I will present a general shape-controlled deterministic nanowire assembly method to produce large-scale arrays of devices with well-defined geometry and position.

Then, I will present the design of a general method to fabricate these nanowire structures into free-standing 3D probes. I will show that free-standing nanowire bioprobes can be manipulated to target specific cells and record stable intracellular action potentials. I will demonstrate simultaneous measurements from the same cell using both kinked nanowire and patch-clamp probes. Moreover, I will discuss two strategies of multiplexed recording using free-standing probes.

Finally, I will report localized stimulation on single cells enabled by the unique properties of p-n kinked nanowires. I will show with simulation and electrical characterization that in reverse bias, localized electric field generated around the nanoscale p-n junction should exceed the threshold for opening voltage-gated sodium channels. Moreover, I will present measurements of localized cell stimulation using p-n nanowire free-standing probes. Together with the capability of stable intracellular recording, these results complete the two-way communication between semiconductor nanowire electronics and biological systems at a natural nanoscale, which can open up new directions in the fields ranging from cellular electrophysiology, brain activity mapping to brain-machine interface.

Table of Contents

| | |
|--|-----|
| Abstract | iii |
| Table of Contents | v |
| Acknowledgements | ix |
| List of Figures | xii |
| List of Abbreviations | xiv |
| Chapter 1. Introduction | 1 |
| 1.1 Bottom-up nanowire synthesis: diverse structure and function | 1 |
| 1.2 Nanowire assembly: hierarchical control with precision | 4 |
| 1.3 Nanoelectronics and biology: interfacing at the natural scale | 6 |
| 1.4 Overview of thesis | 12 |
| 1.5 Bibliography | 15 |
| Chapter 2. Kinked p-n junction nanowire probes for high spatial resolution sensing and intracellular recording | 19 |
| 2.1 Introduction | 19 |
| 2.2 Experimental | 20 |
| 2.2.1 Nanowire synthesis | 20 |
| 2.2.2 Device fabrication | 20 |
| 2.2.3 Tip-modulated scanning gate microscopy characterization | 21 |
| 2.2.4 Charged nanoparticle sensing | 21 |
| 2.2.5 Cellular recordings | 22 |
| 2.3 Results and discussion | 23 |
| 2.3.1 Nanowire synthesis and characterization | 23 |
| 2.3.2 Device fabrication and electrical characterization | 24 |
| 2.3.3 Diode sensing analysis | 25 |
| 2.3.4 Kinked p-n junction nanowire sensing characterizations | 28 |
| 2.3.5 Single charged nanoparticle sensing | 30 |

| | | |
|------------|---|----|
| 2.3.6 | Intracellular recordings | 33 |
| 2.4 | Conclusion..... | 35 |
| 2.5 | Bibliography..... | 36 |
| Chapter 3. | Design and synthesis of diverse functional kinked nanowire structures for nanoelectronic bioprobes | 38 |
| 3.1 | Introduction | 38 |
| 3.2 | Experimental | 39 |
| 3.2.1 | Kinked nanowire synthesis | 39 |
| 3.2.2 | KOH selective wet etching | 41 |
| 3.2.3 | Bend-up probe fabrication | 41 |
| 3.2.4 | Device water-gate characterization..... | 42 |
| 3.2.5 | Scanning gate microscopy characterization..... | 42 |
| 3.3 | Results and discussion..... | 43 |
| 3.3.1 | Material designs and potential applications..... | 43 |
| 3.3.2 | Synthesis and characterization of U-shaped kinked nanowires..... | 44 |
| 3.3.3 | Synthesis and characterization of V-shaped kinked nanowires with series nanoFET..... | 48 |
| 3.3.4 | Synthesis and characterization of W-shaped kinked nanowires with parallel nanoFET..... | 51 |
| 3.4 | Conclusion..... | 54 |
| 3.5 | Bibliography..... | 55 |
| Chapter 4. | Shape-controlled deterministic assembly of nanowires..... | 58 |
| 4.1 | Introduction | 58 |
| 4.2 | Experimental | 59 |
| 4.2.1 | Nanowire synthesis | 59 |
| 4.2.2 | Shape-controlled assembly | 60 |
| 4.2.3 | TEM sample preparation and characterization | 61 |
| 4.2.4 | Strain release tests..... | 63 |

| | | |
|--|--|-----|
| 4.2.5 | Raman microscopy characterization | 63 |
| 4.2.6 | Finite element simulation of nanowire bending..... | 63 |
| 4.2.7 | Bend-up nanowire probe arrays..... | 64 |
| 4.2.8 | Nanowire waveguides..... | 65 |
| 4.2.9 | Finite-Difference Time-Domain calculations..... | 65 |
| 4.3 | Results and discussion..... | 66 |
| 4.3.1 | Demonstration of shape-controlled nanowire assembly..... | 66 |
| 4.3.2 | Characterization of assembled nanowires..... | 69 |
| 4.3.3 | Generalization of assembly method..... | 74 |
| 4.3.4 | Wafer-scale assembly..... | 76 |
| 4.3.5 | Applications of assembly technique..... | 77 |
| 4.4 | Conclusion and outlook..... | 81 |
| 4.5 | Bibliography..... | 81 |
| Chapter 5. Free-standing kinked nanowire transistor probes for targeted intracellular recording in three dimensions..... | | 84 |
| 5.1 | Introduction..... | 84 |
| 5.2 | Experimental..... | 85 |
| 5.2.1 | Nanowire synthesis..... | 85 |
| 5.2.2 | Free-standing probe fabrication..... | 86 |
| 5.2.3 | Cardiomyocyte culture..... | 89 |
| 5.2.4 | Patch-clamp recording..... | 90 |
| 5.2.5 | Intracellular recording..... | 90 |
| 5.3 | Results and discussion..... | 91 |
| 5.3.1 | Free-standing probe design..... | 91 |
| 5.3.2 | Fabrication and assembly of free-standing nanowire probes..... | 92 |
| 5.3.3 | Intracellular recording using free-standing nanowire probes..... | 95 |
| 5.3.4 | Multiplexed recording with two nanoFET probes..... | 102 |
| 5.3.5 | Multiplexed recording with W-shaped kinked nanowire probe..... | 104 |

| | | |
|------------|---|-----|
| 5.4 | Conclusion..... | 112 |
| 5.5 | Bibliography..... | 113 |
| Chapter 6. | Kinked p-n junction nanowire probes for localized cell stimulation..... | 115 |
| 6.1 | Introduction..... | 115 |
| 6.2 | Experimental..... | 116 |
| 6.2.1 | Kinked p-n nanowire synthesis..... | 116 |
| 6.2.2 | COMSOL multiphysics simulation..... | 117 |
| 6.2.3 | Free-standing probe fabrication..... | 117 |
| 6.2.4 | CHO cell culture..... | 119 |
| 6.2.5 | Brain slice preparation..... | 119 |
| 6.2.6 | Patch-clamp recording..... | 120 |
| 6.2.7 | Intracellular recording and stimulation..... | 120 |
| 6.2.8 | Confocal imaging..... | 121 |
| 6.3 | Results and discussion..... | 121 |
| 6.3.1 | Kinked p-n junction nanowire for localized stimulation..... | 121 |
| 6.3.2 | Device fabrication and characterization..... | 125 |
| 6.3.3 | Localized stimulation on CHO cells..... | 128 |
| 6.3.4 | Stimulation on voltage sensitive dye modified CHO cells..... | 132 |
| 6.3.5 | Stimulation of neurons..... | 134 |
| 6.4 | Conclusion and outlook..... | 135 |
| 6.5 | Bibliography..... | 136 |

Acknowledgements

The past five years of graduate school at Harvard University has been an amazing intellectual journey to me. Here I would like to express my sincere gratitude to many people who made this journey possible and memorable.

First and foremost, I am deeply grateful to my advisor, Professor Charles M. Lieber, who has supported me with invaluable trust, exceptional guidance, brilliant ideas, constant encouragement and incredible inspiration. I still remember when I first met Professor Lieber in 2009 in Beijing, I was mesmerized by his deep understanding of science and strong enthusiasm for the pursuit of excellence. That was the start of my exploration in the interdisciplinary world of nanoscience and nanotechnology. Professor Lieber is an extraordinary advisor and a great mentor. I greatly appreciate his unwavering faith in my potential and his persistent patience in guiding me through hardest times. I want to thank him for all the opportunities to work on really exciting scientific projects and to learn from him. He taught me through exemplification the principles of critical thinking, hard-working, staying positive, thinking about big pictures and paying close attention to details. These principles have helped me transform into an independent scientist and will benefit me through my whole career.

I would also like to express my sincere gratitude to members of my Graduate Advising Committee, Professor Xiaowei Zhuang, Professor Daniel Nocera and Professor Sunney Xie for their great support, the time they spent discussing my research and the invaluable advice they gave me to achieve my goals.

My sincere gratitude is also due to Dr. Jinlin Huang, for his dedicated support and invaluable advice throughout these years. His expertise made many of my experiments

possible. It is my great pleasure to work with him. His extraordinary insights and consistent help are greatly appreciated.

I would like to acknowledge past and present Lieber group members for their inspiration and collaboration. The work in this thesis would not have been possible without the support of these friends. I would like to thank Prof. Quan Qing, Dr. Lin Xu, Prof. Zhe Yu, Dr. Peter Kruskal, Dr. Jae-Hyun Lee, Sean You, Dr. You-Shin No, Max N. Mankin and Yunlong Zhao for the fruitful collaborations; the many hours of discussion and working together on hard problems have enriched my knowledge in many ways. I would like to express my gratitude to Dr. Thomas J. Kempa and Robert W. Day for their great help and advice on nanowire synthesis. I am also thankful to Prof. Bozhi Tian, Prof. Xiaojie Duan, Prof. Tzahi Cohen-Karni and Ruixuan Gao for teaching me of intracellular nanoprobe and giving me advice. My special thanks also go to Dr. Hao Yan, Dr. Ping Xie, Dr. Xiaocheng Jiang, Dr. Jun Yao, Dr. Yongjie Hu, Prof. SungWoo Nam and Prof. Wooyoung Shim for teaching me of nanowire assembly and nanoelectronics. My sincere thanks are also due to Dr. Lu Wang for her great help in nanoparticle sensing experiments. I am also grateful to Dr. Jia Liu, Dr. Wei Zhou, Prof. Chong Xie, Dr. Ning Gao, Tian-ming Fu, Dr. Zengguang Cheng and Xiaochuan Dai for their great help on experiments and valuable discussion. I would like to thank Prof. James Cahoon, Dr. Hwan Sung Choe, Dr. Steffen Strehle, Dr. Guosong Hong, Tao Zhou and Anqi Zhang for the help and support and for making the lab a better place to work. In addition, I appreciate technical help from Yuan Lu, David Bell, Jiangdong Deng, Ling Xie and other CNS staffs; and also the administrative assistance from Kathleen Ledyard, Renée Donlon and Purvang Patel.

I would like to thank my families who have all contributed not only to my thesis work but also my meaning of life. My deep thanks to my parents for their unconditional love, faith, understanding, support and encouragement. They have made my life happier and more meaningful.

Finally, I am grateful to all of you who have directly or indirectly contributed to the completion of this thesis work. Thanks for all the kind help.

List of Figures

| | |
|--|----|
| Figure 1-1. Schematic of VLS growth of Si nanowires. | 2 |
| Figure 1-2. Schematics of contact printing and nanocombing assembly methods. | 5 |
| Figure 1-3. Nanowires as a new approach to electrophysiology. | 10 |
| Figure 2-1. Design and controlled synthesis of kinked p-n nanowires. | 24 |
| Figure 2-2. Kinked p-n nanowire device characterization. | 25 |
| Figure 2-3. Schematic of diode band diagram under gate potentials. | 26 |
| Figure 2-4. tmSGM and water-gate experiments of kinked p-n nanowire devices. . | 29 |
| Figure 2-5. Fluorescent polystyrene nanobead sensing experiment. | 32 |
| Figure 2-6. Intracellular electrical recording from spontaneously beating chicken cardiomyocytes. | 35 |
| Figure 3-1. Overview of kinked nanowire synthetic designs and potential applications. | 44 |
| Figure 3-2. U-shaped kinked nanowires. | 45 |
| Figure 3-3. Series nanoFET in V-shaped kinked nanowires. | 49 |
| Figure 3-4. SGM characterization of V-shaped kinked nanowires. | 51 |
| Figure 3-5. Parallel nanoFET kinked nanowires. | 53 |
| Figure 4-1. Preparation of TEM samples. | 62 |
| Figure 4-2. Demonstration of shape-controlled nanowire assembly. | 66 |
| Figure 4-3. Occupancy statistics of U-shaped nanowire arrays assembled by PMMA trenches. | 68 |
| Figure 4-4. Characterization of assembled nanowires. | 71 |
| Figure 4-5. Control of assembled nanowire radius of curvature. | 73 |
| Figure 4-6. Generality of shape-controlled nanowire assembly. | 75 |
| Figure 4-7. Wafer-scale assembly. | 77 |
| Figure 4-8. 3D probe arrays. | 78 |
| Figure 4-9. Nanowire optical waveguide. | 80 |

| | |
|--|-----|
| Figure 5-1. Intracellular recording methods. | 92 |
| Figure 5-2. Fabrication of free-standing nanowire probes. | 93 |
| Figure 5-3. Parallel multi-probe fabrication. | 94 |
| Figure 5-4. Assembly of free-standing nanowire probes. | 95 |
| Figure 5-5. Intracellular recording using free-standing nanowire probes. | 96 |
| Figure 5-6. Stability of nanoFET intracellular recording. | 99 |
| Figure 5-7. Full amplitude action potentials and resting potential recorded by nanoFET probes. | 101 |
| Figure 5-8. Ion-channel blocker tests using free-standing nanowire probes. | 102 |
| Figure 5-9. Multiplexed recording with two free-standing nanowire probes. | 104 |
| Figure 5-10. Key steps of fabricating free-standing probes with selected W-shaped Si kinked nanowire. | 105 |
| Figure 5-11. Multiplexed intracellular recording using the free-standing dual-nanoFET probe. | 109 |
| Figure 6-1. p-n junction kinked nanowire for localized stimulation. | 123 |
| Figure 6-2. p-n kinked nanowire freestanding probe characterization. | 127 |
| Figure 6-3. Localized stimulation using p-n kinked nanowire probes on CHO cell. | 129 |
| Figure 6-4. Stimulation on VSD modified CHO cells. | 133 |
| Figure 6-5. Stimulation of neurons. | 135 |

List of Abbreviations

| | |
|-------------|----------------------------------|
| VLS | Vapor-liquid-solid |
| CVD | Chemical vapor deposition |
| PSP | Post-synaptic potential |
| FET | Field-effect transistor |
| PL | Photolithography |
| EBL | Electron-beam lithography |
| CHO | Chinese hamster ovary |
| SEM | Scanning electron microscopy |
| I-V | Current versus voltage |
| SGM | Scanning gate microscopy |
| AFM | Atomic force microscopy |
| FWHM | Full width at half maximum |
| PBS | Phosphate buffer saline |
| S/D | Source/Drain |
| TEM | Transmission electron microscopy |
| FIB | Focused ion beam |
| FDTD | Finite-difference time-domain |
| VSD | Voltage sensitive dye |

Chapter 1. Introduction

Over the past several decades, the advances of nanoscience and nanotechnology have driven revolutionary breakthroughs across physical and life sciences¹⁻⁷. The bottom-up paradigm has been a major contributor due to its advantages in synthesis and assembly of complex nanostructures into unique functional integrated nanodevices beyond the limits of conventional top-down technologies⁸⁻¹⁵. Central to the bottom-up paradigm are three key areas: (1) rational design and synthesis of nanoscale building blocks with controllable composition, structure and corresponding properties, (2) hierarchical assembly methods that can organize nanomaterials into integrated architectures with high density and precision, and (3) design and fabrication of novel functional devices with unique physical properties. Semiconductor nanowires are a versatile family of nanomaterials where all three themes have seen significant development, and have become a powerful platform for both testing of fundamental limits and exploring novel scientific applications in diverse areas ranging from electronics, photonics to biology^{1,2,3,16-20}.

1.1 Bottom-up nanowire synthesis: diverse structure and function

High-quality semiconductor nanowires can be synthesized using a general nanocluster-catalyzed vapor-liquid-solid (VLS) growth method²¹⁻²⁶. In this process (**Fig. 1-1**), the temperature is maintained above the eutectic point of the metal nanocluster to facilitate the formation of a liquid metal/semiconductor droplet with the feeding of a vapor-phase semiconductor source. Continued addition of semiconductor reactant supersaturates the droplet, resulting in nucleation of solid semiconductor along the chemical potential

avored one dimension. The growth continues on the liquid-solid interface which serves as a sink bringing semiconductor material into the formed lattice, while the alloy droplet cap stays on top of the elongating nanowire.

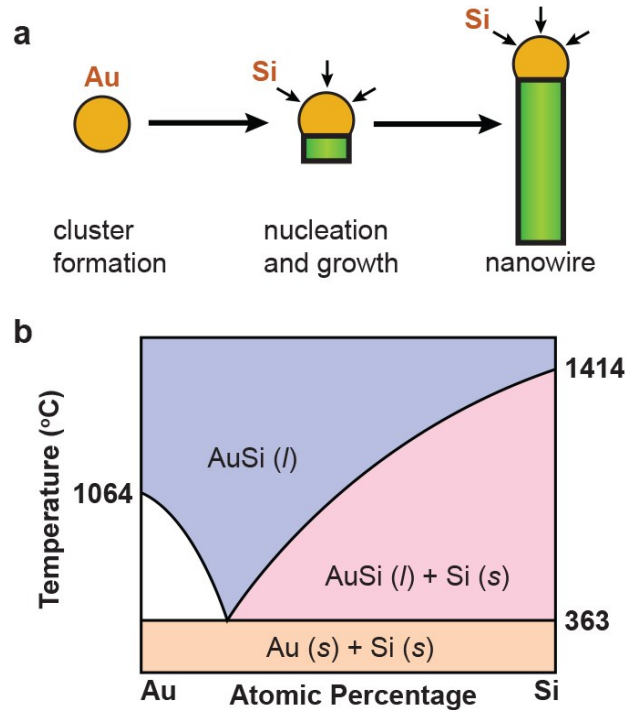


Figure 1-1. Schematic of VLS growth of Si nanowires. **a**, A liquid alloy droplet AuSi is first formed above the eutectic temperature (363 °C) of Au and Si. The continued feeding of Si in the vapor phase into the liquid alloy causes oversaturation of the liquid alloy, resulting in nucleation and directional nanowire growth. **b**, Binary phase diagram for Au and Si illustrating the thermodynamics of VLS growth.

A variety of methods have been explored to generate gaseous semiconductor reactants, including momentum or energy transfer methods such as pulsed laser ablation¹², molecular beam epitaxy (MBE)²³ from solid targets, or the most popular thermal or plasma-enhanced decomposition of precursors such as chemical vapor deposition (CVD) or plasma-enhanced chemical vapor deposition (PECVD) process. In CVD-VLS synthesis, the metal nanocluster acts as both a catalyst to facilitate the decomposition of the gaseous

semiconductor precursor and a growth droplet site. In the case of Si nanowire synthesis (**Fig. 1-1**), Au nanoparticles and silane (SiH_4) are typically used as the catalysts and precursor, respectively^{12,23}. Aside from group IV materials, compound III-V and II-VI nanowires have also been synthesized with the VLS method²⁷, based on the corresponding pseudo-binary phase diagrams of the catalyst and compound semiconductor. To provide the gaseous precursors for compound semiconductor nanowire growth, pulsed laser ablation²⁷ or metal-organic chemical vapor deposition (MOCVD)²⁸ are typically used.

It has been demonstrated in the literature that a variety of semiconductor nanowire classes with unique properties can be produced with the VLS method by precisely controlling size, composition and geometry of the nanowires²⁰. Specifically, (1) nanowires with different diameter and length are produced by varying the size of the metal nanoclusters and the growth time, respectively²⁷, (2) semiconductor nanowires with distinct doping profiles are realized by introducing molecular precursors of the dopant desired during the growth²⁹, (3) axial or coaxial modulated nanowires are synthesized by switching the composition and/or doping either during the elongation of the nanowire³⁰ or a sequential shell growth step following it³¹, (4) branched or tree-like nanowires are created with unique composition and/or doping combinations by sequential nanocluster-catalyzed growth³², and (5) kinked nanowires with rationally designed geometry are produced by introducing changes of crystalline growth direction during nanowire elongation³³. With these precise synthetic controls, nanoscale active device elements such as field-effect transistors (FET), p-n diodes and light-emitting diodes (LED) can be imbedded in the semiconductor nanowires through rational designs³². These families of functional

semiconductor nanowires have demonstrated the power of bottom-up synthetic approach and have opened up new opportunities in nanoscience and nanotechnology.

1.2 Nanowire assembly: hierarchical control with precision

High-density integration of high performance electronic devices has been the driving force of technology revolution for decades³⁴. Two distinct strategies are well known in the pursuit of this goal: top-down and bottom-up. The top-down strategy focuses on the development of technologies such as lithography, etching and thin-film deposition to pattern smaller features in bulk materials, while the bottom-up paradigm offers a more natural approach of building up nanomaterial with increasing complexity and quality. A crucial bridge between these two methodologies is controlled hierarchical assembly, which connects bottom-up synthesis of nanostructures with top-down fabrication.

A variety of approaches have been developed to assemble nanowires using Langmuir-Blodgett technique³⁵⁻³⁷, electric field³⁸, blown-bubble technique³⁹ or mechanical forces^{18,19,40-43}. Among these strategies, friction shear force based contact printing method has shown unique potential due to high efficiency and high alignment ratio¹⁸. This method utilizes the directional sliding friction shear force between a nanowire growth substrate and a receiver substrate to detach nanowires from the donor substrate and align them (**Fig. 1-2a**). The receiver substrate is pre-treated to increase adhesive interaction with nanowires chemically or physically. Recently, a nanocombing assembly technique has been reported as a step beyond contact printing¹⁹. In this new approach, anchoring and aligning regions are spatially separated and chemically distinct on the receiver substrate (**Fig. 1-2b**). This separation improved the assembly yield from ca. 90-95% with a misalignment angle of $\pm 5^\circ$ for contact printing to greater than 98.5% with a misalignment angle within $\pm 1^\circ$. Moreover,

this nanocombing method allows laterally deterministic assembly and end-to-end registration of single nanowire devices through lithography of distinct alignment window patterns. The advances in nanowire assembly techniques have pushed the limits of the fabrication of more compact circuits with superior performance. However, work remains to be done to expand assembly capability to nanowires with geometry beyond a straight line segment.

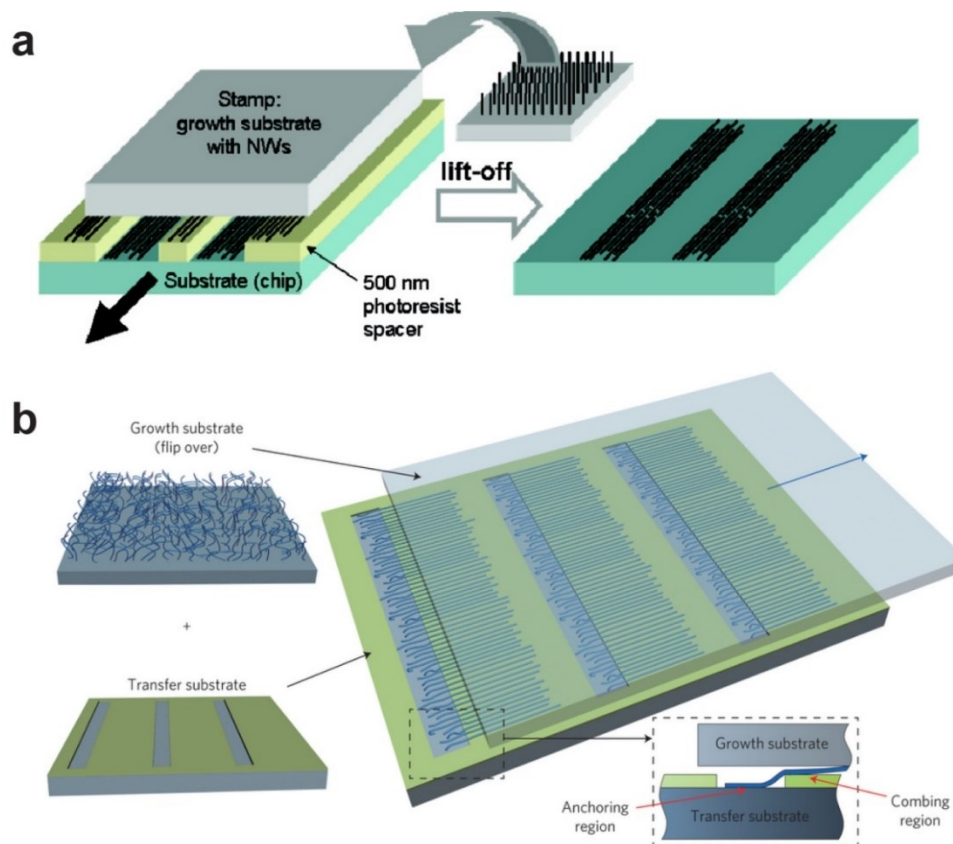


Figure 1-2. Schematics of contact printing and nanocombing assembly methods. a, Schematics of nanowire assembly by contact printing. Adapted from Ref. 18. **b,** Schematics of nanowire assembly by deterministic nanocombing. Adapted from Ref. 19.

1.3 Nanoelectronics and biology: interfacing at the natural scale

Recording cellular bioelectrical signals is central to understanding the fundamental behavior of cells and cell networks and has significant medical applications⁴⁴⁻⁵⁸. Recently there has been a surge of progress on developing nanotechnologies for biological applications⁵⁹⁻⁶³ including micro-to-nanoscale metal pillars⁶⁴⁻⁶⁶, semiconductor kinked nanowires⁶⁷ and nanotube devices⁶⁸⁻⁶⁹. These developments are reaching a level of sophistication that may impact standard electrophysiological recording methods. Patch-clamp allows for intracellular recording and has been key to providing insights into single-cell behavior, with the capability to deconvolve neural microcircuitry⁷⁰⁻⁷², yet patch pipettes as a general cellular interface have changed little over the past several decades and are not without experimental limitations.

Currently, there are several challenges that limit the experimental design of cellular probes. This is in part inherent to the cellular intricacy of tissues such as the brain, the complexity of cellular interactions, and the nonlinearities of the intracellular and network dynamics and is coupled to the need for minimally-invasive and long-lasting recordings. More specific aims and their limitations follow using the example of neurons: (1) Recording subthreshold activity: In many parts of the brain, post-synaptic potentials (PSPs) are summed across multiple neurons before any suprathreshold action potentials are generated. Recording this subthreshold activity is necessary for elucidating synaptic connectivity and microcircuitry⁷¹. Additionally, neural correlations and functional relationships are widely studied *in vivo* with extracellular recordings, but this type of analysis must be performed using incomplete suprathreshold point processes. This creates an “iceberg effect” where only the tip of the iceberg, spiking, is used for analysis while the underlying bulk of activity is ignored⁷²⁻⁷⁴. Continuous subthreshold fluctuations give a

much more sophisticated and complete picture of how neurons receive and engage with a computation. (2) Single-cell stimulation: Control of stimulation to evoke action potentials with single-cell precision greatly enhances the type of experimental questions one might ask. For example, reverse correlation of PSPs to direct stimulation of presynaptic cells can elucidate microcircuitry⁷¹. Further, stimulation even on a single-cell scale can evoke a behavioral response⁷⁵. As new technologies scale to allow for a multitude of precise stimulations, the ability to control network-level activity may be addressed. (3) Minimal invasiveness: New methods are needed to sample without interfering with natural processing in the brain and/or causing excessive damage. Such advances will be of particular importance when translating methods to human subjects and developing brain-machine interfaces. (4) Multiple cell-device interfaces: The number of cells that may be recorded simultaneously has steadily increased with improvements in new tools. Introducing new types of devices, which have higher spatial resolution, may also help with important questions requiring multiple simultaneous recordings within a single neuron's neurites or microdomains. (5) Stable cell-device interfaces: For recordings to be useful over longer periods of time, cellular interfaces must be stable. In particular, for behavioral experiments, having consistent recording sites for neurons across multiple trials is necessary for many sophisticated analyses.

The developments of semiconductor nanowire electronics and soft polymer probes for intracellular interfaces allow interaction at the natural cellular scale and are on the path to solving these challenges. In general, the conductivity in a semiconductor device is controlled by added dopant atoms that have either one extra or one less valence electron than the host material. When dopants with one extra valence electron/atom are added, a

semiconductor is termed “n-type” and conduction is by negative charge carriers; conversely, addition of dopants with one less valence electron/atom yields a “p-type” semiconductor with positive charge carriers. Spatial variations in the concentration of dopant atoms in a semiconductor allows for the implementation of different types of localized devices, including FETs and p-n junction diodes.

A working FET device is configured by connecting source and drain electrodes, and when a voltage is applied between these electrodes the measured conductance (which depends on device size and dopant concentration) varies as the local external potential changes due to events such as an action potential. This potential (voltage) dependent change in conductance – the device transconductance – represents the device sensitivity. Advantages of measuring local electrical potential in this way compared to standard neurophysiological electrodes include: (1) they can be miniaturized to the 10-nm scale without loss of bandwidth, and (2) they do not exchange material with cells and do not depend on interface impedance⁶⁰.

In particular, smaller recording structures are an important goal because they offer the potential for increased stability and reduced invasiveness, as well as increasing the number of recording sites, as is important for probing functional relationships between neurons across multiple cell types. Single-ended electrodes such as microwires for tetrodes, metal pads for silicon probes, and similar devices suffer from impedance limits and related issues as the sizes of these probes shrink⁶³.

The unique scaling of FETs to ultra-small sizes relevant to new electrophysiology capabilities, has been realized through the size-, dopant- and morphology-controlled synthesis of semiconductor nanowires⁶⁰. For example, single-crystal silicon nanowires

have been grown with diameters as small as 5 nm and with dopant variations, which define the FET recording device, on the order of 10 nm. Using nanofabrication methods, including high-resolution lithography and deposition techniques, to configure these synthesized nanowire structures into nanowire FETs has led to 100-nm-scale, 3D devices small enough for isolated intracellular recordings⁶⁷.

One clear advantage of nanoscale devices such as nanowire FETs is their potential to be developed as novel intracellular recording tools, where several distinct approaches have been reported to date. Nanofabrication has been used to define passive metal nanopillar devices that can yield intracellular-like signals from cultured cells⁶³, while a combination of nanowire synthesis and nanofabrication have yielded several distinct types of 3D nanoFET devices that record true intracellular signals⁶⁰.

One of the most promising designs comes from kinked nanowires⁶⁷, where the ‘kinked structure’ and nanoFET recording element (**Fig. 1-3a**) are encoded directly during synthesis. In this way, source and drain electrical connections can be made remote from the cell membrane, which contrasts with nanofabricated linear FETs and allows the highly localized FET isolated at the ‘kink’ tip to be inserted into a cell without damage. Moreover, efforts have been made to bend the polymer probe up from the substrate into a 3D configuration to facilitate nanowire-cell interaction (**Fig. 1-3b**). Interestingly, it has been found that kinked nanowire devices coated with phospholipids can directly penetrate the membrane of cultured cells without application of mechanical forces and record intracellular action potentials⁶⁷. Due to the small and highly localized nature of the FET on the kinked nanowire probe, the intracellular potential can be well isolated.

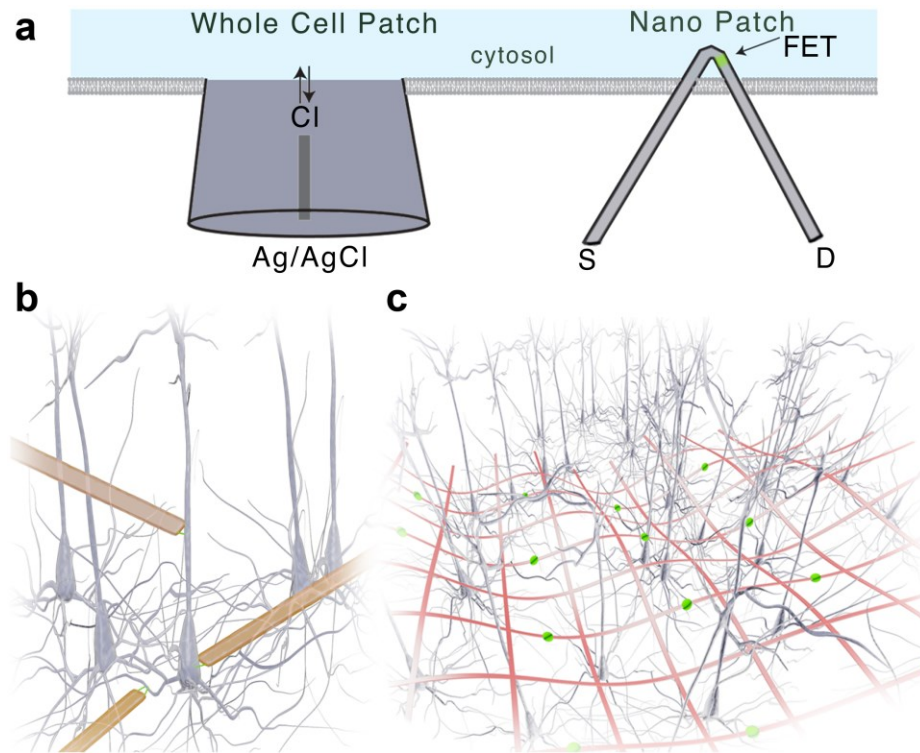


Figure 1-3. Nanowires as a new approach to electrophysiology. **a**, New recording methods such as nanowires for localized intracellular recordings will have advantages compared to patch pipettes. Nanowire FETs require source (S) and drain (D) electrode connections for making high-sensitivity recordings. **b**, 3D polymer probes can facilitate nanowire-cell interaction. **c**, Nanowires may be integrated with 3D flexible electronics for experiments in cultures or, potentially, *in vivo*.

Potential advantages of kinked nanowire FET probes compared to patch pipettes include the absence of solution exchange during measurements and the highly localized size (tens to hundreds of nanometers) of the nanowire FETs. Standard whole-cell patch-clamp involves solution exchange between the intracellular space and the pipette reservoir, which can affect the functioning of the cell. While the internal solution ideally mimics the intracellular environment, the solution components may alter recordings. For example, electrophysiological properties such as after-hyperpolarization potential and input resistance may change over time using potassium-ion source compounds potassium

gluconate or potassium methylsulfate⁷⁶. Perforated patch methods can ameliorate such problems, but can introduce other issues such as inherent access resistance.

However, one limitation of these nanoscale bioprobes is that they have been fabricated primarily on bulk planar substrates. Substrate-based nanodevices can facilitate *in vitro* cell culture, but are difficult to target independently to specific cells or processes and thus cannot exploit much of the ‘nano’ advantage. The development of a free-standing nanowire probe can overcome this limitation and expand the scope of applications.

In addition to the focus on *in vitro* measurements, there has been increasing interest in *in vivo* intracellular recordings, since these can provide greater insight into behavioral microcircuit dynamics than is possible with extracellular measurements. Early *in vivo* patch studies focused on anesthetized and then quiet resting or sleep states in order to maintain stable recordings⁷³. By modifying how patch pipettes are secured to the skull, stable patch recordings have been performed during active movement, although only for short time periods⁷⁷. Such awake-state patch experiments have allowed a deeper understanding of the relationship between subthreshold dynamics, behavior and brain states⁷⁷. Nevertheless, there are intrinsic limits to recording stability due to stiffness mismatch between glass pipettes and brain tissue, which yields maximal shear strains in the tissue at the patch site.

Nanowire FET probes, which are fabricated with soft polymer supports, can overcome this mechanical limitation of patch pipettes. In addition, the small sizes possible for nanowire FET polymer probes are less likely to be rejected by the brain and to cause glial scarring and chronic damage. Hence, it is expected that soft nanowire FET probe structures may allow cellular recordings to be maintained over the course of days though multiple brain states and behavioral paradigms. By improving the stability of cellular

recordings, these methodologies could advance our understanding of neuronal processing in extended behavioral contexts between many brain states.

The potential of flexible polymer electronic interfaces can be extended from individual nanoprobe to 3D macroporous flexible meshes, where addressable nanowire FETs and other nanodevices are integrated within the mesh scaffolds. The width/thickness dimensions of the mesh with embedded electrical interconnects can be on the order of a micron or less, and thus similar to neural processes. The large mesh area allows for a multitude of simultaneous electrical lines and recording sites on a single, free standing, flexible support through which neurons/processes can interpenetrate (**Fig. 1-3c**) and could confer a great advantage for scaled-up recordings. Recent work from our group has already demonstrated the use of these meshes as 3D scaffolds for integrating FET electronics in combination with 3D cell culture^{60,78-80}. Current studies are focusing on integrating 3D macroporous electronic meshes with the capability of intracellular recording within the living brain which could push the medical boundaries of brain machine interfaces and general neural prostheses.

1.4 Overview of thesis

In this thesis, I will focus on three key topics of nanoscience and nanotechnology: (1) development of novel nanowire materials and their unique physical properties, (2) advanced nanowire assembly methods, and (3) interfacing novel nanoprobe with biological systems. The central aim of this thesis is to explore the fundamental limits of nanoelectronic devices and the scope of their applications based on the bottom-up paradigm.

In Chapter 2, I will first introduce the development of kinked p-n junction nanowire probes as a new family of localized biological/chemical sensors. P-n diode as an active device is more naturally localized during a typical CVD synthesis process than FETs in semiconductor nanowires. I will show that the conductance of a nanoscale p-n diode can be controlled by the surrounding gating voltage. The localization of the sensing is characterized with detailed scanning probe measurement and demonstrated by charged nanoparticle detection. I will also show results of intracellular electrical recording from spontaneously beating cardiomyocytes using kinked p-n junction nanowire 3D probes.

Then I will discuss the design and synthesis of a new class of diverse functional kinked nanowire structures in Chapter 3. I will show a multi-step strategy to grow multi-kinked nanowires with controllable geometry and multiple active device elements. Three specific examples discussed in details are ultra-sharp U-shaped nanowires, V-shaped nanowires with series of FET devices and W-shaped nanowires with parallel FET devices. I will also show proof-of-concept demonstration of multiplexed 3D nanoprobe with W-shaped nanowires.

In Chapter 4, I will demonstrate a shape-controlled deterministic assembly method of nanowires. This new approach takes a step beyond nanocombing to create arrays of nanowires with not only deterministic position but also well-controllable geometry. Trenches with variety of shapes are fabricated using photolithography (PL) and electron-beam lithography (EBL) as anchoring sites. I will present assembly of U-shaped nanowire arrays on a 3-inch-wafer scale. Other shapes such as rectangular and triangular are also demonstrated. A multi-step strategy to assemble bending nanowire structures with designed geometry is explored. In addition, I will discuss the mechanism of the assembly

and the experimental parameters determining the shape of nanowires in detail. Moreover, I will show various unique applications of this technique ranging from the fabrication of 3D probe arrays to designed elements of nanophotonic circuits.

In Chapter 5, I will focus on the design and development of the first free-standing kinked nanowire probe for targeted intracellular recording. This novel probe configuration frees nanoscale building blocks from bulk substrate and enables precise 3D positioning control. I will discuss a general fabrication strategy to build micro-to-nanoscale electrical connections with a free-standing nanostructure. I will present results of intracellular recording from the same cell simultaneously using a free-standing nanowire probe and a patch-clamp. Ion channel blockers are used to demonstrate the potential application of these probes in drug screening. To achieve multiplexed intracellular recording, I will show two unique methods using either two probes or one probe with two device elements.

Finally in Chapter 6, I will present new directions of localized cell stimulation using kinked p-n junction nanowires. I will discuss the two distinct functional modes of a p-n diode nanowire in forward and reverse bias due to current rectification, which correspond to electrical recording and stimulation, respectively. I will show with simulation that significant electric field can be generated around the depletion region of the device working in reverse bias, which can be used to activate voltage sensitive ion channels on cell membranes. Thanks to the nanosize of the p-n diode, the stimulation effect can be highly localized. I will present results of stimulation of action potentials on Chinese hamster ovary (CHO) cells and neurons. The capability of stimulation completes the two-way communication between semiconductor nanowire devices and biological systems and opens up new opportunities in the studies of neuronal circuits and brain mapping.

1.5 Bibliography

1. Lieber, C. M. *MRS Bull.* **28**, 486 (2003).
2. Samuelson, L. *Mater. Today* **6**, 22 (2003).
3. Wang, Z. L., *Mater. Today* **7**, 26 (2004).
4. Alivisatos, A. P. *Science* **271**, 933 (1996).
5. Dresselhaus, M. S., Dresselhaus, G., Avouris, P. *Carbon Nanotubes: synthesis, structure, properties and applications*. (Springer-Verlag Berlin Heidelberg, 2001).
6. A. de Heer, W. *MRS Bull.* **29**, 281 (2004).
7. Geim, A. K., Novoselov, K. S. *Nat. Mater.* **6**, 183 (2007).
8. Lieber, C. M., Wang, Z. L., *MRS Bull.* **32**, 99 (2007).
9. Murray, C. B., Kagan, C. R. & Bawendi, M. G. *Ann. Rev. Mater. Sci.* **30**, 545 (2000).
10. Pentes, V. F., Krishnan, K. M. & Alivisatos, A. P. *Science* **291**, 2115 (2001).
11. Iijima, S. *Nature* **354**, 56 (1991).
12. Morales, A. M. & Lieber, C. M. *Science* **279**, 208 (1998).
13. Shulaker, M. M., *et al.* *Nature* **501**, 526 (2013).
14. Yao, J. *et al.* *Proc. Natl. Acad. Sci. USA* **111**, 2431 (2014).
15. Heiss, M. *et al.* *Nat. Mater.* **12**, 439 (2013).
16. Hu, J. T., Odom, T. W. & Lieber, C. M. *Acc. Chem. Res.* **32**, 435 (1999).
17. Gudixsen, M. S., Lauhon, L. J., Wang, J., Smith, D. C. & Lieber, C. M. *Nature* **415**, 617 (2002).
18. Javey, A., Nam, S., Friedman, R. S., Yan, H. & Lieber, C. M. *Nano Lett.* **7**, 773 (2007).
19. Yao, J., Yan, H., Lieber, C. M. *Nat. Nanotech.* **8**, 329 (2013).
20. Lieber, C. M. *MRS Bull.* **36**, 1052 (2011).
21. Wagner, R. S. & Ellis, W. C. *Appl. Phys. Lett.* **4**, 89 (1964).
22. Duan, X. F. & Lieber, C. M. *J. Am. Chem. Soc.* **122**, 188 (2000).

23. Liu, J. L., Cai, S. J., Jin, G. L., Thomas, S. G. & Wang, K. L. *J. Cryst. Growth* **200**, 106 (1999).
24. Wu, Y. Y. & Yang, P. D. *J. Am. Chem. Soc.* **123**, 3165 (2001).
25. Wu, Y. *et al. Nano Lett.* **4**, 433 (2004).
26. Hansen, M. & Anderko, K. *Constitution of binary alloys*. (McGraw-Hill, 1958).
27. Duan, X. & Lieber, C. M. *Adv. Mater.* **12**, 298 (2000).
28. Haraguchi, K., Katsuyama, T., Hiruma, K. & Ogawa, K. *Appl. Phys. Lett.* **60**, 745 (1992).
29. Cui, Y., Duan, X., Hu, J. & Lieber, C. M. *J. Phys. Chem. B* **104**, 5213 (2000).
30. Kempa, T. J. *et al. Nano Lett.* **8**, 3456 (2008).
31. Tian, B. *et al. Nature* **449**, 885 (2007).
32. Jiang, X. *et al. Proc. Natl. Acad. Sci. USA* **108**, 12212 (2011).
33. Tian, B. Z., Xie, P., Kempa, T. J., Bell, D. C. & Lieber, C. M. *Nat. Nanotech.* **4**, 824 (2009).
34. Moore, G. *Electronics* **38**, 114 (1965).
35. Whang, D., Jin, S., Wu, Y. & Lieber, C. M. *Nano Lett.* **3**, 1255 (2003).
36. Tao, A. R., Huang, J. & Yang, P. *Acc. Chem. Res.* **41**, 1662 (2008).
37. Wang, D. W., Chang, Y. L., Liu, Z. & Dai, H. *J. Am. Chem. Soc.* **127**, 11871 (2005).
38. Smith, P. A. *et al. Appl. Phys. Lett.* **77**, 1399 (2000).
39. Yu, G., Cao, A. & Lieber, C. M. *Nat. Nanotech.* **2**, 372 (2007).
40. Duan, X. F., Niu, C. M., Sahi, V., Chen, J., Parce, J. W., Empedocles, S. & Goldman, J. L. *Nature* **425**, 274 (2003).
41. Huang, Y., Duan, X. F., Wei, Q. Q. & Lieber, C. M. *Science* **291**, 630 (2001).
42. Fan, Z. *et al. Nano Lett.* **8**, 20 (2008).
43. Nam, S., Jiang, X., Xiong, Q., Ham, D. & Lieber, C. M. *Proc. Natl. Acad. Sci. USA* **106**, 21035 (2009).
44. Hille, B. *Ion channels of excitable membranes*. (Sinauer Associates, Inc. 2001).

45. Zipes D. P. & Jalife, J. *Cardiac electrophysiology: From cell to bedside*. (Saunders, 2004).
46. Dhein, S., Mohr, F. W. & Delmar, M. *Practical methods in cardiovascular research*. (Springer, 2005).
47. Davie, J. T., Kole, M. H. P., Letzkus, J. J., Rancz, E. A., Spruston, N., Stuart, G. J. & Häusser, M. *Nat. Protocols* **1**, 1235 (2006).
48. Halbach, M. D., Egert, U., Hescheler, J. & Banach, K. *Cell. Physiol. Biochem.* **13**, 271 (2003).
49. Meyer, T., Boven, K. H., Gunther, E. & Fejtl, M. *Drug Safety* **27**, 763 (2004).
50. Erickson, J., Tooker, A., Tai, Y. C. & Pine, J. *J. Neurosci. Method.* **175**, 1 (2008).
51. Law, J. K. Y., Yeung, C. K., Hofman, B., Ingebrandt, S., Rudd, J. A., Offenhäusser, A. & Chan, M. *Physiol. Meas.* **30**, 155 (2009).
52. Ingebrandt, S., Yeung, C.-K., Krause, M. & Offenhäusser, A. *Biosens. Bioelectron.* **16**, 565 (2001).
53. Yeung, C.-K., Ingebrandt, S., Krause, M., Offenhäusser, A. & Knoll, W. *J. Pharmacol. Toxicol. Meth.* **45**, 207 (2001).
54. Cohen, A., Shappir, J., Yitzchiak, S. & Spira, M. E. *Biosens. Bioelectron.* **22**, 656 (2006).
55. Cohen, A., Shappir, J., Yitzchaik, S. & Spira, M. E. *Biosens. Bioelectron.* **23**, 811 (2008).
56. Lu, Z.-L., Pereveraev, A., Liu, H.-L., Weihergräber, M., Henry, M., Krieger, A., Smyth, N., Hescheler, J. & Schneider, T. *J. Electrocardiology* **14**, 11 (2004).
57. Reppel, M., Pillekamp, F., Lu, Z. J., Halbach, M., Brockmeier, K., Fleischmann, B. K. & Hescheler, J. *J. Electrocardiology* **37**, 104 (2004).
58. Fromherz, P. *ChemPhysChem* **2**, 276 (2002).
59. Parpura, V. *Nature Nanotech.* **7**, 143 (2012).
60. Duan, X., Fu, T. M., Liu, J., & Lieber, C. M. *Nano Today* **8**, 351 (2013).
61. Dunlop, J., Bowlby, M., Peri, R., Vasilyev, D. & Arias, R. *Nature Rev. Drug Discov.* **7**, 358 (2008).
62. Rogers, J. A. *MRS Bull.* **39**, 549 (2014).
63. Spira, M. E. & Hai, A. *Nat. Nanotech.* **8**, 83 (2013).

64. Xie, C., Lin, Z., Hanson, L., Cui, Y. & Cui, B. *Nat. Nanotech.* **7**, 185 (2012).
65. Robinson, J. T. *et al.* *Nat. Nanotech.* **7**, 180 (2012).
66. Hai, A., Shappir, J. & Spira, M. E. *J. Neurophysiol.* **104**, 559 (2010).
67. Tian, B. *et al.* *Science* **329**, 831 (2010).
68. Duan, X. *et al.* *Nat. Nanotech.* **7**, 174 (2012).
69. Gao, R. *et al.* *Nano Lett.* **12**, 3329 (2012).
70. London M. & Häusser M. *Annu. Rev. of Neurosci.* **28**, 503 (2005).
71. Silberberg, G., Grillner, S., LeBeau, F. E., Maex, R. & Markram, H. *Trends Neurosci.* **28**, 541 (2005).
72. Lampl, I., Reichova, I. & Ferster, D. *Neuron* **22**, 361 (1999).
73. Steriade, M., Timofeev, I. & Grenier, F. *J. of Neurophysiol.* **85**, 1969 (2001).
74. Kruskal, P. B., Li L. & MacLean J. N. *Nat. Commun.* **4** 2574 (2013).
75. Houweling, A. R. & Brecht M. *Nature* **451**, 65 (2007).
76. Kaczorowski, C. C., Disterhoft, J. & Spruston, N. *J. Physiol.* **578**, 799 (2007).
77. Epsztein, J., Brecht, M. & Lee, A. K. *Neuron* **70**,109 (2011).
78. Tian, B. *et al.* *Nat. Mater.* **11**, 986 (2012).
79. Liu, J. *et al.* *Proc. Natl. Acad. Sci. USA* **110**, 6694 (2013).
80. Tian, B. & Lieber, C. M. *Annu. Rev. Anal. Chem.* **6**, 31 (2013).

Chapter 2. Kinked p-n junction nanowire probes for high spatial resolution sensing and intracellular recording

2.1 Introduction

The rational design and synthesis of nanomaterials have enabled many advances in functional nanoelectronics¹⁻⁹, and moreover, have opened-up unique opportunities at the interface between nanoelectronics and biological systems^{2,10-21}. For example, recent studies have shown that nanoFETs can be synthetically encoded at the tips of kinked silicon nanowires^{2,5}. These kinked nanostructures can be readily configured as 3D bioprobes, which enabled recording intracellular action potentials from beating cardiomyocytes in a minimally-invasive manner². This work represented the first demonstration of internalizing an active electronic probe, a transistor, which was comparable in size to viruses and many biological macromolecules inside a cell. While these studies open up a new paradigm for integrating electronics with cells and tissue, they are also potentially limited in that synthetic preparation of an ideal point-like nanoFET detector is challenging.

In this regard, nanoscale p-n diodes are attractive since the device element is naturally localized at the depletion region of the junction²². A number of previous studies have shown that p-n junctions can be synthetically encoded in axial and core/shell nanowires^{3-4,23-24}, although only the photovoltaic properties of such nanojunctions have been thoroughly studied^{3,4}. Such p-n diodes have not yet been investigated as biological/chemical sensors. In this chapter, I will demonstrate a successful synthetic integration of p-n junction in the kinked silicon nanowire structure, and study for the first

time both experimentally and theoretically these devices as highly localized electronic biosensors. In particular, I will focus on the use of p-n junction kinked nanowire devices for charge sensing down to the single nanoparticle level, and for intracellular potential recording within live cells.

2.2 Experimental

2.2.1 Nanowire synthesis

Kinked p-n silicon nanowires were synthesized by CVD through a nanoparticle-catalyzed VLS process as described previously⁵. Specifically, 100 nm diameter gold nanoparticles (Ted Pella) were dispersed on Si growth substrates with 600 nm SiO₂ layer (Nova Electronic Materials). Growth of heavily boron-doped p-type arm was first carried out by feeding SiH₄ (1 sccm), B₂H₆ (10 sccm, 100 ppm in H₂) and H₂ (60 sccm) into the system for 15 min at a total pressure of 40 torr and temperature of 450 °C. The growth was then paused for 15 s by rapidly evacuating the chamber to lowest pressure and shutting off the gas lines. SiH₄ (1 sccm), PH₃ (4 sccm, 1000 ppm in H₂), and H₂ (60 sccm) were then flown into the system at the same total pressure and temperature to grow a heavily doped n-type section for 30 s, forming the p-n junction. A second evacuation of 15 s followed, and finally the heavily doped n-type arm was allowed to finish in additional 15 min.

2.2.2 Device fabrication

For planar devices, two pairs of metal electrodes (1.5 nm Cr/120 nm Pd/60 nm Cr, spacing between electrodes 1.5 μm) were fabricated on each of the p- and n-type arms of a kinked nanowire device. 3D bend-up devices were fabricated using procedures similar to previous studies². The diameter of the nanowire was 100 nm.

2.2.3 Tip-modulated scanning gate microscopy characterization

The device chip was mounted on a BioScope MultiMode SPM stage (Digital Instrument). A constant current of 250-700 nA was injected into the kinked p-n device, resulting in a forward bias of ~ 1 V. The voltage drop across the device was measured using a low-noise differential preamplifier (SR560, Stanford Research Systems). A conductive atomic force microscopy (AFM) tip (ARROW-CONTPT-10, NanoWorld) vibrating at a resonance frequency of 90 kHz was used as a local gate and scanned over the device to map the conductance image in “Lift Mode”. Specifically, first for each scan line zero potential was applied to the tip, and a topographic image was acquired in Tapping Mode with feedback enabled. The tip was then lifted up 30 nm, and a tip potential of ± 5 V was applied. The tip was scanned across the same line again following the captured topological profile with feedback turned off, when the change of voltage across the device was recorded with a lock-in amplifier (SR830, Stanford Research Systems) using the tip oscillation as the reference frequency²⁵. In order to remove the drift error during the imaging, we scanned in opposite directions for $V_{\text{tip}} = +5$ V (FWHM = 120 nm) and $V_{\text{tip}} = -5$ V (FWHM = 300 nm) images, and obtain the average of 210 nm as the corrected length of the sensitive region for our device.

2.2.4 Charged nanoparticle sensing

To control the solution flowing over the devices, a 1.7 mm thick polydimethylsiloxane (PDMS) sheet with a micro-fluidic channel 50 μm in height and 1 mm in width was put on the device chip. Fluorescent polystyrene nanobeads of 100 nm in diameter (initial concentration 24 nM in deionized water, excitation wavelength 540 nm, emission wavelength 560 nm, from Phosphorex) were diluted in deionized water (1:20),

and introduced into the microfluidic channel at a flow rate of 0.02 ml/hour set by a syringe pump (PHD 2000, Harvard Apparatus). A confocal fluorescent microscope (FV1000, Olympus) was used to image the motion of the fluorescent nanobeads and the kinked probes in real time while the conductance was recorded. Real-time fluorescent images of the p-n junction area were captured at a rate of 2 Hz using a 559 nm laser to excite the nanobeads. Two channels with filters of 490-540 nm and 575-675 nm were recorded together to rule out noise signals and unambiguously identify the nanobeads. Images were then superimposed over the device image recorded with a 535-565 nm filter to mark the relative position of the nanobeads and the p-n junction. The Zeta potential of the nanobeads was measured using PALS Zeta Potential Analyzer (Brookhaven Instruments). An averaged zeta potential of -59 ± 11 mV from 6 runs was obtained.

2.2.5 Cellular recordings

Embryonic chicken cardiomyocytes were cultured using published protocols on thin PDMS films^{2,11}. Device chips were incubated with lipid vesicles of 1,2-dimyristoyl-sn-glycero-3-phosphocholine (DMPC, Avanti Polar Lipids Inc.) containing 1% 1-myristoyl-2-{12-[(7-nitro-2-1,3-benzoxadiazol-4-yl) amino] dodecanoyl}-sn-glycero-3-phosphocholine (NBD-lipid, Avanti Polar Lipids Inc.) as fluorescent reporter to form lipid bilayers over the nanowire surface, using a procedure described earlier². The cell recording measurements were carried out in Tyrode solution (Sigma Aldrich) at 35 °C. The devices were forward biased at 1.0 V, and the current was converted to voltage with a current preamplifier (Model 1211, DL Instruments) at sensitivity of 10^{-6} A/V, before low-pass filtered (0-6 kHz, CyberAmp 380, Molecular Devices), and digitized at 20 kHz sampling rate (Axon Digi1440A, Molecular Devices). A Ag/AgCl reference electrode was used to

fix the extracellular solution potential at a constant value of +0.3 V in all recording experiments^{2,11}. The PDMS/cell sheets were manipulated using a glass micropipette mounted on a micromanipulator, to control the relative position between the cells and the nanowires as previously reported^{2,11}.

2.3 Results and discussion

2.3.1 Nanowire synthesis and characterization

Kinked p-n junction silicon nanowires were synthesized by gold nanoparticle-catalyzed CVD process with doping and geometric control adapted from our previous report⁵. Initially, boron-doped p-type Si nanowires were grown for 15 min at a calibrated growth rate of 0.7 $\mu\text{m}/\text{min}$. The reactor was evacuated for ca. 15 s, and then growth was continued using phosphine dopant to create an n-type nanowire segment (forming the p-n junction) for 30 s, followed by a second cycle of reactor evacuation and continued growth using phosphine for ca. 15 min. Scanning electron microscopy (SEM) images of the Si nanowires prepared in this way (**Fig. 2-1a**) showed that the majority (> 90%) of the kinked nanowires have a 120° angle between the two arms, which is consistent with our previous results that the abrupt evacuation/resumption of feeding gases during the growth of n-type Si nanowires introduces a 120° kink in high-yield⁵. In addition, analysis of images showed that a small fraction (< 10%) of the kinked nanowires exhibited a 60° angle (**Fig. 2-1b**), indicating that the switching between p- and n-dopant could also introduce a similar kink (with both in *cis* orientation²) albeit at a much lower yield.

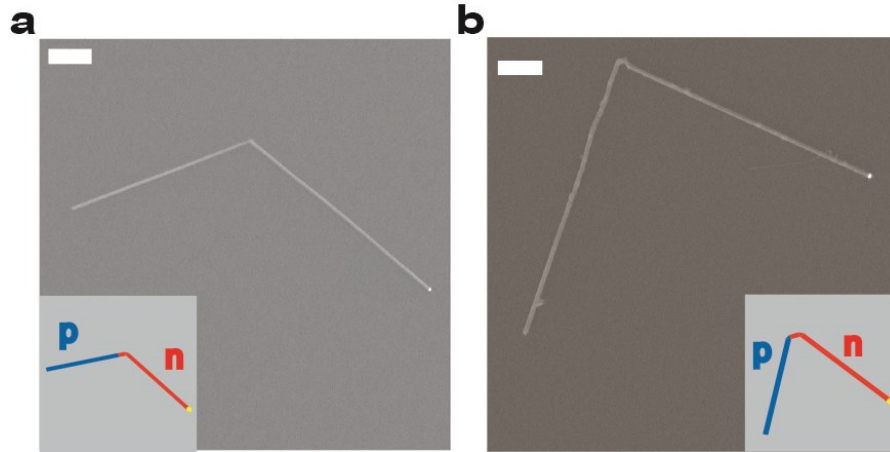


Figure 2-1. Design and controlled synthesis of kinked p-n nanowires. a, Representative SEM image of a kinked p-n Si nanowire with 120° tip angle. Scale bar, $1\ \mu\text{m}$. Inset: Schematic of a kinked p-n nanowire with 120° tip angle. The blue and red lines designate the p-doped and n-doped arms, respectively. **b,** Representative SEM image of a kinked p-n Si nanowire with 60° tip angle. Scale bar, $1\ \mu\text{m}$. Inset: Schematic of a kinked p-n nanowire with 60° tip angle. The blue and red lines designate the p-doped and n-doped arms, respectively.

2.3.2 Device fabrication and electrical characterization

To assess the overall electrical characteristics of the kinked p-n nanowires, contacts (Cr/Pd/Cr 1.5/120/60 nm) were defined on both arms by EBL and metallization² (**Fig. 2-2a**, inset). Typical current versus voltage (I-V) data (**Fig. 2-2a**) show clear rectification with no measurable current in reverse bias and an onset for current flow of 0.6 V in forward bias. These results are consistent with previously studies of straight Si nanowires with axial p-n junctions⁴.

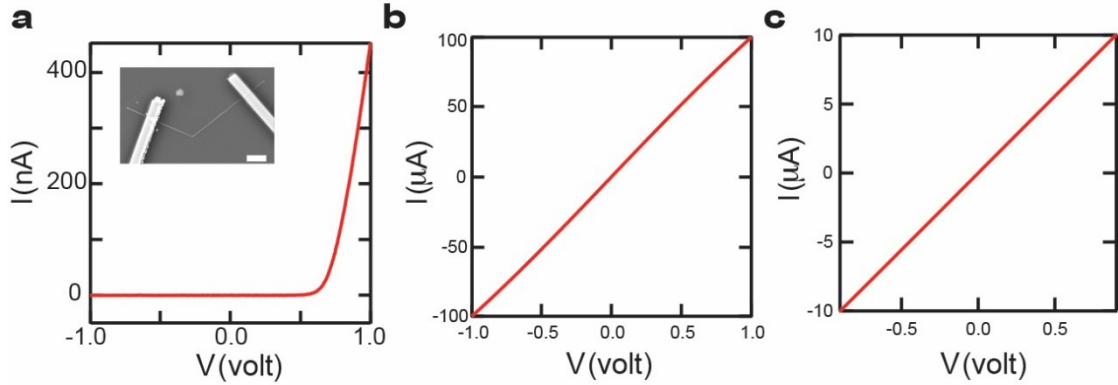


Figure 2-2. Kinked p-n nanowire device characterization. **a**, I-V data recorded from a representative kinked p-n nanowire device. Inset: SEM image of the device structure. Scale bar, 2 μ m. **b**, I-V data recorded from the n-type arm of a representative kinked p-n nanowire device. The spacing between electrodes was 1.5 μ m. No barrier was present at metal contact. **c**, I-V data recorded from the p-type arm of the same device in **b**. The spacing between electrodes was 1.5 μ m. No barrier was present at metal contact.

In addition, measurements made on devices with two contacts per arm (**Fig. 2-2b,c**) showed that no metal/nanowire Schottky barriers were present and allowed the estimation of the dopant concentrations. The doping levels of the arms were estimated using $N = \sigma / q\mu$, where N is the doping level, σ is the conductivity calculated from the slope of the I-V traces in **Fig. 2-2b** and **Fig. 2-2c**, q is the charge of an electron, and μ is the mobility. Here μ is taken as $14 \text{ cm}^2/\text{V}\cdot\text{s}$ ²⁶. Specifically, the dopant concentrations of the p-arm and n-arm were estimated to be ca. $9 \times 10^{18} \text{ cm}^{-3}$ and $9 \times 10^{19} \text{ cm}^{-3}$, respectively.

2.3.3 Diode sensing analysis

In a planar p-n diode device, the p-n junction is mostly buried beneath the surface and thus can only be partially gated with a top gate electrode²⁷. In contrast, the axial design of our kinked nanowires fully exposes the nanoscale p-n junction to external potential and enables a much more effective gate modulation of the transport behavior. **Fig. 2-3** illustrates a schematic band diagram change of the nanowire diode when a gate potential is

applied at the p-n junction. The heavily doped p- and n- arms are not affected by the gate and the Fermi energy is pinned along the nanowire. When a negative potential is applied, the electron energy levels in both the conduction band and the valence band are raised (Blue dashed lines in **Fig. 2-3**). As a result, the p-depletion region becomes more conductive, while the n-depletion region less conductive. In the case of applying a positive potential, the opposite occurs. In order to estimate the overall gate response of our device, we assume that (1) the carrier concentration distribution in the depletion region is linear, (2) the depletion region can be approximated as a number of small segments, each of which can be treated as an FET with uniform doping, (3) the gate coupling is ideal, and (4) the width of the depletion region is the same as the abrupt junction. In addition, the mobility along the nanowire is treated as uniform, to simplify the calculation without affecting the physics.

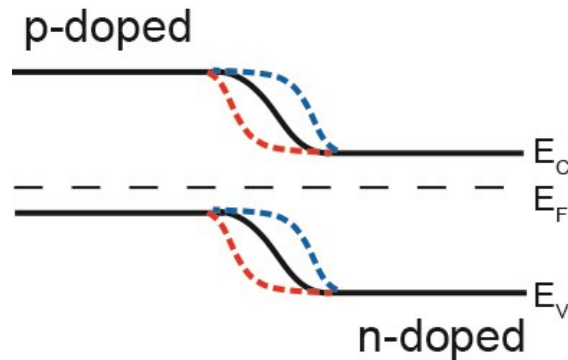


Figure 2-3. Schematic of diode band diagram under gate potentials. Schematic band diagram (black curves) and band diagram change of kinked p-n nanowires under gate potential. The blue and red dashed lines designate band diagram under negative and positive gate potentials respectively. E_C , E_V and E_F mark the position of the conduction band, valence band and Fermi energy, respectively.

We first use n-type depletion region as an example of calculating resistance change of p-n junction under gating potential. Basic semiconductor physics has: $\sigma_n = nq\mu$,

$n = N_C e^{-(E_c - E_f)/kT}$, where σ is the electrical conductivity, n is the carrier concentration of electrons, q is the charge of an electron, μ is the mobility of electrons, N_C is the density of states at the conduction band edge. Assuming that carrier concentration distribution within the depletion region along the nanowire is linear ($n = n_i + lk_D$), it follows that:

$$\Delta\sigma_n = \Delta n q \mu = n q \mu (\Delta V q / kT) = \Delta V q \sigma_n / kT \quad (1)$$

$$\Delta\rho_n = -\Delta\sigma_n / \sigma_n^2 = -\Delta V / (n \mu kT) = -\Delta V / [(n_i + lk_D) \mu kT] \quad (2)$$

$$\Delta R_n = \int_{-l_A}^0 \frac{\Delta\rho_n}{\pi r^2} dl = \int_0^{l_D} \frac{\Delta V}{\pi r^2 \mu kT [(n_i + lk_D)]} dl = -\frac{\Delta V}{\pi r^2 \mu kT k_D} \text{Ln}\left(\frac{N_D}{n_i}\right) \quad (3)$$

where ρ and R are the resistivity and resistance, respectively.

Using the same method, we can have resistance change of the p-type depletion region as:

$$\Delta R_p = \int_{-l_A}^0 \frac{\Delta\rho_p}{\pi r^2} dl = \int_{-l_A}^0 \frac{\Delta V}{\pi r^2 \mu kT [(n_i - lk_A)]} dl = \frac{\Delta V}{\pi r^2 \mu kT k_A} \text{Ln}\left(\frac{N_A}{n_i}\right) \quad (4)$$

So the total resistance change can be expressed as:

$$\Delta R = \Delta R_n + \Delta R_p = \frac{\Delta V}{\pi r^2 \mu kT} \left[\frac{1}{k_A} \text{Ln}\left(\frac{N_A}{n_i}\right) - \frac{1}{k_D} \text{Ln}\left(\frac{N_D}{n_i}\right) \right] \quad (5)$$

Because $l_D N_D = l_A N_A$, $l_D k_D \cong N_D$, $l_A k_A \cong N_A$

It yields: $\frac{k_D}{k_A} = \left(\frac{N_D}{N_A}\right)^2$, and

$$\Delta R \cong A \Delta V \left[\frac{1}{N_A^2} \text{Ln}(N_A) - \frac{1}{N_D^2} \text{Ln}(N_D) \right] \quad (5)$$

When $N_D > N_A$ and $\Delta V > 0$, $\Delta R > 0$, the device behaves as a p-type FET

When $N_D < N_A$ and $\Delta V > 0$, $\Delta R < 0$, the device behaves as an n-type FET

It shows that the resistance change (ΔR) of the p-n junction can be expressed as

$$\Delta R \propto A \Delta V \left[\frac{\text{Ln}(N_A)}{N_A^2} - \frac{\text{Ln}(N_D)}{N_D^2} \right],$$
 where ΔV is the change of the gate potential, and N_A and

N_D are the dopant concentration of the p- and n-arms, respectively. When N_A and N_D are equal or comparable, the p-n junction will behave as an ambipolar FET. However, when $N_A < N_D$, the p-n junction will function as a p-type FET, and similarly, when $N_A > N_D$, an n-type. In our design the doping level of the p-arm is ten times lower than the n-arm, thus the device is predicted to behave as a p-type FET.

2.3.4 Kinked p-n junction nanowire sensing characterizations

Tip-modulated scanning gate microscopy (tmSGM)²⁵ was used to identify directly the gate response and length-scale of the sensitive regions in kinked p-n nanowire devices. Briefly, a conductive AFM tip was used as a local gate to modulate the conductance of the kinked p-n nanowire junction. The conductance change was phase-locked to the vibration of the tip to enhance the spatial resolution²⁵, and the conductance map at different tip biases was superimposed over the topological image of the device. Representative data (**Fig. 2-4a**) show several key features. First, only the region close to the kink where the p-n junction was synthetically defined showed clear gate response. Second, the p-depletion region gave 3-5 fold larger conductance change than the n-depletion region (**Fig. 2-4a**, inset traces). This result is consistent with our theoretical estimate using the calculated dopant concentration of the arms, and implies that the device behavior is similar to a p-type FET. Third, the length of the p-depletion region, which defines the spatial resolution of the device, was estimated from the full width at half maximum (FWHM) of the conductance line profiles along the nanowire axis (**Fig. 2-4a**, inset traces) and found to be 210 nm. While

the size of the sensitive region without optimization is comparable to the best value reported in our previous work, we note that theoretical spatial resolution of a gated p-n device, characterized by the thickness of the depletion region, is 10-30 nm for highly doped silicon²⁸, and thus could be improved in the future.

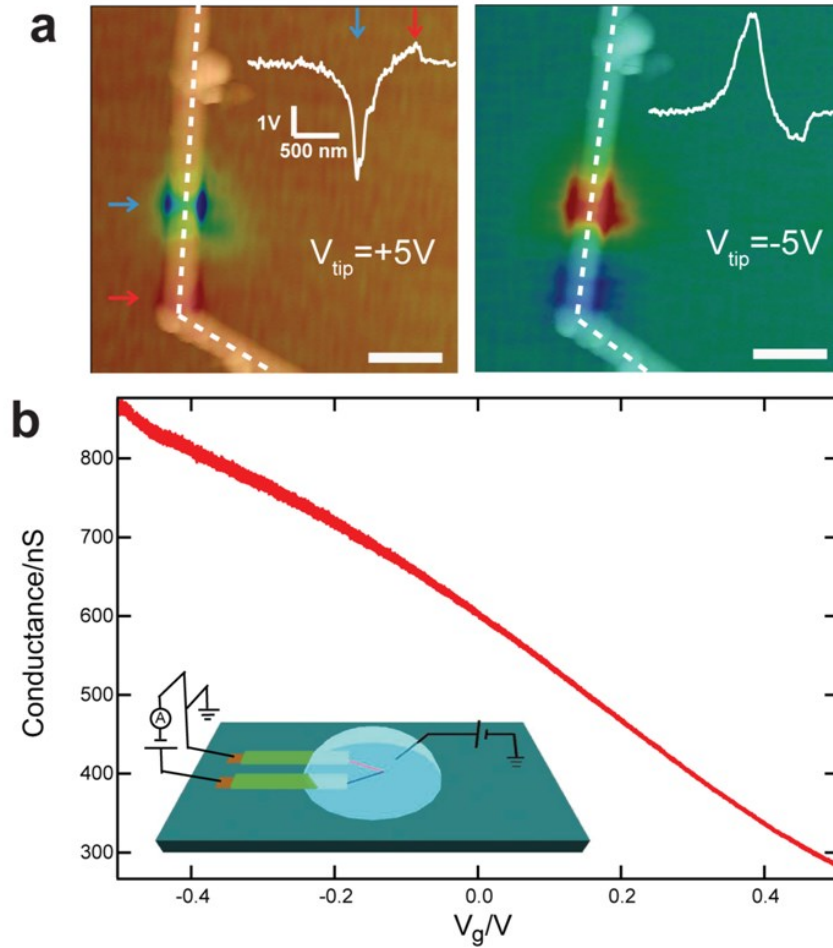


Figure 2-4. tmSGM and water-gate experiments of kinked p-n nanowire devices. a, Superposition of tmSGM images on AFM topographic images of a representative kinked p-n nanowire device under V_{tip} of +5 V (left, scanning direction from top down) and -5 V (right, scanning direction from bottom up), respectively. Scale bar, 0.5 μm . The blue/red arrows indicate the p-type and n-type depletion/accumulation regions (left panel), respectively; the same positions show accumulation/depletion in the right panel. Insets: Line profiles of the tmSGM signal along the white dashed lines about these p-type and n-type regions. **b,** Conductance versus water-gate reference potential data recorded from a

(Continued) representative kinked p-n nanowire device in $1\times$ phosphate buffer saline (PBS). Inset: Schematic of conductance vs. water-gate experiment.

The devices used for sensing experiments in solution were fabricated through multiple EBL, metallization and passivation steps similar to previous reports^{2,10,12}, using Cr/Pd/Cr for contacts and SU8 as the passivation layer to isolate the metal electrodes from the aqueous medium. The sensitivity of kinked nanowire p-n devices in solution was assessed by water-gate experiments^{2,10} (**Fig. 2-4b**, inset), where the p-n junction was forward biased at 1.0 V and a Ag/AgCl electrode was used to control the chemical potential (V_g) of the solution. Representative conductance versus V_g data (**Fig. 2-4b**) demonstrate a p-type response and sensitivity of 620 nS/V. The p-type response is consistent with the tmSGM results. The water-gate results also exhibit an increase in noise with increasing device conductance, which could be due to increased recombination at higher carrier concentrations within the depletion region²². From a practical perspective, such water-gate data can be used to choose an optimal operating regime (i.e., where the sensitivity/noise ratio is maximized), although future work should also address fundamental origin of noise in these p-n junction nanowire devices and potential reductions through, for example, improvements in junction quality and reduction of the surface defects.

2.3.5 Single charged nanoparticle sensing

Localized detection using our kinked p-n probes was first explored in single nanoparticle sensing experiments. Specifically, an array of kinked p-n nanowires probes on a SiO₂ substrate^{2,10,12} was coupled to PDMS microfluidic channel to control the solution flow over the devices. Conductance versus time traces recorded simultaneously from two independent devices following the introduction of a 1.2 nM solution of 100 nm diameter

charged fluorescent polystyrene nanobeads (**Fig. 2-5a**) exhibit several key features. First, when nanobeads solutions flow through the device area, uncorrelated ‘pulse’ (on/off) signals were observed from both devices (**Fig. 2-5a**, red traces). The time duration time of the ‘on’ state of the pulses ranged from 50 to 200 ms. Second, the conductance amplitudes of signals recorded on device-1 (D1) and device-2 (D2) were consistently 3-4 and 2-3 nS, respectively. The calibrated potential change (based on the water-gate sensitivity of the two devices) yields a consistent decrease of 5-6 mV at the p-n junction of both devices. This decrease in potential is also consistent with the negative charge on the nanobeads. Third, introduction of the aqueous solution without nanobeads (**Fig. 2-5a**, green traces) exhibited no on/off pulsed signals from either device even over much longer recording times. Together, these results are consistent with the detection of single nanobeads as outlined schematically in **Fig. 2-5b**. Briefly, when there is no nanobead close to the p-n junction within the Debye screening length, the conductance of the device remains constant (**Fig. 2-5b**, left image). When a nanobead approaches and/or attaches to the p-n junction, an increase of conductance will be observed due to the negative charges on the nanobead (**Fig. 2-5b**, middle image), and when the nanobead leaves the sensitive region of the probe, the conductance returns to baseline (**Fig. 2-5b**, right image).

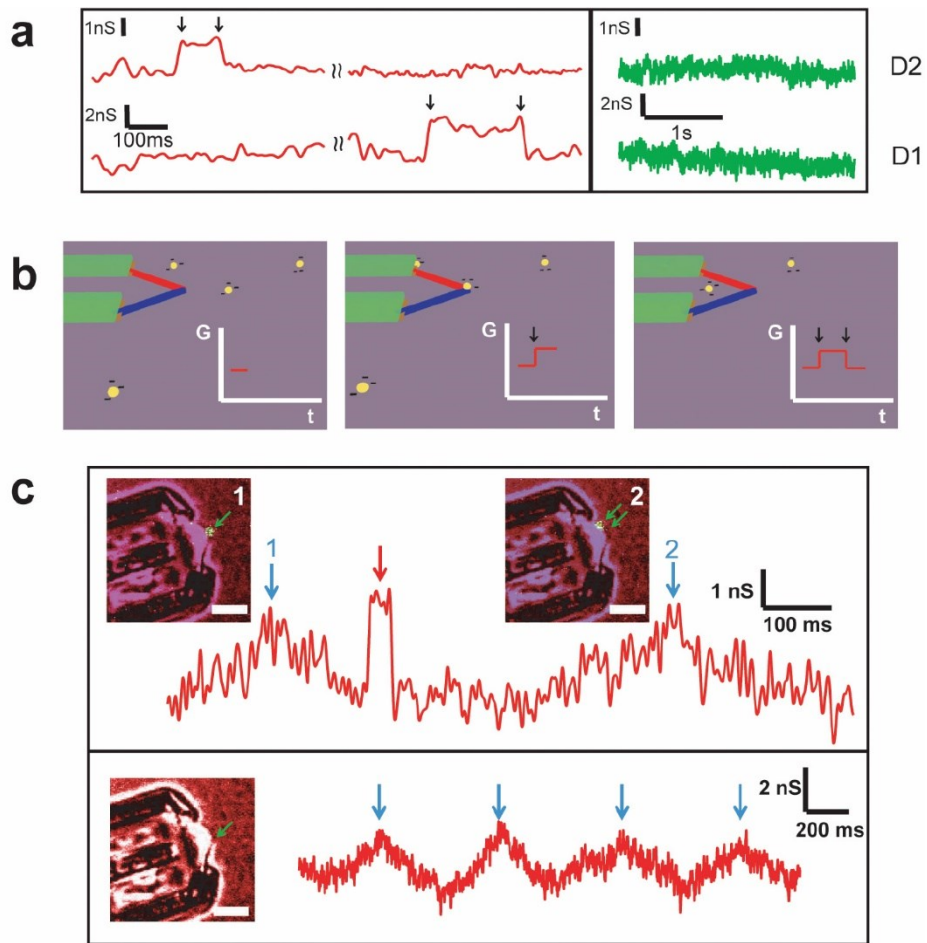


Figure 2-5. Fluorescent polystyrene nanobead sensing experiment. **a**, (Left) Conductance vs. time data recorded simultaneously from two independent kinked p-n nanowire devices with nanobeads in deionized water introduced into the microfluidic channel. Black arrows mark the on/off points of the signals. (Right) Conductance vs. time data recorded simultaneously from the same two devices with only deionized water in the microfluidic channel. **b**, Schematic of fluorescent polystyrene nanobead sensing process using kinked p-n nanowire devices and the corresponding schematic of time-dependent change in device conductance. Black arrows mark the on/off points of the signal. **c**, (Top) Simultaneous confocal microscopy and conductance vs. time data recorded from a kinked p-n nanowire device in a nanobead solution flow. Red arrow marks the charge sensing signal. Blue arrows mark the photocurrent peaks caused by the laser scanning over the p-n junction for images 1 and 2. The green arrows in the images highlight the positions of the nanowire junction and fluorescent nanobead in both images. In Image 1, the two green arrows overlap. (Bottom) Simultaneous confocal microscopy and conductance vs. time data recorded from the same device without nanobeads in solution. Blue arrows indicate photocurrent peaks due to the laser scanning over the p-n junction. The green

(Continued) arrow in the image highlights the position of the nanowire junction. All the electrical data were filtered through a 100 Hz low-pass digital filter. Scale bars, 5 μm .

To confirm this interpretation of the multiplexed electrical measurements we carried out simultaneous confocal fluorescent microscopy imaging and electrical recording in the presence and absence of the fluorescent nanobeads. Significantly, we find that a conductance pulse (**Fig. 2-5c**, red arrow) similar to that observed in measurements described above occurs when a single nanobead approaches the p-n junction at the elbow of the kink (**Fig. 2-5c**, inset-1) and then diffuses away (**Fig. 2-5c**, inset-2). The 50 ms wide conductance pulse is consistent with brief contact between the nanobead and the p-n junction during this process. We also note that when the laser scans over the p-n junction, there is a photocurrent (conductance increase) as indicated by blue arrows 1 and 2 (**Fig. 2-5c**), and this can be used to assign the times when each image is captured. In addition, when the same solution without fluorescent nanobeads was introduced into the device, only periodic photocurrent was observed (**Fig. 2-5c**, lower trace). These control experiments further confirm that conductance pulses correspond to single nanobead detection, and also highlight the potential of our p-n devices as point-like nanoscale photodetectors for biophysical studies and imaging.

2.3.6 Intracellular recordings

We have also configured the kinked p-n junction nanowires as 3D probes for highly localized interaction with living cells (**Fig. 2-6a**). The 3D p-n junction devices were fabricated using procedures similar to our previous studies² to yield nanowire probe oriented at 45-60° angle with respect to the substrate. In a typical experiment, the 3D p-n junction nanowire probes were functionalized with 1,2-dimyristoyl-sn-glycero-3-

phosphocholine (DMPC) bilayer and then embryonic chicken cardiomyocyte cells cultured on a PDMS sheet were positioned over a nanowire probe within a cell perfusion chamber². Representative conductance versus time data recorded from a spontaneously beating cardiomyocyte cell (**Fig. 2-6b**) show periodic spikes with the same frequency of the overall cell contraction, and an amplitude, shape and time scale of individual peaks characteristic of the intracellular action potential. Specifically, a reproducible fast onset of over 60 mV increase in local potential is observed followed by a broad slow return to baseline within 200 ms, which is consistent with the intracellular action potentials recorded using a patch-clamp²⁹. These results show that the nanoscale p-n diode sensor can be internalized by the cell. In addition, we find that these nanowire p-n junction probes can be inserted and retracted multiple times from the same cell without losing key features of the intracellular action potential or loss of cell viability, highlighting the minimal invasiveness of these nanoscale probes. We note that the highly localized nature of our p-n kinked probe could enable detailed studies of the potential distribution within the cell and in subcellular structures. However, the current probe design does not provide sufficient control of the probe-cell position for such experiments due to the flexibility of the floating PDMS cell substrate.

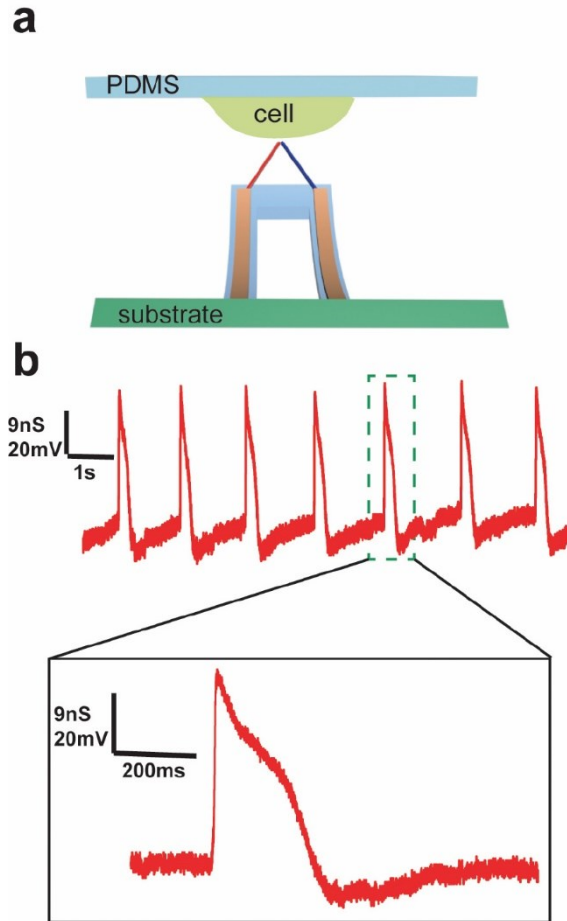


Figure 2-6. Intracellular electrical recording from spontaneously beating chicken cardiomyocytes. **a**, Schematic of intracellular recording from spontaneously beating embryonic chicken cardiomyocytes cultured on PDMS substrate using 3D kinked p-n nanoprobes. **b**, (Top) Steady-state intracellular recording using a 3D kinked p-n nanoprobes from a spontaneously beating cardiomyocyte cell. (Bottom) Zoom of the single action potential peak from the green-dashed region.

2.4 Conclusion

We have demonstrated for the first time that a nanoscale axial p-n junction synthetically embedded in a kinked nanowire structure can be tuned to work as a highly localized field-effect sensor to detect charges down to a single nanoparticle level, and to record full intracellular signals of spontaneously beating cardiomyocyte cells. Compared to previously reported nanoFET probes², this gateable p-n diode device represents a new

family of nanoscale biosensor probes with several unique advantages, including (1) a highly localized sensing region that can be tuned simply by optimizing the doping levels of the p- and n-arms, (2) the possibility of yielding different types of field-effect sensors (i.e., p-type, n-type and ambipolar) by tuning the relative doping ratio between the p- and n-arms, and (3) the potential of using the p-n junction as a 3D nanoscale photodetector, for example, to study highly localized fluorescent events when integrated within living cells and tissue.

2.5 Bibliography

1. Timko, B. P., Cohen-Karni, T., Qing, Q., Tian, B. & Lieber, C. M. *IEEE Trans. Nanotechnol.* **9**, 269 (2009).
2. Tian, B. *et al. Science* **329**, 831 (2010).
3. Tian, B. *et al. Nature* **449**, 885 (2007).
4. Kempa, T. J. *et al. Nano Lett.* **8**, 3456 (2008).
5. Tian, B. Z., Xie, P., Kempa, T. J., Bell, D. C. & Lieber, C. M. *Nat. Nanotech.* **4**, 824 (2009).
6. Xu, S., Qin, Y., Xu, C., Wei, Y., Yang, R. & Wang, Z. L. *Nature Nanotech.* **5**, 366 (2010).
7. Yan, H. *et al. Nature* **470**, 240 (2011).
8. Dick, K. A. *et al. Nat. Mater.* **3**, 380 (2004).
9. Jiang, X. *et al. Proc. Natl. Acad. Sci. USA* **108**, 12212 (2011).
10. Qing, Q. *et al. Proc. Natl. Acad. Sci. USA* **107**, 1882 (2010).
11. Cohen-Karni, T., Timbo, B. P., Weiss, L. E. & Lieber, C. M. *Proc. Natl. Acad. Sci. USA* **106**, 7309 (2009).
12. Cohen-Karni, T., Qing, Q., Li, Q., Fang, Y. & Lieber, C. M. *Nano Lett.* **10**, 1098 (2010).
13. Heller, I., Smaal, W. T. T., Lemay, S. G. & Dekker, C. *Small* **5**, 2528 (2009).

14. Kotov, N. A. *et al. Adv. Mater.* **21**, 3970 (2009).
15. Patolsky, F. *et al. Science* **313**, 1100 (2006).
16. Lieber, C. M. *MRS Bull.* **36**, 1052 (2011).
17. Patolsky, F., Timko, B. P., Zheng, G. F. & Lieber, C. M. *MRS Bull.* **32**, 142 (2007).
18. Timko, B. P. *et al. Nano Lett.* **9**, 914 (2009).
19. Pui, T. S., Agarwal, A., Ye, F., Balasubramanian, N. & Chen, P. *Small* **5**, 208 (2009).
20. Eschermann, J. F. *et al. Appl. Phys. Lett.* **95**, 083703 (2009).
21. Stern, E. *et al. Nature* **445**, 519 (2007).
22. Sze, S. M. *Semiconductor devices, physics and technology*. Singapore: Wiley, 2002.
23. Gudlksen, M. S., Lauhon, L. J., Wang, J., Smith, D. C. & Lieber, C. M. *Nature* **415**, 617 (2002).
24. Lauhon, L. J., Gudlksen, M. S., Wang, D. & Lieber, C. M. *Nature* **420**, 57 (2002).
25. Wilson, N. R. & Cobden, D. H. *Nano Lett.* **8**, 2161 (2008).
26. Cui, Y., Zhong, Z., Wang, D., Wang, W. U. & Lieber, C. M. *Nano Lett.* **3**, 149 (2003).
27. Rusu, A. & Bulucea, C. *Proc. Rom. Acad.* **10**, 285 (2009).
28. Weber, L. & Gmelin, E. *Appl. Phys. A* **53**, 136 (1991).
29. Zipes, D.P. & Jalife, J. *Cardiac Electrophysiology: From Cell to Bedside*. Philadelphia, PA: Saunders, 2009.

Chapter 3. Design and synthesis of diverse functional kinked nanowire structures for nanoelectronic bioprobes

3.1 Introduction

The rational design and synthesis of semiconductor nanowire building blocks with controlled structures have enabled the bottom-up fabrication paradigm with unprecedented flexibility to construct nanoelectronic and nanophotonic devices¹⁻⁸. The development of nanowire structures from basic 1D⁹⁻¹¹ through 2D and 3D^{2,12-14} enables novel spatial and functional configurations of devices that have proven especially advantageous in developing nanoelectronic interfaces with biological systems¹³⁻²¹. In particular, functional kinked nanowires in which nanoFETs or field sensitive p-n diodes are synthetically integrated in kinked nanowire superstructures, have been used to fabricate 3D bend-up nanoelectronic probes to record extra- and intracellular action potentials from single cells and tissues^{14,20}. In these nanobiosensors, the development of topological and compositional control in silicon nanowires has enabled the synthesis and fabrication of single-detector probes from single 60° or 120° kinked nanowires where the nanoscale detector is ‘presented’ away from supporting substrates and bulky metal interconnects. However, the synthetic demonstration of more (i) complex nanowire geometries, including multikinked and zigzag shaped nanowires^{14,20,22-31}, and (ii) multiple nanoFETs within single 1D nanowires^{19,32} promise a rich combination of device designs that could open up distinct sensing applications. To realize this opportunity requires that several fundamental questions be addressed, including: (1) Can the probe size be reduced while at the same time

being ca. size-independent away from the tip so that deep insertions are even less invasive; and (2) can ab initio design and subsequent synthetic be used to realize functional multiplexed kinked nanowire device arrays with defined geometry and topology? In this chapter, we address these questions and substantially expand the scope of functional kinked nanowires building blocks through the ab initio design and synthesis of several new structures.

3.2 Experimental

3.2.1 Kinked nanowire synthesis

The three types of functional kinked nanowires described in this chapter were synthesized as follows. (1) The U-shaped kinked nanowires were synthesized by CVD through a nanoparticle-catalyzed VLS process as described previously²⁰. Specifically, 30 nm, 80 nm or 150 nm diameter gold nanoparticles (Ted Pella) were dispersed on Si growth substrates with 600 nm SiO₂ layer (Nova Electronic Materials). Growth of heavily phosphorous-doped n-type arm was first carried out by feeding SiH₄ (1 sccm, 99.9999%), PH₃ (4 sccm, 1000 ppm in H₂) and H₂ (60 sccm) into the system (atom ratio of Si:P is 250:1) for 16 min at a total pressure of 40 torr and temperature of 460 °C. The growth was then paused for 15 s to introduce one 120° kink, by rapidly evacuating the chamber to lowest pressure and shutting off the gas lines. The following two 120° *cis*-kinks were introduced via the same procedure, with a 40-100 s growth time between every two *cis*-linked kinks. To grow the lightly doped n-type FET segment between the second and the third 120° *cis*-kinks at the tip, the flow rates of SiH₄ (99.9999%) and PH₃ (1000 ppm in H₂) were 1 sccm and 0.5 sccm (atom ratio of Si:P is 2000:1, for 30 nm diameter nanowires) or 1 sccm and 0.1 sccm (atom ratio of Si:P is 10,000:1 for 80 nm and 150 nm diameter

nanowires). Finally, the second heavily doped n-type arm was allowed to finish in additional 16 min. (2) Series multi-nanoFET kinked nanowires were grown with reactant gas flow rates, total gas pressure and growth temperature the same to U-shaped kinked nanowires described in (1). Initially, the first heavily doped n^{++} arm (atom ratio of Si:P is 250:1) was grown for 30 min, and the reactor was then evacuated for 15 s to introduce a 120° kink, then the n^{++} tip segment was grown for 20 s followed by evacuating the reactor for 15 s again to introduce another 120° *cis*-linked kink. The lightly-doped nanoFET segments (atom ratio of Si:P is 10,000:1) with intentionally varied distance were grown and encoded in the second n^{++} arm, in which the growth time for each nanoFET element was 45 s, and growth times for the n^{++} segment between two adjacent nanoFETs were 85, 170, and 340 s, respectively. The total growth time of the second arm was 30 min. Dopant modulation was achieved by varying the flow rates of PH_3 (1000 ppm in H_2) at 4 sccm and 0.1 sccm for heavily doped n^{++} - and lightly doped n-type segments respectively and kept the flow rates of SiH_4 (1 sccm, 99.9999%) and H_2 (60 sccm) constant. (3) The growth temperature and reactant gas pressures of parallel-nanoFET multi-kinked nanowires were the same to U-shaped kinked nanowires described in (1). Specifically, using 150 nm diameter gold catalysts, the four heavily doped n^{++} arms (atom ratio of Si:P is 250:1) were grown for 6-18 min respectively (Initial arm was grown 10 min longer than other three arms) and every adjacent arms were connected by a 60° tip constructed from two *cis*-linked 120° kinks. Lightly doped nanoFET elements (atom ratio of Si:P is 10,000:1) with growth time of 45 s were introduced immediately after each probe tip growth. Dopant modulation was achieved by varying the flow rates of PH_3 (1000 ppm in H_2) at 4 sccm and 0.1 sccm

for heavily doped n^{++} - and lightly doped n-type segments, respectively, and the flow rates of SiH_4 (1 sccm, 99.9999%) and H_2 (60 sccm) were kept constant.

3.2.2 KOH selective wet etching

We used KOH selective wet etching to analyze the doping profile of the kinked nanowires encoded with nanoFETs. Briefly, 10 g of KOH (Sigma-Aldrich Inc.) were dissolved in 88 mL deionized H_2O and 37 mL isopropanol. Substrates with dispersed nanowires were dipped in buffered hydrogen fluoride (BHF) solution (Transene Company Inc.) for 10 s followed with deionized H_2O rinse and then immediately dipped in this KOH solution for 3-10 s at 50-60 °C. The substrates were rinsed with deionized H_2O , followed with isopropanol rinse and N_2 blow drying.

3.2.3 Bend-up probe fabrication

The bend-up probes were fabricated on Si substrates (Nova Electronic Materials, n-type 0.005 Ω cm) with 600 nm SiO_2 layer. A nickel sacrificial layer (100 nm) was first defined by EBL and thermal evaporation. The substrate was then coated with SU8 resist (2000.5, MicroChem Corp.), on which the as-synthesized kinked nanowires suspended in ethanol were deposited. After definition of the bottom SU8 support layer by EBL, source/drain (S/D) metal contacts were defined by EBL and metalized by thermal evaporation of Ti/Pd/Ti (1.5/120/60 nm). Typically, the S/D contact separation was 0.5–1 μm for U-shaped kinked nanowire probe and 10-15 μm for V-shaped kinked nanowire probe, and the free end of the nanowire extended 3–4 μm from the source contact. The top SU8 layer was subsequently defined by EBL for passivation. Etching of the nickel sacrificial layer (~1 h) in nickel etchant (TFB, Transene Company, Inc.) yielded the 3D bend-up probes.

3.2.4 Device water-gate characterization

The water-gate measurements were carried out in $1\times$ PBS. An Ag/AgCl wire was used as a reference electrode. The kinked nanowire device conductance was measured with dc bias set to 0.1 V, and the current was converted to voltage with a current preamplifier (Model 1211, DL Instruments) at sensitivity of 10^{-6} A/V, before low-pass filtered (0-6 KHz, CyberAmp 380, Molecular Devices), and digitized at 20 kHz sampling rate (Axon Digi1440A, Molecular Devices).

3.2.5 Scanning gate microscopy characterization

The device chip was mounted on a BioScope MultiMode SPM stage (Digital Instrument). The S/D voltage across the device was kept constant at 0.1 V, and S/D current was measured using a low-noise differential preamplifier (SR560, Stanford Research Systems). The device conductance was calculated from S/D voltage and current. A conductive AFM tip (PPP-NCHPt, Nanosensors) was used as a local gate and scanned over the device to map the conductance image in “Lift Mode”. Specifically, first, for each scan line, zero potential was applied to the tip, and a topographic image was acquired in Tapping Mode with feedback enabled. The tip was then lifted up 30 nm, and a tip potential of ± 10 V was applied. The tip was scanned across the same line again following the captured topological profile with feedback turned off, when the change of conductance of the device was recorded.

3.3 Results and discussion

3.3.1 Material designs and potential applications

Novel functional kinked nanowire building blocks are designed for potential biological applications as illustrated schematically in **Fig. 3-1**. First, we designed U-shaped kinked nanowires as compact, high aspect ratio probes (**Fig. 3-1a**), where three 120° *cis*-kinks can define the “U”, dopant modulation between two of these kinks defines nanoFET detector, and heavily-doped (parallel) arms before/after the three kinks function as nanoscale S/D connections to the FET. The width of this U-shaped kinked nanowire design is constant, determined by interkink segment lengths, and independent of the length of the arms. This design allows in principle deep penetration of the nanoFET detector into cells and tissue without increasing the cross-sectional area. Second, we have expanded upon our original V-shaped kinked nanowire with single detector by devising two approaches for encoding multiplexed nanoFET detectors (**Fig. 3-1b**), where (i) dopant modulation is used to encode multiple FETs with controlled position and size along a single arm of a V-shaped kinked nanowire with the “V” defined by 1 or 2-*cis* 120° kinks, and (ii) dopant modulation is used to encode multiple FETs in distinct arms of W-shaped kinked nanowires. These designs would allow for series and/or parallel multiplexing of intracellular/extracellular recording from a single nanobioprobe.

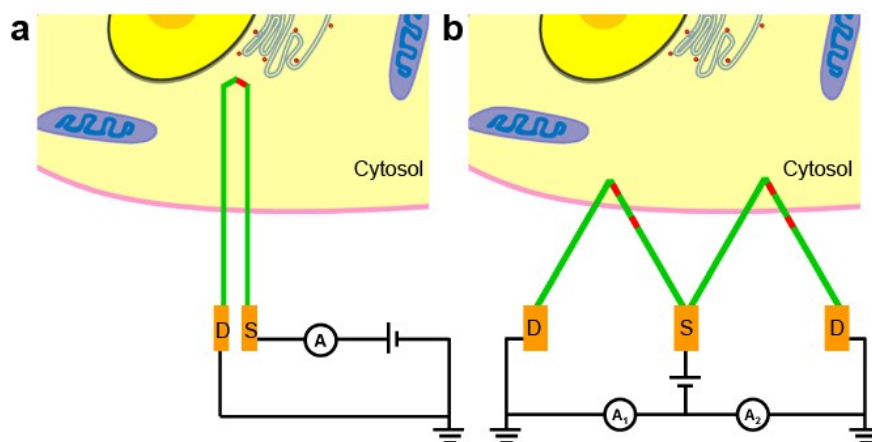


Figure 3-1. Overview of kinked nanowire synthetic designs and potential applications. **a**, U-shaped kinked nanowire with integrated nanoFET (red) shown as a bioprobe for intracellular recording. **b**, W-shaped kinked nanowire with multiple nanoFETs (red) illustrated as a bioprobe for simultaneous intracellular/extracellular recording. In **a** and **b**, green indicates heavily-doped (n^{++}) S/D nanowire nanoelectrode arms, red highlights the pointlike active nanoFET elements, and gold indicates the fabricated metal interconnects to the nanowire S/D arms. A schematic of a cell to scale is drawn with the different device designs to show the potential for achieving minimally invasive deep penetration (**a**) and multiplexed intracellular and extracellular recording (**b**).

3.3.2 Synthesis and characterization of U-shaped kinked nanowires

The kinked nanowires were prepared using gold-nanoparticle catalyzed VLS growth method with doping and geometric control adapted from our previous reports²⁰. For the U-shaped kinked nanowires (**Fig. 3-2a**), the initial heavily-doped n^{++} straight arm was grown at 460 °C using 80 nm gold nanoparticles as the catalyst. Following typical 16 min arm growth (growth rate ca. 750 nm/min), the U-shape probe end was begun by introducing two 120° *cis*-kinks sequentially with the intervening nanowire segment grown for 100 s. After the second kink was initiated (by evacuation of the growth chamber), the nanoFET was encoded by reducing the phosphine dopant by 97.5% (from that used to prepare the heavily doped arms and initial turn of the “U”) and growing a second segment for 100 s.

Last, a third 120° *cis*-kink to complete the U-shaped end of the probe was introduced and the other S/D arm was grown with the phosphine concentration at the initial high doping level.

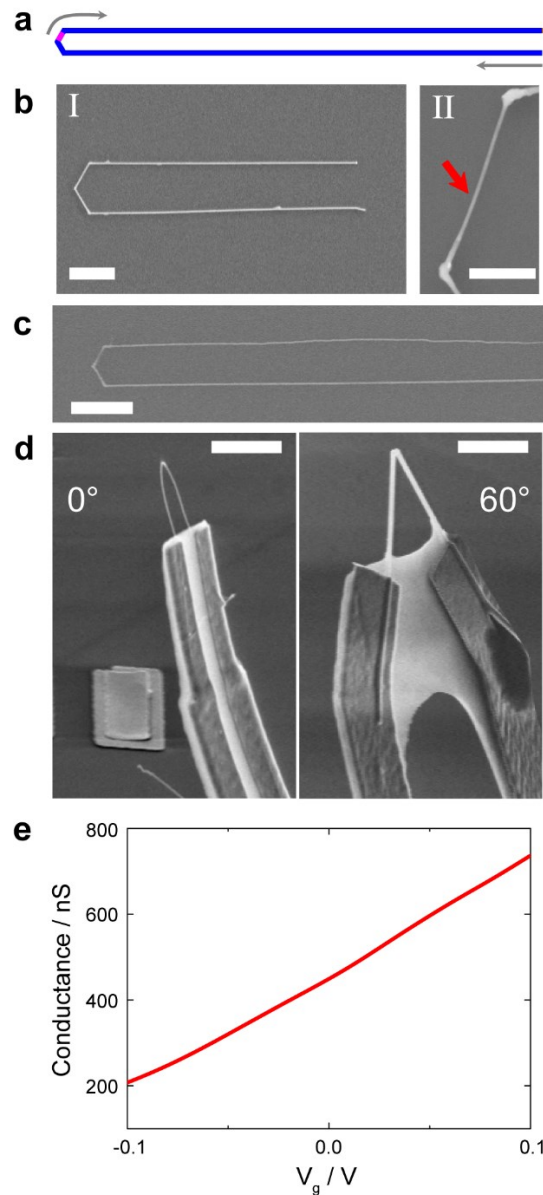


Figure 3-2. U-shaped kinked nanowires. **a**, Schematic of a U-shaped kinked nanowire with tip constructed from three 120° *cis*-linked kinks. The lightly-doped n-type nanoFET element (pink) is encoded at the tip and connected by heavily-doped n^{++} S/D arms (blue). The gray arrows indicate the growth sequence for the nanostructure. **b**, SEM images of original (I: scale bar, $2\ \mu\text{m}$) and KOH-etched (II: scale bar, $500\ \text{nm}$) U-shaped kinked nanowire synthesized with $80\ \text{nm}$ diameter gold nanoparticle catalysts. The red arrow

(Continued) marks the position of nanoFET element between the second and the third *cis*-linked kinks. **c**, Representative SEM image of a U-shaped kinked nanowire prepared using 30 nm diameter gold nanoparticles. The measured nanowire diameter is 30 nm. Scale bar, 1 μm . **d**, SEM images of 3D probe devices fabricated using a 30 nm diameter U-shaped (left) and 150 nm diameter V-shaped (right) kinked nanowire building blocks. Scale bars, 3 μm . **e**, Conductance versus water-gate reference potential data recorded from a representative 30 nm diameter U-shaped kinked nanowire 3D probe in $1\times$ PBS.

An SEM image of a typical Si kinked nanowire synthesized using the above procedure (**Fig. 3-2b**, I) shows several key features. First, the overall U-shaped structure is obtained as a result of the *cis*-orientation of the three 120° kinks, including uniform parallel arms separated by ca. 2.1 μm . Second, the lengths of the two segments separating the kinks, 1.3 μm , which determines the observed arm separation, and the overall arm lengths, 12 μm , are consistent with programmed growth times during synthesis, thus showing that we could implement design changes in systematic manner (e.g., changing arm separation). To verify the designed dopant variation, which encodes the nanoFET detector, the U-shaped Si kinked nanowires were etched with KOH solution, where the KOH yields enhanced Si nanowire etching rates in regions with lower n-type dopant concentration^{11,19}. An SEM image of the U-end of the same kinked nanowire after etching (**Fig. 3-2b**, II) shows clearly the smaller nanowire diameter between the second and the third kinks and is thus consistent with the design and synthesis. The generality of this new kinked nanowire structure was further explored with the synthesis using a $2.7\times$ smaller diameter gold nanoparticle catalyst. A representative SEM image (**Fig. 3-2c**) highlights this structure, where the separation between parallel 30 nm diameter arms of the “U” was reduced to only 650 nm. Overall, the yield of U-shaped kinked nanowire structures grown with both 80 and 30 nm catalysts was ca. 20%. Other “impurity” structures observed were straight or V-

shaped nanowires, thus suggesting that the kink yield (not *cis/trans* yield) is the factor that should be addressed to improve overall yields in the future.

We have used U-shaped kinked nanowires to fabricate 3D devices to compare this new building block to previous V-shaped kinked nanowire nanoprobe and to characterize the electrical properties in solution. 3D devices were fabricated using stressed metal interconnects that bend the kinked nanowire probes upward after relief from the substrate^{20,33}. Representative SEM images of U-shaped and V-shaped 3D kinked nanowire probes (**Fig. 3-2d**) highlight the advantage of the U-shaped kinked nanowire for reducing overall probe cross-section as a function of distance from the probe end. Specifically, the U-shaped probe is no more than $\sim 1 \mu\text{m}$ in width at the point of the metal interconnects (3 μm total tip to contact length) compared to $\sim 4 \mu\text{m}$ width at similar point for the 60° V-shaped probe, and moreover, the total widths of the metal connections at the two kinked nanowire probes were $< 3 \mu\text{m}$ (U-shape) and $\sim 10 \mu\text{m}$ (V-shape). In addition, the U-shaped kinked nanowire probes could be further reduced in width through synthesis as discussed above and using higher resolution EBL, while size reductions for the V-shaped probes are limited by structural geometry. In this regard, the U-shaped 3D kinked nanowire probes provide a better option for applications where deep insertion is desired. Second, the sensitivities of the nanoFET detectors encoded in the 3D U-shaped kinked nanowire probes were assessed in aqueous solution²⁰. Representative conductance versus water-gate (Ag/AgCl electrode) data (**Fig. 3-2e**) yields a relatively linear n-type FET response with a sensitivity of $2.7 \mu\text{S/V}$. Measurements on several U-shaped probes yields sensitivity values from ca. $1\text{--}10 \mu\text{S/V}$ and noise from ca. $1\text{--}4 \text{ mV}$ ($0\text{--}6000 \text{ Hz}$ bandwidth), thus showing the capability to record both intracellular and extracellular signals from electrogenic cells.

3.3.3 Synthesis and characterization of V-shaped kinked nanowires with series nanoFET

In addition, we have used the V-shape kinked nanowire motif as a starting point to explore the integration of multiple nanoFETs to enable multiplexed 3D bioprobes. The multiple nanoFETs were encoded in series along one arm of V-shaped kinked nanowires (**Fig. 3-3a**, inset) by dopant modulation, where the overall yield of V-shaped kinked nanowires was ca. 40%. A dark-field optical image of KOH-etched V-shaped kinked nanowire with 4 nanoFETs grown for 45 s/each and heavily-doped segment growth times (between every two adjacent nanoFETs) following the initial nanoFET of 85, 170 and 340 s is shown in **Fig. 3-3a**, where the KOH preferentially etches the lightly doped nanoFET regions^{11,19}. The dark-field image shows clearly the 4 encoded nanoFETs (dark contrast) with ca. the same length, and moreover, shows that separation between nanoFETs along the arms increases as expected from the segment growth times. The nanoFET channel lengths and separations were quantified using SEM images (**Fig. 3-3b,c**), which yield FET lengths of 540, 550, 530, and 530 nm (from the kinked nanowire tip), and separations of 1.05, 2.03, and 4.08 μm . These results are consistent with the calibrated growth rate of ~ 700 nm/min, and demonstrate the capability for sophisticated bottom-up encoding of multiplexing function within the kinked nanowire building blocks.

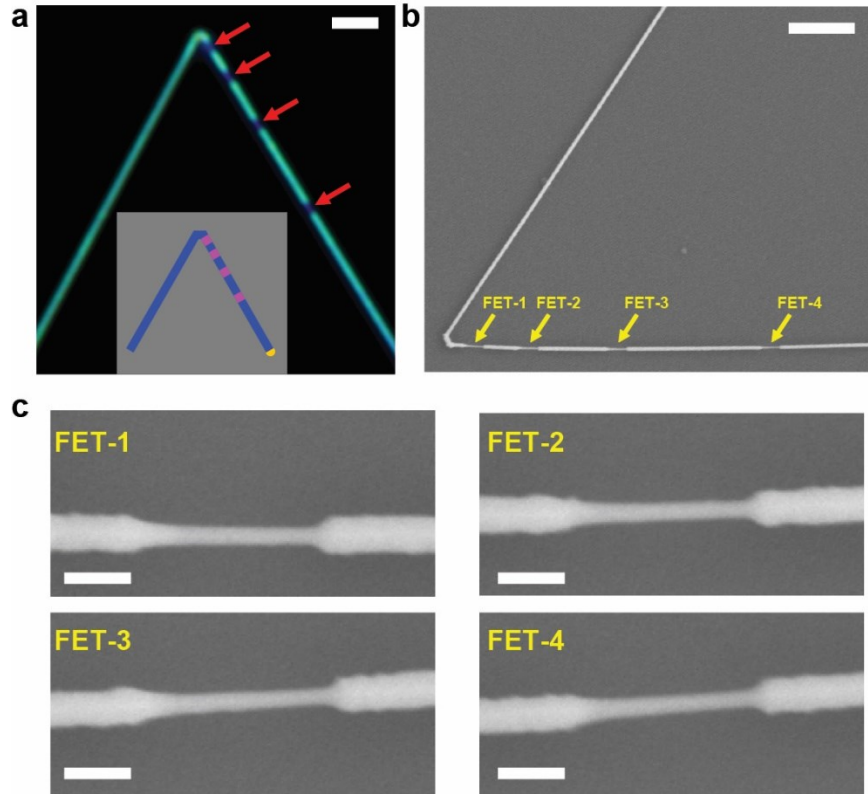


Figure 3-3. Series nanoFET in V-shaped kinked nanowires. **a**, Dark-field optical microscopy image of a KOH-etched kinked nanowire with 4 nanoFETs. The dark segments correspond to the four lightly doped nanoFET elements (red arrows). Scale bar, 2 μm . Inset: schematic of the synthetic design for the kinked nanowire with 4 series nanoFETs (pink) and heavily-doped connecting nanowire segments (blue). **b**, Representative SEM image of a KOH-etched series multi-nanoFET kinked nanowire. The segments with smaller diameter correspond to preferentially-etched lightly-doped nanoFET elements. Scale bar, 2 μm . **c**, Magnified images of the 4 nanoFET elements marked with arrows in **b**. Scale bars, 200 nm.

The electrical characteristics of the series nanoFETs encoded in the arms of V-shaped kinked nanowires were characterized using SGM³². Representative SGM and AFM images of a kinked nanowire device with four nanoFETs in series (**Fig. 3-4 a-c**) highlight several key features. First, only the synthetically defined lightly doped regions showed gate response, indicating that the four series nanoFETs in this individual kinked nanowire can work independently as localized nanosensors. Second, the lengths of the lightly doped

regions estimated from the FWHM of the conductance line profile along the nanowire axis (**Fig. 3-4d**) obtained from SGM were 502, 505, 510, and 505 nm, respectively. We note that these channel lengths calculated from SGM data agreed well with the results measured from KOH etched SEM images. Third, the positions of the SGM signal peaks matched the location of the four lightly doped FET elements revealed by KOH wet etch. Fourth, the amplitude variations determined from the SGM peaks suggest that sensitivity of the 4 distinct nanoFETs are within a factor of 2–3 of each other with the largest variation arising for the nanoFET closest to the tip of the kinked nanowire device. While further synthetic optimization should allow for series devices with comparable sensitivities to be prepared, taken together, the results demonstrate excellent bottom-up control of doping profile, active channel lengths, and positions of nanoFET elements in the kinked nanowire structures.

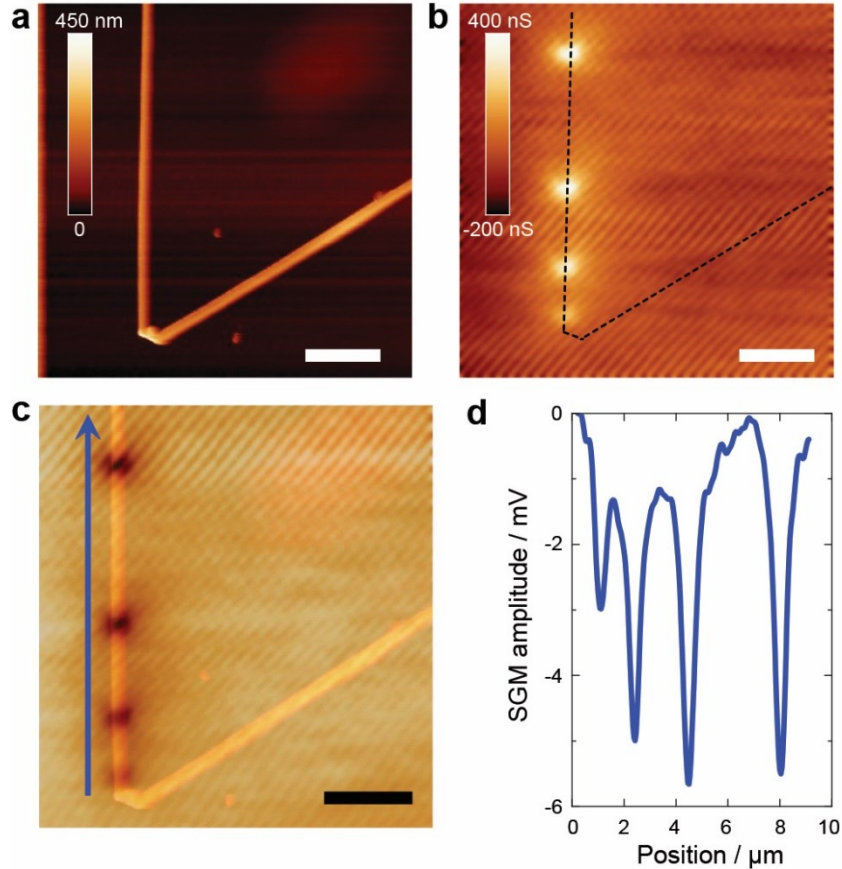


Figure 3-4. SGM characterization of V-shaped kinked nanowires. **a**, AFM image of series multi-nanoFET kinked nanowire. Scale bar, 2 μm . Color scale (0 to 450 nm) corresponds to the z-height of the image; the kinked nanowire is ~ 150 nm in diameter. **b**, Corresponding SGM image of the multi-nanoFET kinked nanowire in **a** with V_{tip} of +10 V. Scale bar, 2 μm . The bright regions in SGM image correspond to increased nanowire conductance. Color scale (-200 to 400 nS) corresponds to the conductance change. **c**, Superposition of SGM and AFM topographic images of the multi-nanoFET kinked nanowire in **a** with V_{tip} of -10 V. Scale bar, 2 μm . Dark regions in SGM image correspond to reduced nanowire conductance. **d**, Line profile of the SGM signal along the nanowire arm indicated by the blue arrow in **c**. The negative peaks correspond to the dark regions in SGM image.

3.3.4 Synthesis and characterization of W-shaped kinked nanowires with parallel nanoFET

Last, we have extended the topological complexity of the original V-shaped kinked nanowire by designing and synthesizing W-shaped kinked nanowires where one nanoFET

detector is encoded at the tips of each of the two “Vs” making up the W-shaped structure (Fig. 3-5a, inset). In this manner, independent, parallel multiplexing with a single probe can be implemented (see below). The key structural feature needed to realize the W-shaped building block is *trans*-oriented kink at the central bend of the “W” relative to the two *cis*-kinks that define each of the V-shaped tip components of the structure. An SEM image of a W-shaped nanostructure (Fig. 3-5a) highlights several key points. First, all of the bends defining the W-shape are defined by 60° angles at defined positions during growth. Second, each of the three 60° angles was introduced with two 120° *cis*-kinks with controlled tip widths of ca. 200 nm. Third, the 120° kinks separated by the ca. 4.5 μm arms have a *trans*-orientation as required to realize the “W” structure; we note that this is consistent with previous studies²⁰ that showed a higher yield of *trans* linkages were realized as the separation between 120° kinks was increased. Last, the overall yield of the W-shaped structure was ca. 10%, where other “impurity” structures typically had few numbers of kinks. This result suggests that as with the U-shaped probes overall yield could be improved in the future by increasing the yield of kink formation.

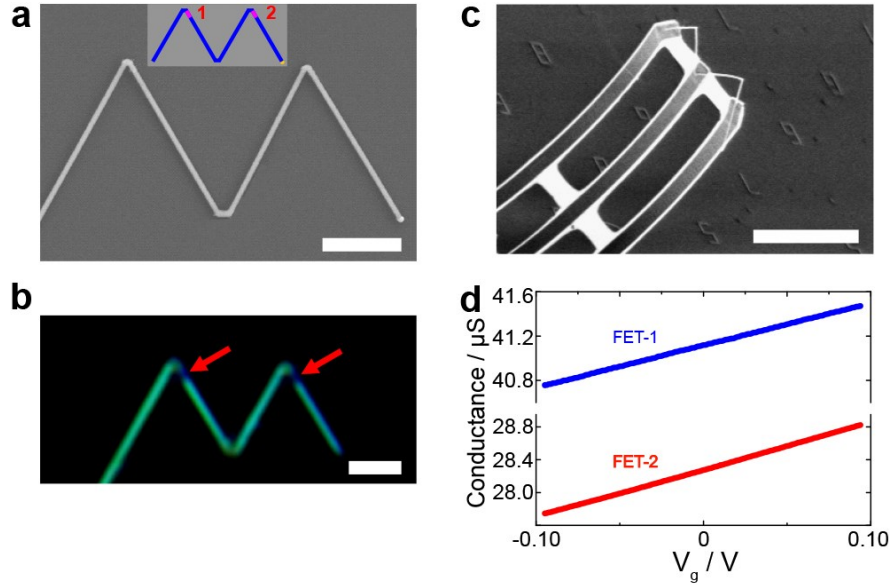


Figure 3-5. Parallel nanoFET kinked nanowires. **a**, SEM image of a W-shaped parallel-nanoFET kinked nanowire. Scale bar, 2 μm . Inset: Schematic of the W-shaped kinked nanowire with one nanoFET encoded at the tip of each V-shaped component of the “W”, where blue and pink indicate heavily-doped connections and lightly-doped nanoFET channels, respectively. **b**, Dark-field optical microscopy image of KOH etched W-shaped kinked nanowire. The two dark color segments correspond to the lightly doped nanoFET elements (red arrows) near the two tips. Scale bar, 2 μm . **c**, SEM image of W-shaped parallel-nanoFET kinked nanowire bend-up probe. Scale bar, 20 μm . **d**, Conductance versus water-gate reference potential data recorded independently from two parallel nanoFETs.

The positions of the nanoFETs encoded in the W-shaped were verified using the selective KOH etching described above. A representative dark-field optical microscopy image (**Fig. 3-5b**) shows clearly that there is one lightly-doped nanoFET at each probe tip and that the distance between the two nanoFET elements is ca. 4.5 μm . The spatial resolution of or separation between these parallel-nanoFETs, is determined by the length of the arms and the angle of the kinks. Currently the highest resolution is $\sim 3 \mu\text{m}$, although this could be further reduced to the submicrometer range by incorporating the zero-degree

kinked nanowires element at the central bend of the “W” or increased to ca. 10 μm by using a single 120° kink at this central bend.

To evaluate the multiplexing capability of the W-shaped kinked nanowire structures, we fabricated 3D probe devices where a common source connection was made to the central bend of the “W” and two independent drain connections were made to the outer arms of the structure. A representative SEM image of W-shaped kinked nanowire probe connected in this manner (**Fig. 3-5c**) shows that the probe bends upward uniformly from the substrate and presents both nanoFETs encoded in the two tips of the inverted “W” at the same height from the substrate. Water-gate measurements (**Fig. 3-5d**) showed that the sensitivities of the two nanoFETs were 3.8 and 5.7 $\mu\text{S/V}$, which are comparable to the performance of single-kinked nanowire probes²⁰. These results demonstrate that bottom-up designed parallel-nanoFETs in a single W-shaped kinked nanowire can work as independent multiplexed 3D nanosensors. We note that the key features of this unique multiplexed probe were all controlled during nanowire synthesis, which provides a potentially higher level of flexibility and precision compared to the post-growth assembly of single-detector kinked nanowire devices.

3.4 Conclusion

We have designed and synthesized in good yield three new types of functional kinked nanowires including (1) U-shaped kinked nanowire structures with two parallel heavily-doped arms connecting a nanoFET at the tip of the “U”, (2) series multiplexed functional kinked nanowire integrating multi-nanoFETs along the arm and at the tips of V-shaped structures, and (3) W-shaped multiplexed kinked nanowires integrating nanoFETs at the two tips of W-shaped structures. The U-shaped kinked nanowires were synthesized

with parallel arm separations as small as 650 nm and were used to fabricate 3D nanoFET probes at least three times smaller than previous V-shaped designs. Second, four nanoFETs were encoded in precise positions by synthesis in one arm/tip of V-shaped building blocks, and SGM measurements demonstrated that the series detectors had similar sensitivities that have potential for recording both extracellular and intracellular action potentials. Third, two nanoFETs were encoded in distinct arms of the new W-shaped kinked nanowire, and these building blocks were used to fabricate 3D nanoprobe capable of parallel multiplexing measurements using the independently addressable nanoFET detectors. The facile design and bottom-up synthesis of these diverse functional kinked nanowires provides a greatly expanded toolbox of building blocks for fabricating highly compact and multiplexed 3D nanoprobe for applications in life sciences, including (1) deep intracellular and deep tissue recordings with the ultrasmall U-shaped probes, (2) series multiplexed recording, for example for simultaneous intracellular and extracellular responses, using the new V-shaped probes having detectors spatially encoded along a single arm, and (3) parallel multiplexing, for example for simultaneous, independent recording of at least two intracellular signals from spatially defined positions within a single cell.

3.5 Bibliography

1. Lieber, C. M. *MRS Bull.* **36**, 1052 (2011).
2. Tian, B. & Lieber, C. M. *Pure Appl. Chem.* **83**, 2153 (2011).
3. Schmidt, V., Wittemann, J. V. & Gosele, U. *Chem. Rev.* **110**, 361 (2010).
4. Mai, L. *et al. Mater. Today* **14**, 346 (2011).
5. Wang, Z. L. *MRS Bull.* **37**, 814 (2012).

6. Wu, H. & Cui, Y. *Nano Today* **7**, 414 (2012).
7. Yang, P. *MRS Bull.* **37**, 806 (2012).
8. Wacaser, B. A. *et al. Adv. Mater.* **21**, 153 (2009).
9. Yan, H. *et al. Nature* **470**, 240 (2011).
10. Tian, B. *et al. Nature* **449**, 885 (2007).
11. Kempa, T. J. *et al. Nano Lett.* **8**, 3456 (2008).
12. Jiang, X. *et al. Proc. Natl. Acad. Sci. USA* **108**, 12212 (2011).
13. Duan, X. *et al. Nature Nanotech.* **7**, 174 (2012).
14. Jiang, Z., Qing, Q., Xie, P., Gao, R. & Lieber, C. M. *Nano Lett.* **12**, 1711 (2012).
15. Zheng, G., Patolsky, F., Cui, Y., Wang, W. U. & Lieber, C. M. *Nat. Biotechnol.* **23**, 1294 (2005).
16. Xie, C., Lin, Z., Hanson, L., Cui, Y. & Cui, B. *Nature Nanotech.* **7**, 185 (2012).
17. Yan, R. *et al. Nature Nanotech.* **7**, 191 (2012).
18. Gao, R. *et al. Nano Lett.* **12**, 3329 (2012).
19. Cohen-Karni, T. *et al. Nano Lett.* **12**, 2639 (2012).
20. Tian, B. *et al. Science* **329**, 831 (2010).
21. Qing, Q. *et al. Proc. Natl. Acad. Sci. USA* **107**, 1882 (2010).
22. Tian, B. Z., Xie, P., Kempa, T. J., Bell, D. C. & Lieber, C. M. *Nat. Nanotech.* **4**, 824 (2009).
23. Musin, I. R. & Filler, M. A. *Nano Lett.* **12**, 3363 (2012).
24. Lee, G. *et al. Angew. Chem. Int. Ed.* **48**, 7366 (2009).
25. Lugstein, A. *et al. Nano Lett.* **8**, 2310 (2008).
26. Madras, P., Dailey, E. & Drucker, J. *Nano Lett.* **9**, 3826 (2009).
27. Ben-Ishai, M. & Patolsky, F. *Nano Lett.* **12**, 1121 (2012).
28. Geaney, H. *et al. Cryst. Growth Des.* **11**, 3266 (2011).
29. Schwarz, K. W. & Tersoff, J. *Nano Lett.* **11**, 316 (2011).

30. Ross, F. M. *Rep. Prog. Phys.* **73**, 114501 (2010).
31. Kim, J. H. *et al. Nanotech.* **23**, 115603 (2012).
32. Yang, C., Zhong, Z. & Lieber, C. M. *Science* **310**, 1304 (2005).
33. Tian, B. *et al. Nat. Mater.* **11**, 986 (2012).

Chapter 4. Shape-controlled deterministic assembly of nanowires

4.1 Introduction

Interest in the assembly of nanowires has long been motivated by the development of bottom-up integrated nanodevices¹⁻¹². Existing assembly techniques¹⁻¹² can position and align straight nanowires, but have not yet demonstrated assembly of nanowires with other shapes. Moreover, bending nanowires into other shapes can result in novel properties and functions with wide applications in strain-engineering¹³, energy¹⁴, electronics¹⁵, photonics¹⁶⁻¹⁹, optoelectronics²⁰, piezotronics^{21,22}, ferroelectrics²³, superconductors²⁴, and mechanics²⁵. However, most work on shape manipulation of nanowires^{13-16,18,25} is limited to single nanowires and/or randomly assembled nanowires, and it remains challenging to precisely control nanowire shaping in large scale. In this chapter, we demonstrate a novel and unique technique combining “nanowire assembly” and “nanowire shaping”, starting from straight nanowires and using trenches with designed shapes to precisely anchor, bend and align nanowires to achieve large-scale, high-precision shape control and deterministic assembly of nanowires. We used shear force and pre-defined trenches to bend nanowires *in situ* into various shapes, including circular, rectangular, triangular and other more complex geometries, with average offsets of y - and x - coordinates of nanowires within ± 20 nm and ± 40 nm, deviation of radius of nanowire curvature within ± 40 nm, and misalignment angle within $\pm 1^\circ$. Moreover, unlike state-of-the-art post-growth nanowire assembly techniques^{1,4-8} in which assembly precision relies on trench or anchor pattern size, our method is less dependent on trench size, allowing us to use patterns with large

feature sizes for wafer-scale deterministic assembly of U-shaped nanowires with yield of ~90% on 432,990 sites. Furthermore, we show that the assembled U-shaped silicon nanowires can serve as building blocks to fabricate 3D bend-up nanowire FET probe arrays. We also demonstrate the guiding and manipulating of light through U-shaped cadmium sulfide (CdS) nanowire waveguides as integrated nanoscale photonic circuit elements. This shape-controlled deterministic nanowire assembly method opens up new opportunities for next generation nanowire-based device arrays on an industrial scale that use shape-controlled nanowires with unique functions and properties as novel building blocks.

4.2 Experimental

4.2.1 Nanowire synthesis

Silicon nanowires were synthesized using a gold nanoparticle-catalysed VLS process described previously⁶. Briefly, 10, 30 and 80 nm diameter gold nanoparticles (#15703, #15706, #15710, Ted Pella, Redding, CA) were dispersed on the SiO₂ surface of Si growth substrates (600 nm thermal SiO₂, Nova Electronic Materials, Flower Mound, TX). Nanowire growth was carried out at 450–460 °C at a total pressure of 40 Torr with silane (SiH₄, 99.9999%, Voltaix, Branchburg, NJ) as the silicon precursor, diborane (B₂H₆, 100 ppm in H₂, Voltaix, Branchburg, NJ) as the p-type dopant, phosphine (PH₃, 1,000 ppm in H₂, Voltaix, Branchburg, NJ) as the n-type dopant, and hydrogen (H₂, 99.999%; Matheson, Basking Ridge, NJ) as the carrier gas. Both p-type and n-type nanowires were used for nanowire assembly and device fabrication in this work. For p-type nanowire growth, the flow rates of SiH₄, B₂H₆ and H₂ were 2.5, 3 and 60 sccm, respectively. For n-type nanowire growth, the flow rates of SiH₄, PH₃ and H₂ were 1, 1 and 60 sccm,

respectively. Typical growth times of 1–2 h yielded nanowires with lengths of 40–80 μm . CdS nanowires were grown using gold nanoparticle catalysed growth, with nanoparticles dispersed as above and CdS (99.999%, Alfa Aesar, Ward Hill, MA) produced by thermal evaporation in the higher temperature zone upstream and growth in the lower temperature zone downstream. Specific CdS nanowire growth conditions were CdS evaporation temperature, 675°C, growth zone temperature, 600°C, H₂ carrier gas flow rate, 20 sccm, pressure, 2.7 mTorr, and growth time, 60 min.

4.2.2 Shape-controlled assembly

A range of target substrates were used in our studies, including Si wafers (Nova Electronic Materials, Flower Mound, TX) with SiO₂, Si₃N₄, gold, nickel (Ni) and SU8 polymer (SU8 2000.5, Microchem, Inc., Westborough, MA) surface layers. The substrate surface layer was cleaned by rinsing in isopropanol (IPA, Cleanroom® MB, KMG Electronic Chemicals, Inc., Houston, TX) for 30 s followed by nitrogen drying. Polymethyl methacrylate (PMMA, 950-C2, Microchem, Westborough, MA) for EBL or S1805 (Microchem, Westborough, MA) for PL was spin-coated. EBL or PL was used to define arrays of trenches with different shapes and widths from 0.5–5 μm . No additional surface modification followed exposure and development.

Shape-selective assembly of nanowire samples was carried out in a manner similar to previous shear-printing studies described elsewhere^{2,6}. Briefly, a target substrate patterned with an array of trenches was mounted onto a micromanipulator-controlled moveable stage, covered with mineral oil (#330760, viscosity $\nu \approx 70$ mPa•s, Sigma-Aldrich, St. Louis, MO), and then the growth substrate was brought into contact with the target substrate with controlled contact pressure (see values below). The target substrate was

moved at a constant velocity of ~ 5 mm/min with respect to the fixed nanowire growth substrate, and then the growth substrate was removed and the target substrate rinsed with octane (98%, Sigma-Aldrich, St. Louis, MO) to remove the lubricant. To assemble the more complex nanowire geometries in two steps, we first patterned a resist trench on a receiving substrate using EBL or PL as described above. Next, nanowires were transferred from the growth substrate to the receiving substrate in direction 1 relative to the trenches. The substrate was rinsed with octane as described above, rotated 90° on the micromanipulator stage such that the transfer direction was aligned with direction 2, and then a second transfer was performed, again following the same conditions as described above. The minimum radius of nanowire curvature achievable by this process was determined by using ca. 200 nm radius of curvature trenches for 80 and 30 nm diameter silicon nanowires, and 151.9 ± 1.1 nm (mean \pm standard deviation) diameter gold nanoparticles (#15712, Ted Pella, Redding, CA; size statistics obtained from the vendor's characterization of 100 particles with transmission electron microscopy (TEM)) for 10 nm diameter silicon nanowires. Shape-controlled assembly of CdS nanowires was carried out similarly to that for Si nanowires.

4.2.3 TEM sample preparation and characterization

Arrays of U-shaped silicon nanowires with different radii of curvature were prepared for TEM characterization by fixing the arms of the assembled wires between Au metal layers while leaving the suspended nanowire tips exposed for imaging (**Fig. 4-1**). We introduced gold layers on both top and bottom of PMMA patterned for assembly as follows. (1) A Ni sacrificial layer (100 nm) was deposited on an oxidized silicon substrate by thermal evaporation. (2) A square mesh gold ribbon network (100 nm) was defined on the

Ni layer by EBL and thermal evaporation. (3) Arrays of U-shaped 80 nm diameter silicon nanowires were patterned as described above such that the straight arms and U-tips were on top of the gold mesh and open areas, respectively. (4) PMMA under the straight arms of U-shaped nanowires was cross-linked by EBL using a dose of $\sim 8,000 \mu\text{C}/\text{cm}^2$. (5) A second gold mesh (100 nm thick) which was coincident in the x-y plane with the bottom mesh was defined on top of the cross-linked PMMA and deposited via thermal evaporation. (6) The Ni sacrificial layer was etched in nickel etchant (TFB, Transene Company, Inc., Danvers, MA) for 1 h and then the free-standing arrays of U-shaped silicon nanowires embedded in the Au-mesh/PMMA/Au-mesh trilayer were transferred to a copper TEM grid (300 mesh Cu, Ted Pella, Redding, CA). TEM characterization (JEOL 2100, JEOL Ltd., Tokyo, Japan or aberration-corrected Zeiss Libra MC TEM, Carl Zeiss AG, Oberkochen, Germany) was carried out at a beam accelerating voltage of 200 kV. Fourier-filtered images processed from the high-resolution TEM (HRTEM) images were used to characterize dislocations in the bent nanowires.

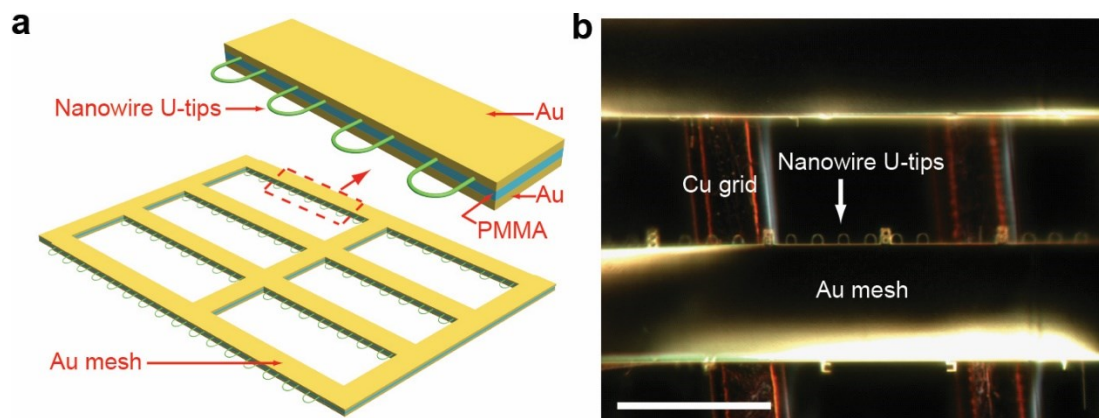


Figure 4-1. Preparation of TEM samples. **a**, Schematics of free-standing arrays of U-shaped silicon nanowires embedded in the Au mesh layers. **b**, Dark-field optical image of U-shaped silicon nanowire arrays fixed and encapsulated in mesh-like double-layered gold ribbon networks transferred to a copper TEM grid. Scale bar, 50 μm .

4.2.4 Strain release tests

Arrays of suspended U-shaped silicon nanowires were transferred to TEM grids as described above and introduced into a focused ion beam (FIB) instrument (dual ion/electron beam Zeiss NVision 40, Carl Zeiss AG, Oberkochen, Germany). The FIB was used to cut one of the two suspended arms of a U-shaped nanowire (Ga^+ ions, 30 kV) while monitoring the nanowire release process *in situ* by SEM video-rate imaging (8 frames per second).

4.2.5 Raman microscopy characterization

Arrays of suspended U-shaped silicon nanowires with some nanowires cut by FIB were transferred to a glass slide. Raman spectra were acquired with a LabRam Evolution Multiline Raman Spectrometer (Horiba, Kyoto, Japan) equipped with 1800 blaze/mm grating, Synapse CCD detector, and $100\times$ 0.95 NA objective using a 633 nm CW diode laser which was depolarized using a zero-order quarter waveplate optimized for 633 nm. The laser power was ~ 26 μW and the laser spot was ~ 1.5 μm in diameter.

4.2.6 Finite element simulation of nanowire bending

A geometrically nonlinear finite element model was used to simulate the large deformations of nanowires under load. The modelling and simulations were carried out with commercial ANSYS 14.5 software. In our model, the nanowire is considered as a linearly elastic cantilever beam with elastic modulus of 188 GPa and Poisson ratio of 0.3 characteristic of silicon²⁶. The length and diameter of the cantilever beam are 20 μm and 80 nm, respectively. The in-plane shear forces generated during the experimental assembly process are expected to produce an approximately uniform distributed bending load, which are applied in the simulations; these uniform bending loads ranged from 0 to 20 nN/ μm .

The deformation of the nanowire under different loading and the corresponding load-dependent radii of curvature at the fixed end were calculated from the simulated results.

4.2.7 Bend-up nanowire probe arrays

Arrays of head-to-head U-shaped silicon nanowires were used as building blocks to fabricate arrays of 3D bend-up nanoprobe devices. Briefly, (1) a nickel sacrificial layer (100 nm) was defined and deposited on a silicon substrate (600 nm thermal SiO₂) by EBL and thermal evaporation. (2) U-shaped 80 nm diameter silicon nanowires were deterministically assembled in PMMA trenches for direction 1. (3) A PMMA bottom passivation layer for the nanowire arrays assembled in Step (2) was fabricated by EBL with an area dose of $\sim 8,000 \mu\text{C}/\text{cm}^2$ followed by removal of unexposed PMMA in acetone. (4) The second array of U-shaped 80 nm diameter silicon nanowires was then assembled in a similar manner with a head-to-head orientation relative to the U-shaped nanowires of Step (2). (5) A PMMA bottom passivation layer for the nanowires assembled in Step (4) was defined as in Step (3). (6) S/D metal contacts Cr/Pd/Cr (1.5/75/50 nm) were defined by EBL and thermal evaporation. Typically, the S/D contact separation was 1.5 μm in each probe, and the free end of the nanowire extended 3–6 μm from the source contact. (7) A top SU8 (SU8 2000.5, Microchem, Westborough, MA) layer was subsequently defined by EBL to complete the passivation of the metal contacts/interconnects. (8) The nickel layer was etched (~ 1 h, TFB etchant, Transene Company, Inc., Danvers, MA) to yield the 3D bend-up probes. Notably, individual nanowire probe devices were fabricated without registration to nanowires, since the patterns of bottom PMMA passivation layer, contact electrodes and top SU8 passivation layer, and x- and y- coordinates of U-shaped nanowires

all precisely match the original predetermined trench pattern used for shape-selective deterministic assembly; the process follows a design-oriented fabrication.

Device sensitivities were characterized by water-gate measurements which were carried out in $1\times$ PBS with a Ag/AgCl wire reference electrode^{27,28}. The nanowire device conductances were measured with a DC bias of 0.1 V, and the current was converted to voltage with a current preamplifier (10^{-6} A/V, Model 1211, DL Instruments, Brooktondale, NY), low-pass filtered (0-6 kHz, CyberAmp 380, Molecular Devices, Sunnyvale, CA), and digitized at 20 kHz sampling rate (Axon Digi1440A, Molecular Devices).

4.2.8 Nanowire waveguides

Assembled U-shaped CdS nanowires (diameters \sim 150 nm) were used for optical waveguide experiments. The radius of curvature of the U-shaped tips were 2 μ m. A 405 nm diode laser (LRD-0405, LaserGlow Technologies, Toronto, Ontario) was used to excite the nanowires: power \sim 40 μ W; spot size \sim 1 μ m diameter. Wide-field photoluminescence images were collected by placing a 450 nm dichroic mirror and a 420 nm longpass filter between the sample and a camera.

4.2.9 Finite-Difference Time-Domain calculations

Finite-difference time-domain (FDTD) analyses were performed using a dipole light source with wavelength 515 nm coupled at one end of the nanowire. In the calculations, the nanowire and substrate parameters are consistent with experimental values (e.g. nanowire diameter 150 nm, substrate SiO₂ thickness 300 nm). Calculation showed that only the fundamental mode was excited in the nanowires. The electric field intensity in the nanowires was calculated using perfectly matched layer boundary

conditions. For tangentially coupled U-shaped nanowire and straight nanowire, transmission efficiency and optical loss were calculated.

4.3 Results and discussion

4.3.1 Demonstration of shape-controlled nanowire assembly

Our assembly concept features trenches with designed shapes to anchor nanowires and guide nanowire bending and alignment, so that nanowires conform to the geometries of the trenches. To demonstrate our concept, we start with U-shaped nanowire assembly. The assembly procedure consists of (i) fabrication of U-shaped trench arrays on a target substrate and (ii) sliding a nanowire growth substrate over the target substrate through an “anchor-bend-align” process (**Fig. 4-2a**).

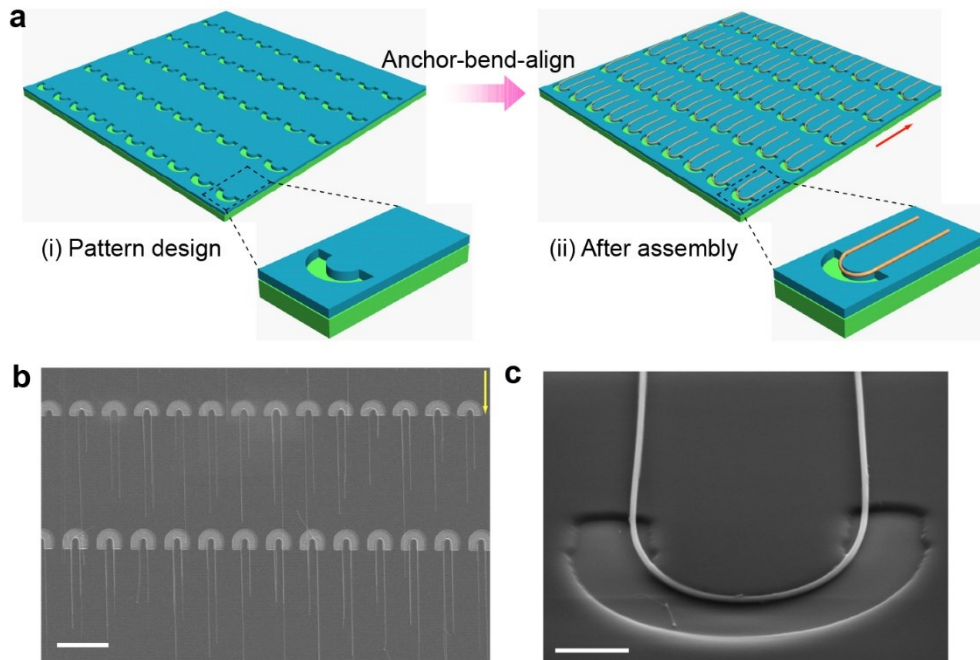


Figure 4-2. Demonstration of shape-controlled nanowire assembly. **a**, Schematics of deterministic assembly of U-shaped nanowire arrays. The arrow shows the sliding direction of the nanowire growth substrate with respect to the target substrate. **b**, Top view SEM images of U-shaped silicon nanowire arrays assembled by PMMA trenches. Nanowire diameter is 80 nm. The arrow shows the sliding direction of the nanowire growth substrate with respect to the target substrate. Scale bars, 20 μm . **c**, Representative

(Continued) tilt view SEM image of U-shaped silicon nanowire anchored, bent and aligned in a PMMA trench. Nanowire diameter is 80 nm. Scale bar, 1 μm .

To demonstrate U-shaped nanowire deterministic assembly, we fabricated U-shaped PMMA trench arrays to assemble silicon nanowires. Briefly, the target substrate was patterned with PMMA U-shaped trenches by EBL and then mounted onto a micromanipulator-controlled linear actuator stage, and coated with mineral oil as lubricant. Then, the growth substrate with straight silicon nanowires (nanowire length 40–80 μm , diameter 80 nm) was placed on the target substrate with controlled pressure ($\sim 4.8 \text{ Ncm}^{-2}$) and translated at a constant velocity of $\sim 5 \text{ mm/min}$ with respect to the fixed growth substrate. SEM images of the assembled nanowire arrays (**Fig. 4-2b,c**) reveal several key features. First, nanowires are precisely anchored at the U-shaped trenches. The average offsets of y - and x - coordinates of nanowires (U-shaped segments) are within $\pm 20 \text{ nm}$ and $\pm 40 \text{ nm}$ (the y -direction is sliding direction; x -direction is in the substrate plane and is perpendicular to the y -direction). We note that the length of nanowire end segments could be controlled by subsequent lithography-based trimming⁶. Second, nanowires are precisely bent and aligned along the inner edge of the trenches. The average deviation of nanowire radius of curvature is within $\pm 40 \text{ nm}$ and the end segments of nanowires are aligned within $\pm 1^\circ$. Third, the U-shaped tips of $\sim 50\%$ of the nanowires were flush with the PMMA surface but not attached to the exposed substrate in the U-trench, suggesting that anchoring and alignment of nanowires result from mechanical ‘snagging’ on the inner wall of the trenches rather than from the forces between the nanowires and the exposed SiO_2 region^{2,6,8}. Fourth, the overall assembly yield is $\sim 90\%$ (statistics from an area of $1 \times 1 \text{ mm}$ with 1,320 sites). Specifically, $\sim 60\%$ of the trenches contain a single nanowire, $\sim 20\%$ two nanowires, $\sim 10\%$

three nanowires, and ~10% are vacant (**Fig. 4-3a**). Overall, these results indicate that both positions and shapes of nanowire arrays are deterministic in high yield. We note that nanowires precisely overlap with the inner edge of the trenches, and feature sizes such as trench width do not affect the precision of nanowire assembly, in contrast to previously reported nanowire assembly techniques which rely on small feature size for deterministic assembly at the expense of limited assembly area, as well as time of fabrication and assembly yield⁶. This advantage suggests the potential of using lower-resolution lithography, for example, PL versus EBL, to fabricate patterns with large feature size for large-scale, high-precision deterministic nanowire assembly.

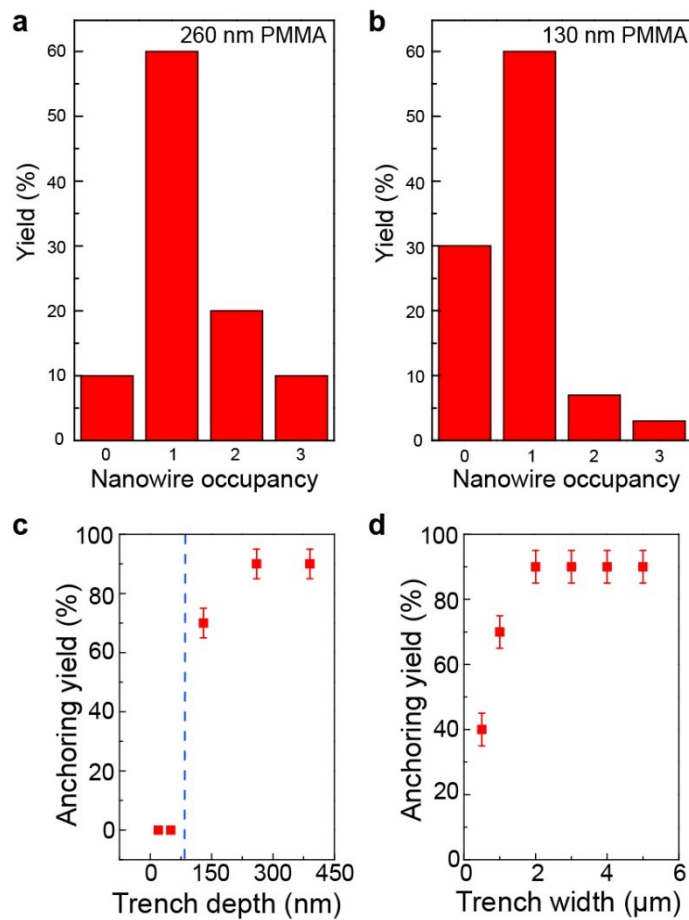


Figure 4-3. Occupancy statistics of U-shaped nanowire arrays assembled by PMMA trenches. a, Nanowire occupancy statistics with PMMA trench depth 260 nm and trench

(Continued) width 3 μm . **b**, Nanowire occupancy statistics with PMMA trench depth 130 nm and trench width 3 μm . **c-d**, Nanowire anchoring yield versus trench depth (**c**) and width (**d**). In **c**, trench width is fixed at 3 μm ; in **d**, trench depth is fixed at 260 nm. The blue vertical dashed line in the left plot indicating the nanowire diameter of 80 nm shows that assembly yield is zero for trench depth less than nanowire diameter. Statistics in **a-d** are based on an area of 1×1 mm, 1,320 sites. Silicon nanowires used in **a-d** have diameter 80 nm.

We assembled nanowires in trenches of various sizes to determine key assembly parameters controlling nanowire assembly yield (**Fig. 4-3**). First, we observed that when trench depth is less than the nanowire diameter, the anchoring yield is zero. When trench depth is larger than nanowire diameter, the anchoring yield increases with trench depth and saturates at $\sim 90\%$ if trench depth is more than ~ 3 times of nanowire diameter. Second, anchoring yield increases with trench width, and saturates at $\sim 90\%$ if trench width is more than 2 μm (for 80 nm diameter nanowires). Third, reducing trench depth can reduce the percentage of trenches in which multiple nanowires are anchored. Taken together, these results demonstrate the rational control of assembly yield and that nanowire occupancy can be achieved by tuning trench size. Moreover, these results corroborate the hypothesis that mechanical ‘snagging’ rather than surface adhesion is responsible for nanowire assembly in the U-trenches. Thus, we term our process “anchor-bend-align” in that nanowires from the growth substrate are first anchored by ‘snagging’ on the exposed edge of the patterned trench, and then shear forces due to the linear transfer^{2,6,8} bend the nanowires around the trench features and align their arms on the resist.

4.3.2 Characterization of assembled nanowires

We conducted several experiments to characterize the U-shaped, deterministically assembled nanowires and understand the mechanism of assembly. First, we designed U-

shaped PMMA trenches with different radii of curvature ($R = 1\text{--}3\ \mu\text{m}$) to assemble silicon nanowires. SEM images of assembled nanowires show that the radii of curvature of the nanowires are in agreement with the radii of curvature of the trenches, with average deviation $\pm 40\ \text{nm}$ (**Fig. 4-4a,b**). Second, we carried out strain release tests, Raman microscopy, and TEM characterization of U-shaped nanowires. The results show several key features. (1) U-shaped nanowires spring back into approximately straight nanowires after being released by FIB cutting (**Fig. 4-4c**). (2) Local defects develop in bent nanowires with reduced radius of curvature (i.e. increased strain) (**Fig. 4-4d-f**). (3) The FWHM of the first-order Raman scattering mode from U-shaped silicon nanowires increases with reduced radius of curvature (**Fig. 4-4g,h**). The broadening of Raman peak is due to the inhomogeneous strain distribution²⁹ which includes the compressive strain causing a positive frequency shift on the inner side of the bent nanowires and the tensile strain causing a negative shift on the outer side of the bent nanowires.

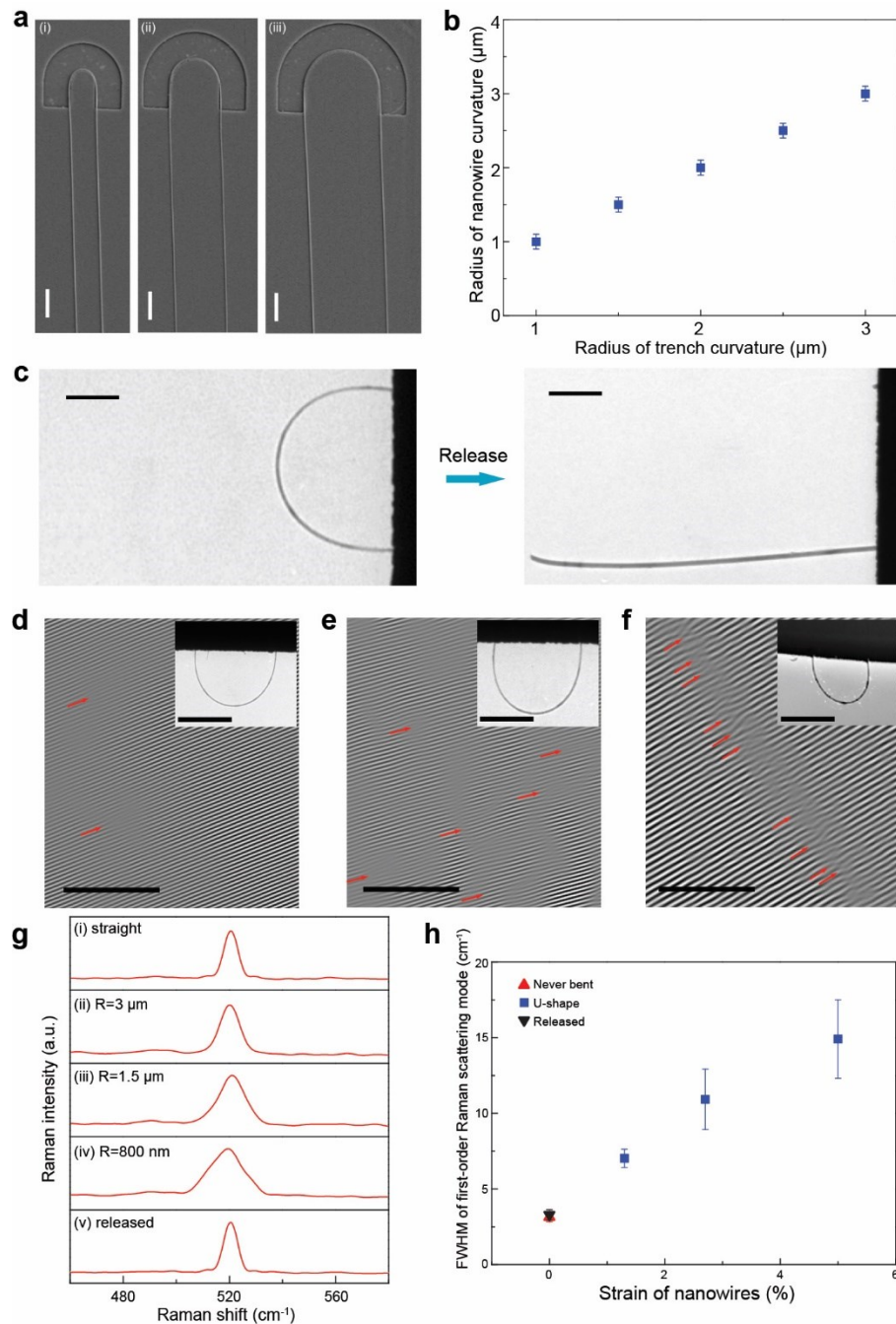


Figure 4-4. Characterization of assembled nanowires. **a**, Representative SEM images of U-shaped silicon nanowires assembled by PMMA trenches with controlled radius (R) of curvature. (i) $R = 1 \mu\text{m}$; (ii) $R = 2 \mu\text{m}$; (iii) $R = 3 \mu\text{m}$. Nanowire diameter is 80 nm. Scale bars, 2 μm . **b**, Plot of radius of nanowire curvature versus radius of PMMA pattern curvature. Nanowire diameter is 80 nm. **c**, Representative TEM images of U-shaped silicon nanowire ($R = 1.5 \mu\text{m}$) before (left) and after (right) cutting nanowire to release strain. Scale bars, 1 μm . **d-f**, Fourier-filtered HRTEM images of U-shaped tip of the assembled U-shaped nanowires (nanowire diameter 80 nm) with radii of curvature of 3.0, 1.5, and 0.8 μm in **d**, **e** and **f**, respectively. Red arrows indicate the dislocation regions.

(Continued) Scale bars, 5 nm. Insets: low magnification TEM images of the U-shaped, suspended nanowires. Scale bars are 4 μm , 2 μm and 2 μm in the inset images in **d**, **e** and **f**, respectively. **g**, Normalized Raman spectra acquired on silicon nanowires with different strains. **(i)** Raman spectra acquired from a straight nanowire which was never bent. **(ii-iv)** Raman spectra acquired at the U-shaped tip of nanowires with radii of curvature of 3.0, 1.5, and 0.8 μm , respectively. **(v)** Raman spectra acquired from a FIB-released nanowire at the position which used to be the tip of the U-shape with radius of curvature 1.5 μm . **h**, Plot of FWHM of first-order Raman scattering mode versus strain of U-shaped silicon nanowires. The strain was approximately calculated from nanowire radii of curvature and nanowire diameter.

Third, we designed trenches with very small radius of curvature ($R = \sim 200 \text{ nm}$) and applied different contact pressures to study the dependence of nanowire curvature on load (contact pressures). The results show that average radii of nanowire curvature (80 nm diameter silicon nanowires) are 1500, 800 and 550 nm when pressures are 0.8, 4.8 and 7.2 Ncm^{-2} (**Fig. 4-5a,b**). Mechanical calculations show that the radius of nanowire curvature is proportional to the inverse square root of load on the nanowires, which fits well with our experimental data (**Fig. 4-5c,d**). Fourth, we have also studied the dependence of minimum radius of nanowire curvature on diameter while keeping contact pressure and other assembly conditions fixed. The results show that the approximate minimum radii of nanowire curvature are 100, 400 and 800 nm for nanowires with diameters of 10, 30 and 80 nm (**Fig. 4-5e**). Mechanical calculations show that radius of nanowire curvature decreases linearly with diameter when nanowire diameter is larger than 30 nm, and decrease more quickly when nanowire diameter is smaller than 30 nm, which is in agreement with our experimental data (**Fig. 4-5e**).

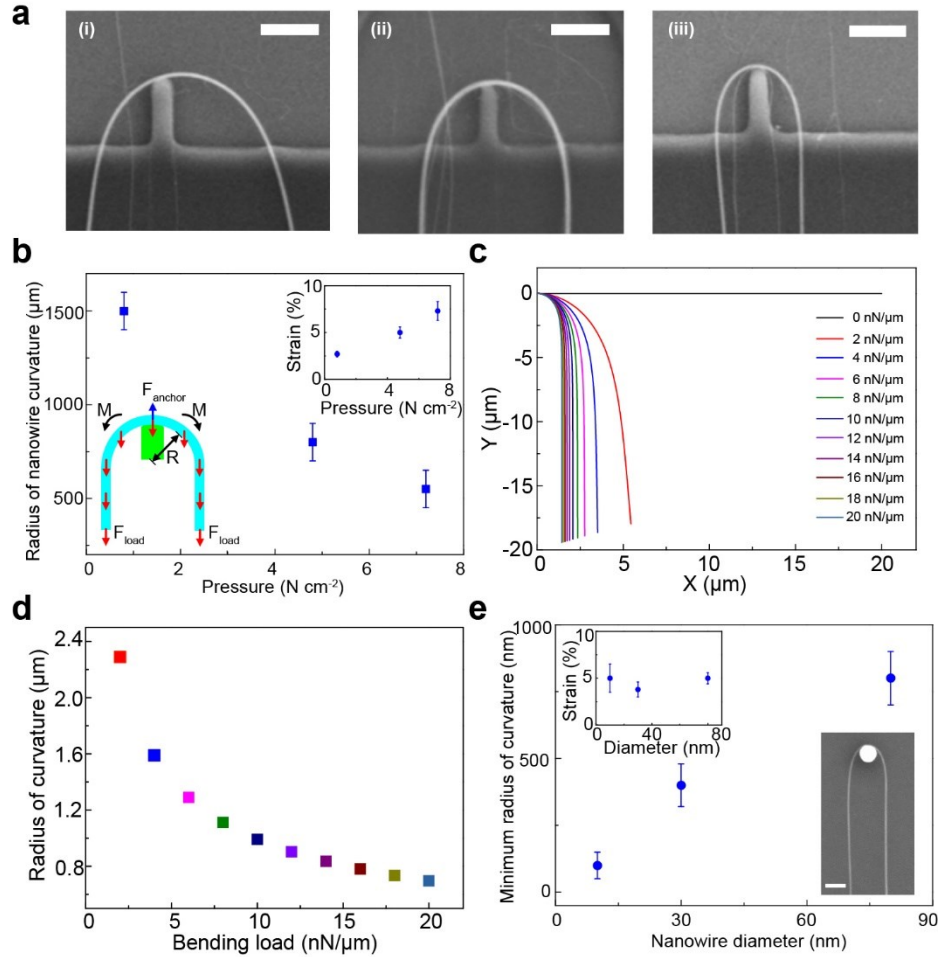


Figure 4-5. Control of assembled nanowire radius of curvature. **a**, Representative SEM images of silicon nanowires assembled with (i) pressure = 0.8 N cm^{-2} , (ii) pressure = 4.8 N cm^{-2} , (iii) pressure = 7.2 N cm^{-2} . Nanowire length is 40–60 μm . Scale bars, 1 μm . **b**, Plot of radius of silicon nanowire curvature versus contact pressure. Left inset: Model and force analysis of nanowire bending during assembly. Right inset: Plot of strain of silicon nanowires versus contact pressure. Nanowire diameter is 80 nm. **c**, Simulation of deformation of the nanowire under bending loads 0 to 20 nN/ μm . **d**, The corresponding radius of curvature at the fixed end calculated from the simulated results in **c**. **e**, Plot of minimum radius of curvature versus nanowire diameter under standard assembly conditions (pressure = 4.8 N cm^{-2}). Left inset: Plot of strain of silicon nanowires versus nanowire diameter. Right inset: Representative SEM image of U-shaped silicon nanowire assembled by gold nanoparticle. Nanowire diameter is $\sim 10 \text{ nm}$. Scale bar, 200 nm.

4.3.3 Generalization of assembly method

To demonstrate the generality of shape control beyond U-shaped trenches, we designed rectangular and triangular trenches to assemble and bend nanowires into rectangular and triangular patterns by one-step alignment in one direction (**Fig. 4-6a**, i, ii). Moreover, we designed trenches with multi-directional channels to bend and align nanowires by adding a second alignment step perpendicular to the first alignment step's direction of motion (**Fig. 4-6a**, iii). Optical and SEM images of nanowires assembled by rectangular and triangular shaped trenches show several key features (**Fig. 4-6b,c**). First, rectangular and triangular trenches can successfully guide the bending of nanowires by one-step alignment, and nanowires precisely overlap with the inner edge of the trenches. Second, at the corner of the square trench, the nanowire radius of curvature reaches the minimum limit (~400 nm for 30 nm diameter nanowires) when the radius of trench curvature (~200 nm) is smaller than the limit. Third, at the vertex of triangle shapes, radii of curvature of nanowires and trenches are the same (~700 nm) when radius of trench curvature is larger than the limit. Fourth, the shape of the outer edge on the opposite side (versus inner edge) of the trenches did not affect the shape of nanowires. Furthermore, optical and SEM images of nanowires assembled by trenches with multi-directional channels show that bending directions and positions of different segments of individual nanowires were determined independently during each translation step (**Fig. 4-6d**). The assembly yield is 30-40% for rectangular shaped nanowires, 40-50% for triangular shaped nanowires, and 40-50% for two-step aligned nanowires (statistics calculated in an area of 1×1 mm, 1,320 sites). Overall, these results demonstrate that trenches can serve as a guide to bend nanowires into different basic geometric shapes (circular, rectangular and triangular) by one-step alignment, and more complex structures by multi-step alignments.

We note that it is possible to combine basic geometric shapes and multi-step alignments to assemble more advanced and functional nanowire structures such as electronic and photonic circuit elements^{16,30,31} with additional efforts in the future.

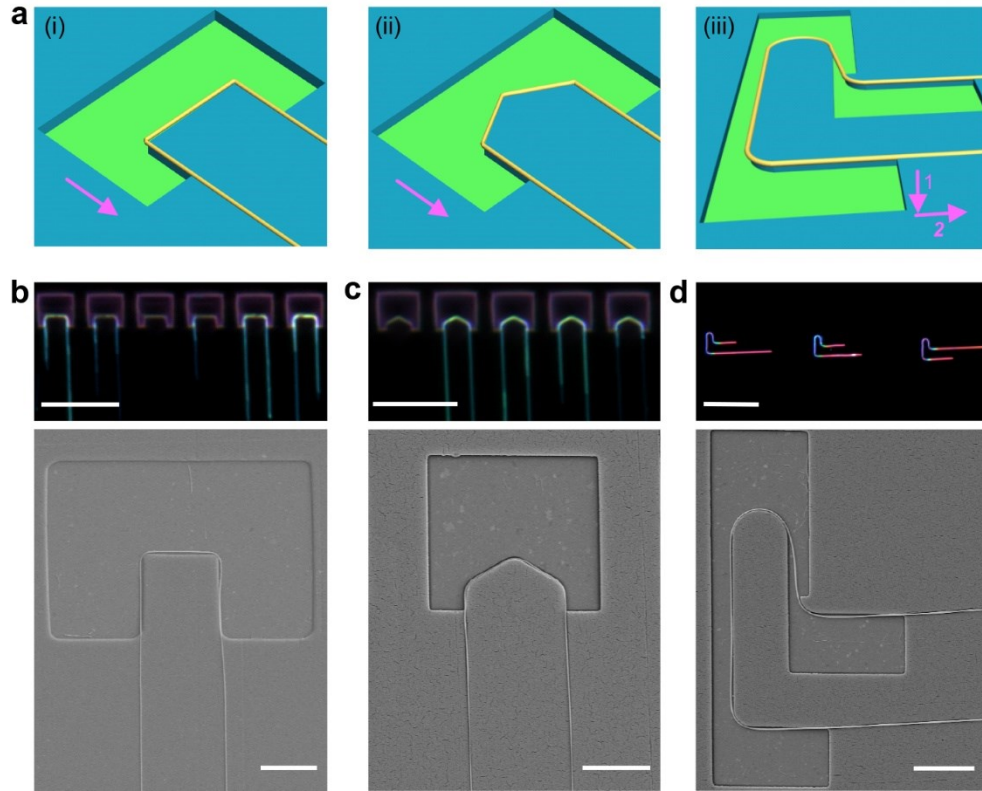


Figure 4-6. Generality of shape-controlled nanowire assembly. **a**, Schematics of deterministic assembly of nanowires with various shapes: rectangular shape (i) and triangular shape (ii) by one-step alignment, and more complex shape (iii) by multi-directional alignments. The arrows show the sliding directions of nanowire growth substrates with respect to the target substrates. **b-d**, Optical (upper) and SEM (lower) images of deterministic assembly of nanowires with various shapes: rectangular shape in **b** and triangular shape in **c** by one-step alignment, and more complex shape in **d** by multi-directional alignments. Nanowire diameters are 30 nm in **b** and **c**, and 80 nm in **d**. Trench depths are 130 nm in **b** and **c**, and 200 nm in **d**. Scale bars of optical images in **b-d** are 10 μm , 10 μm , and 30 μm , respectively. Scale bars of SEM images in **b-d** are 2 μm , 2 μm , and 3 μm , respectively.

4.3.4 Wafer-scale assembly

We also extended our concept from EBL to PL to demonstrate wafer-scale shape-controlled deterministic nanowire assembly. Briefly, a 3-inch wafer was patterned with U-shaped photoresist trench arrays (S1805, Microposit) with 432,990 sites serving as the target substrate (**Fig. 4-7a**). LOR (1A, Microposit) was used as an undercut layer for better anchoring of nanowires. The trench width ($\sim 3 \mu\text{m}$) and nanowire printing process were the same to that of EBL. Optical and SEM images of nanowire arrays show several important features (**Fig. 4-7a-c**). First, U-shaped nanowires were uniformly assembled on the patterned regions of the whole wafer with pitch of adjacent nanowires of $15 \mu\text{m}$ and row-to-row pitch of $100 \mu\text{m}$. The overall assembly yield is $\sim 90\%$ (statistics calculated in an area of $1.5 \times 1.5 \text{ mm}$, 1,500 sites). Specifically, there are $\sim 50\%$ trenches with a single nanowire, $\sim 30\%$ with two nanowires, $\sim 10\%$ with three nanowires, and $\sim 10\%$ are vacant (**Fig. 4-7d**). Second, U-shaped nanowires precisely overlap with the inner edge of trenches. The average offsets of y - and x - coordinates of nanowires are within $\pm 30 \text{ nm}$ and $\pm 50 \text{ nm}$. The average deviation of radius of nanowire curvature is within $\pm 50 \text{ nm}$, and end segments of nanowires are highly-aligned within $\pm 1^\circ$. These results demonstrate the high-precision shape-controlled deterministic nanowire assembly by PL on a wafer-scale.

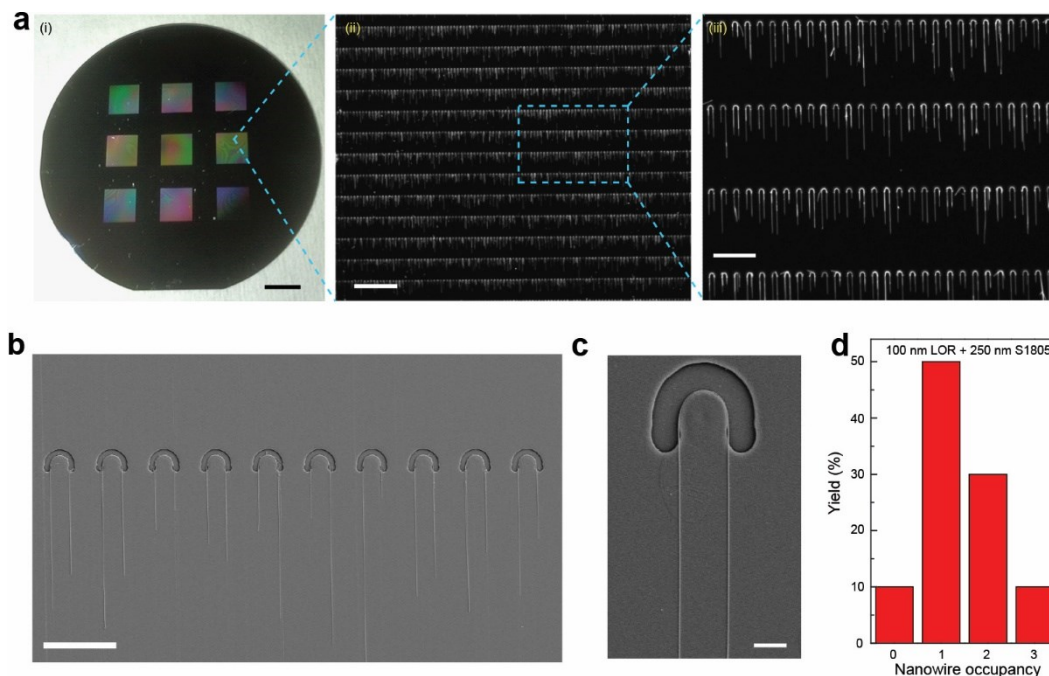


Figure 4-7. Wafer-scale assembly. **a**, Wafer-scale assembly of U-shaped nanowire arrays. (i) Photograph of 3-inch silicon wafer with U-shaped trench arrays defined by PL. The photoresist layer consists of 100 nm LOR 1A bottom layer and 250 nm S1805 top layer. Scale bar, 10 mm. (ii, iii) Optical images of U-shaped silicon nanowire arrays assembled on the 3 inch wafer. Scale bars in (ii) and (iii) are 200 μm and 50 μm respectively. **b**, Representative SEM image of U-shaped silicon nanowires assembled in photoresist trenches. Scale bar, 20 μm . **c**, Representative SEM image of an individual U-shaped silicon nanowire assembled in a photoresist trench. Scale bar, 2 μm . **d**, Occupancy statistics of nanowires assembled by photoresist trenches.

4.3.5 Applications of assembly technique

To demonstrate the potential applications of our shape-controlled nanowire assembly, we used U-shaped silicon nanowires as building blocks to fabricate 3D bend-up nanowire probe arrays (**Fig. 4-8a**). A two-step assembly was used to construct U-shaped nanowire arrays in head-to-head directions. We note that this design can reduce row-to-row separation of devices. Then, 3D bend-up nanowire probe arrays were fabricated using stressed metal interconnects (Cr/Pd/Cr) that bend the probe arrays upward³². Notably,

individual nanowire probe devices were fabricated without registration to nanowires, because the x - and y - coordinates of the underlying PMMA passivation layer, the contact electrodes, the top SU8 passivation layer, and the U-shaped nanowires all precisely matched the original predetermined trench pattern. SEM images of bend-up probe arrays shows (**Fig. 4-8b**) that we have successfully assembled U-shaped nanowire arrays in head-to-head directions and fabricated bend-up probe arrays with a yield of $\sim 90\%$. The pitch of nanowire probe devices is $\sim 20 \mu\text{m}$. A histogram of water-gate sensitivities of bend-up nanowire probe array shows that the devices have water-gate sensitivities of 1-4 $\mu\text{S/V}$ (**Fig. 4-8c**), which are comparable (considering that channel length of our devices is 10-15 μm) to the performance of silicon nanowire devices that we previously reported³². This work thus demonstrates the potential for next generation 3D flexible nanoelectronic devices for large-scale multiplexed measurements of chemical and biological signals³².

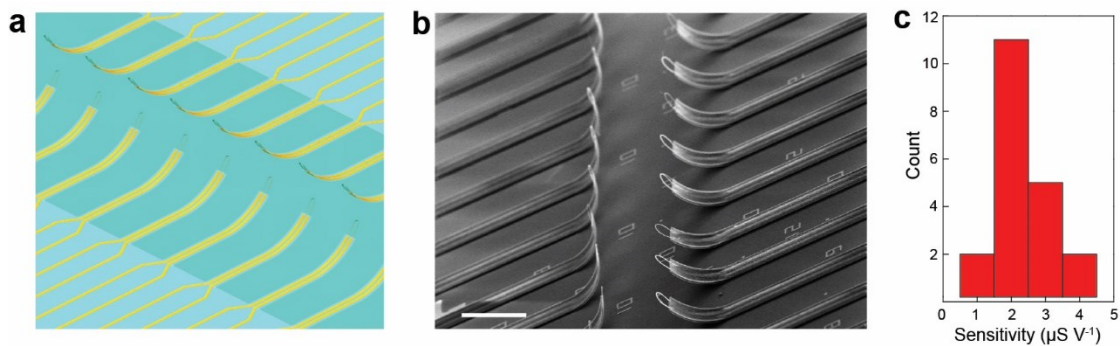


Figure 4-8. 3D probe arrays. **a**, Schematic of 3D bend-up probe arrays with multi-direction assembled U-shaped silicon nanowires. **b**, Representative SEM image of the 3D bend-up probe arrays. Scale bar, 20 μm . **c**, Histogram of water-gate sensitivity of U-shaped p-type silicon nanowire FET bend-up probe arrays.

We also demonstrated the guiding and manipulating of light through U-shaped CdS nanowire waveguides as integrated nanoscale photonic circuit elements³⁰ (**Fig. 4-9**). The 150 nm diameter CdS nanowires were bent around PMMA U-features with 2 μm radius of

curvature. Excitation with a 405 nm laser at one end of the nanowire is shown to propagate along the straight arm, make a U-turn, and finally propagate in the reverse direction to the other end of nanowire (**Fig. 4-9a**), allowing effective use of this nanowire waveguide as, for instance, a microscale delay line for on-chip photonics³¹. The result is consistent with our FDTD simulation with the same configuration (**Fig. 4-9a**). Moreover, we did FDTD simulation of coupling between tangentially assembled U-shaped nanowire and straight nanowire, which showed that with a nanoscale gap, a nanoresonator structure can be fabricated (**Fig. 4-9b**). We used two-step assembly to anchor a straight CdS nanowire and a U-shaped CdS nanowire sequentially with a 70 nm gap (**Fig. 4-9c**). Excitation with a 405 nm laser at one end of the U-shaped nanowire and at one end of the straight nanowire both showed results consistent with simulation, which demonstrated efficient coupling between two nanowires and directional waveguide after coupling (**Fig. 4-9d**). These results demonstrated the unique capability of shape-controlled assembly technique to fabricate novel nanoscale photonic circuit elements.

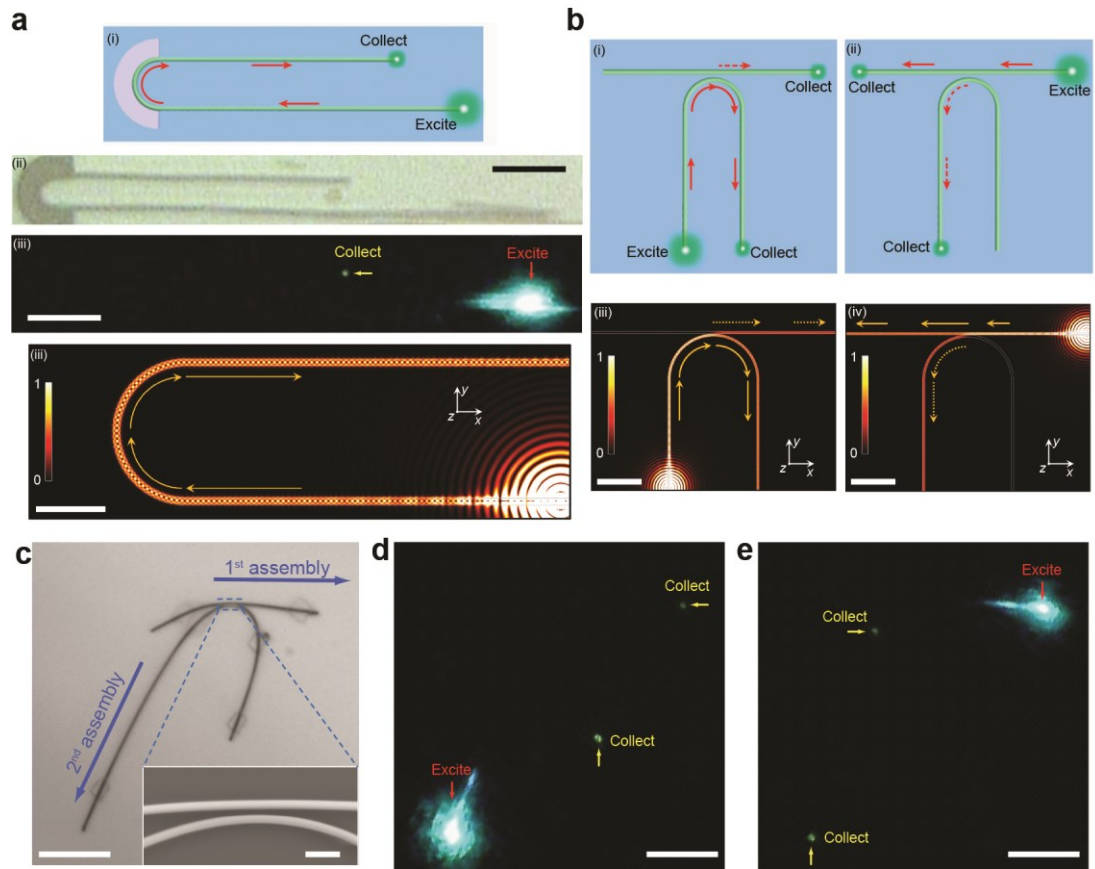


Figure 4-9. Nanowire optical waveguide. **a**, Single U-shaped CdS nanowire optical waveguide. (i), schematic of a nanowire optically pumped at one end of an arm. The red arrows indicate the guiding directions of light in the nanowire. (ii), white light optical image of a single U-shaped CdS nanowire waveguide. Scale bar, 8 μm . (iii), photoluminescence image of a single U-shaped CdS nanowire waveguide. Scale bar, 8 μm . (iv), FDTD simulation of a single U-shaped CdS nanowire waveguide. Scale bar, 2 μm . **b**, (i, ii), Schematics of optical coupling between tangentially assembled U-shaped CdS nanowire and straight CdS nanowire. In (i), one end of the U-shaped nanowire was optically pumped; in (ii), one end of the straight nanowire was optically pumped. The red arrows indicate the guiding directions of light in the nanowire. (iii, iv), FDTD simulations corresponding to (i) and (ii), respectively. Scale bars, 2 μm . **c**, White light optical image of tangentially assembled U-shaped CdS nanowire and straight CdS nanowire. Scale bar, 5 μm . Inset: zoom of gap region. Scale bar, 500 nm. **d**, Photoluminescence image of situation in **b** (i). Scale bar, 5 μm . **e**, Photoluminescence image of situation in **b** (ii). Scale bar, 5 μm .

4.4 Conclusion and outlook

We have demonstrated a general shape-controlled nanowire assembly method with high yield. We showed that the shape of the assembled nanowires can be controlled precisely by factors such as trench geometry and applied force at a wafer-scale. This technique opened up unique opportunities in nanoelectronics and nanophotonics beyond the scope of straight nanowires. For example, arrays of 3D bend-up U-shaped nanowire probes can be used for multiplexed intracellular measurement. In addition, the ability to manipulate light on sub-wavelength scales in 2D using deterministically assembled shaped-controlled nanowires represents a promising pathway towards future nanowire photonic circuits integrated with nanoelectronic circuits and nanosensor elements on one chip³⁰. Moreover, the inhomogeneous strain in bent nanowires could break the symmetry of silicon and produce significant second-order nonlinear optical susceptibility, $\chi^{(2)}$, which makes it promising to fabricate silicon nanowire electro-optic modulator²⁰ and silicon nanowire waveguides with second-harmonic generation¹⁷ for future optical computer systems. Compared to straight nanowire devices, the assembled curvature-controlled buckled nanowires could accommodate much more strain in different directions, which have the potential to serve as key elements for future generation stretchable electronic and photonic circuits with band-gap engineering capabilities. We are currently exploring properties and applications of strained nanowires assembled with this technique.

4.5 Bibliography

1. Wang, M. C. P. & Gates, B. D. *Mater. Today* **12**, 34 (2009).
2. Yan, H. *et al. Nature* **470**, 240 (2011).
3. Heurlin, M. *et al. Nature* **492**, 90 (2012).

4. Freer, E. M., Grachev, O., Duan, X., Martin, S. & Stumbo, D. P. *Nature Nanotech.* **5**, 525 (2010).
5. Li, M. *et al.* *Nature Nanotech.* **3**, 88 (2008).
6. Yao, J., Yan, H. & Lieber, C. M. *Nature Nanotech.* **8**, 329 (2013).
7. Collet, M. *et al.* *Adv. Mater.* **27**, 1268 (2015).
8. Fan, Z. *et al.* *Nano Lett.* **8**, 20 (2008).
9. Tao, A. R, Huang, J. & Yang, P. *Acc. Chem. Res.* **41**, 1662 (2008).
10. Pauzauskie, P. J. *et al.* *Nature Mater.* **5**, 97 (2006).
11. Tsvivion, D., Schvartzman, M., Popovitz-Biro, R., von Huth, P. & Joselevich, E. *Science* **333**, 1003 (2011).
12. Duan, X. *et al.* *Nature* **425**, 274 (2003).
13. Cao, J. *et al.* *Nature Nanotech.* **4**, 732 (2009).
14. Wang, Z. L. & Song, J. *Science* **312**, 242 (2006).
15. He, R. & Yang, P. *Nature Nanotech.* **1**, 42 (2006).
16. Law, M. *et al.* *Science* **305**, 1269 (2004).
17. Cazzanelli, M. *et al.* *Nature Mater.* **11**, 148 (2012).
18. Sun, L., Kim, D. H., Oh, K. H. & Agarwal, R. *Nano Lett.* **13**, 3836 (2013).
19. Suess, M. J. *et al.* *Nature Photon.* **7**, 466 (2013).
20. Jacobsen, R. S. *et al.* *Nature* **441**, 199 (2006).
21. Wu, W., Wen, X. & Wang, Z. L. *Science* **340**, 952 (2013).
22. Pan, C. *et al.* *Nature Photon.* **7**, 752 (2013).
23. Haeni, J. H. *et al.* *Nature* **430**, 758 (2004).
24. Hicks, C. W. *et al.* *Science* **344**, 283 (2014).
25. Falvo, M. R. *et al.* *Nature* **389**, 582 (1997).
26. Stan, G., Krylyuk, S., Davydov, A. V. & Cook, R. F. *J. Mater. Res.* **27**, 562 (2012).
27. Tian, B. *et al.* *Science* **329**, 830 (2010).

28. Qing, Q. *et al.* *Nature Nanotech.* **9**, 142 (2014).
29. Chen, J. *et al.* *Nano Lett.* **10**, 1280 (2010).
30. Barrelet, C. J., Greytak, A. B. & Lieber, C. M. *Nano Lett.* **4**, 1981 (2004).
31. Xia, F., Sekaric, L. & Vlasov, Y. *Nature Photon.* **1**, 65 (2007).
32. Yang, P., Yan, R. & Fardy, M. *Nano Lett.* **10**, 1529 (2010).

Chapter 5. Free-standing kinked nanowire transistor probes for targeted intracellular recording in three dimensions

5.1 Introduction

Recording intracellular bioelectrical signals is central to understanding the fundamental behavior of cells and cell networks in, for example, neural and cardiac systems¹⁻⁴. The standard tool for intracellular recording, the patch-clamp micropipette⁵ is widely applied, yet remains limited in terms of reducing the tip size, the ability to reuse the pipette⁵ and ion exchange with the cytoplasm⁶. Recent efforts have been directed towards developing new chip-based tools^{1-4,7-13}, including micro-to-nanoscale metal pillars⁷⁻⁹, transistor-based kinked nanowire^{10,11} and nanotube devices^{12,13}. These nanoscale tools are interesting with respect to chip-based multiplexing, but, so far, preclude targeted recording from specific cell regions and/or subcellular structures. In this chapter, we overcome this limitation in a general manner by fabricating free-standing probes in which a kinked silicon nanowire with an encoded FET detector serves as the tip end. These probes can be manipulated in 3D within a standard microscope to target specific cells or cell regions, and record stable full-amplitude intracellular action potentials from different targeted cells without the need to clean or change the tip. Simultaneous measurements from the same cell made with free-standing nanowire and patch-clamp probes show that the same action potential amplitude and temporal properties are recorded without corrections to the raw nanowire signal. In addition, we demonstrate real-time monitoring of changes in the action

potential as different ion-channel blockers are applied to cells, and multiplexed recording from cells by independent manipulation of two free-standing nanowire probes.

5.2 Experimental

5.2.1 Nanowire synthesis

V-shaped kinked silicon nanowires with a 60° angle were synthesized by gold nanocluster catalyzed VLS method as previously described^{10,14-16}. Specifically, gold nanoparticles with diameters 80, 100, or 150 nm (Ted Pella) were dispersed on Si substrates with 600 nm SiO_2 (Nova Electronic Materials, Flower Mound, TX). A heavily doped n-type (n^{++}) arm was first grown for 30 min using SiH_4 (1 sccm), PH_3 (4 sccm, 1000 ppm in H_2) and H_2 (60 sccm) at a total pressure of 40 torr and temperature of 460°C . The growth was paused for 15 s by rapidly evacuating the chamber, followed by re-introducing reactant gases to generate the first 120° kink^{10,15,16}. At this point the flux of PH_3 was reduced to 0.1 sccm (from 4 sccm) to decrease the doping level in the segment that serves as the active channel of the nanoFET. Growth of the lightly doped segment was continued for 30-60 s, and then a second 120° kink was introduced by another evacuation/reactant introduction cycle, where PH_3 flux was increased back to 4 sccm and growth was continued for 30 min to complete the other n^{++} arm of the probe. Under these growth conditions the two 120° kinks form a *cis*-geometry with high efficiency to yield an overall 60° probe tip^{10,16}.

The W-shaped kinked nanowires were synthesized by CVD through a nanoparticle-catalyzed VLS process as described previously¹⁶. Specifically, 150 nm diameter gold nanoparticles (Ted Pella) were dispersed on Si growth substrates with 600 nm SiO_2 layer (Nova Electronic Materials). Nanowires were grown at a total pressure of 40 torr and

temperature of 460 °C. The four heavily doped n^{++} arms were grown for 2-16 min respectively (resulting in controlled arm length between 1.45 and 11.60 μm) and every adjacent arms were connected by a 120° kink tip. Lightly doped nanoFET elements with growth time of ~ 45 s were introduced immediately after each kink formation (resulting in controlled nanoFET channel length of ~ 500 nm). Dopant modulation was achieved by varying the flow rates of PH_3 (1000 ppm in H_2) at 4 sccm and 0.1 sccm for heavily doped (Si:P = 250:1) n^{++} - and lightly doped (Si:P = 10,000:1) n-type segments respectively and kept the flow rates of SiH_4 (1 sccm, 99.9999%) and H_2 (60 sccm) constant.

5.2.2 Free-standing probe fabrication

Free-standing probes with V-shaped kinked nanowires were fabricated on a metal sacrificial layer that was deposited on a Si substrate with 600 nm SiO_2 surface layer (Nova Electronic Materials, Flower Mound, TX) using PL and EBL. Key steps used in the fabrication were as follows. (1) PL and metal deposition (100 nm, Ni) were used to define an array of 5 mm x 5 mm sacrificial layer blocks, where each block is sufficiently large for fabrication of a free-standing probe end. (2) The 4.5 mm long bottom passivation layer and main body of the probes was fabricated by spin coating SU8 2002 (2 μm , MicroChem) followed by PL, where one probe body was defined in each sacrificial layer block. (3) Contact pads and interconnects to the tip region were patterned by PL, metal evaporation and lift-off (Cr/Au, 5/200 nm) on top of the bottom SU8 of the probe body. (4) 500 nm thick layer of SU8 2000.5 (MicroChem) was deposited by spin coating, pre-baked at 65 °C for 2 min, and then kinked Si-nanowires dispersed in ethanol solution were deposited in the region near the end of each probe structure. (5) Dark-field optical microscopy was used to identify kinked Si-nanowires with desired orientation in each block near the tip region

of the probe body, and then the chosen nanowires were immobilized on the surface by electron-beam irradiation of the SU8 in this region and post-baking (75 °C for 2 min) to yield a continuous SU8 passivation layer from the probe body defined by PL to the arms of the kinked nanowire. Subsequent development of the SU8 removed all other deposited nanowires. (6) Metal contacts linking the arms of the kinked nanowires to the larger PL-defined probe interconnects were defined by EBL and metallization (Cr/Pd/Cr, 1.5/120/60 nm) on the SU8. (7) Another 500 nm thick SU8 layer was deposited and patterned by EBL to passivate the metal contacts to the kinked nanowire arms while leaving the kinked nanoprobe exposed. (8) A 50 µm thick layer of low stress SU8 with SiO₂ nanoparticles (GLM 2060, Gersteltec) was patterned by PL as top passivation layer for the 4.5 mm long main body of the probe, and then post-baked at 57 °C for 3 h, followed by slow cooling to reduce internal stress, before development and final hard baking¹⁷. (9) Last, 300 and 500 nm thick layers of LOR 3A and S1805 (MicroChem) were deposited by spin-coating on the surface, and a small region covering the nanowire tip end was defined by PL. (10) The probe was released from the substrate by etching the Ni layer (40% FeCl₃:39% HCl:H₂O=1:1:20) in a small petri-dish, and then the solution was exchanged with deionized water. (11) The resulting probe body was manually removed from the solution with tweezers, and excess water was removed on absorbent material (Kimwipes, Kimberly-Clark). Then the probe was aligned and glued (Devcon 5-minute epoxy, ITW) to a printed circuit board connector (PCB_A16, NeuroNexus) on top of a 4 mm long, 15 µm thick silicon lever (raw A-style probe, NeuroNexus). The position of the probe was adjusted such that the nanowire probe extends beyond the Si support lever. (12) The metal pads on the probe and printed circuit board connector were electrically-connected using silver epoxy

(E415G, Epoxy Technology), cured at 55 °C for 3-4 h, and subsequently passivated with silicone elastomer (Kwik-Sil adhesive, World Precision Instruments). Since 12 probe-end structures on a single substrate can be fabricated in ca. 6 days, it is possible to make 12 complete probes in ~7 days and satisfy research requirements.

Fabrication procedures are adjusted for W-shaped kinked nanowires with multiplexed nanoFETs due to lower synthesis yield. Key steps used in the fabrication were as follows. (1) The fabrication substrate (Si with 600 nm SiO₂) with metal position markers defined by EBL (5nm Cr/45 nm Au) was coated with a Ni sacrificial layer and an unexposed SU8 polymer layer (SU8 2000.5, Micro Chem). The W-shaped kinked nanowires on the growth substrate were then dispersed in ethanol by ultrasonication, and transferred to the marker area using a micro-pipette. Once a single nanowire building block with the ideal shape as designed could be identified by a dark-field optical microscope, its location was then registered using the position markers. (2) Based on the position and orientation of the selected W-shaped kinked nanowire, a microscale head piece and a new set of alignment markers were fabricated before the construction of the main probe structure. Specifically, the SU8 layer adjacent to the arms of the nanowire was exposed by EBL to shape the bottom passivation layer with a typical dimension of 200 μm long by 50 μm wide, followed by additional EBL and metallization process to fabricate a common source and two drain metal electrodes (1.5 nm Cr/120 nm Pd/60 nm Cr) on top. In addition, four outer markers were then fabricated by PL. The center and orientation of the markers were aligned with the head piece through a transparent observation window on the photo mask with the same shape and size of the head piece, by adjusting the position and angle/rotation of the fabrication substrate on the photo aligner. In this PL step, a small piece

of aluminum foil was used to block the observation window, so that only the alignment markers were exposed for the following development and metallization (5 nm Cr/50 nm Au). (3) The bottom SU8 passivation layer for the main probe structure, which linked with the existing head piece, was fabricated by PL based on the new set of alignment markers, followed by the PL fabrication of the metal connections that scaled from the existing metal contacts on the head piece to the millimeter-scale bonding area. Last, top SU8 passivation layers with low internal stress of 2 μm and 50 μm thickness (GLM 2060, Gersteltec) were coated over the head piece by EBL and the main probe structure by PL, respectively, using protocols as described above. In addition, a photosensitive protection cap (LOR 3A and S1805, MicroChem) was fabricated around the tip of the probe, similarly to the previous design, to protect the nanowire from the capillary force in the assembly procedures, and to keep it free of contaminations before use in the recording experiments.

5.2.3 Cardiomyocyte culture

Cardiac cells were isolated from intact ventricles of 1 to 4-day old neonatal Sprague/Dawley rats using 3–4 cycles (30 min each) of enzyme digestion using collagenase type II and pancreatin as previously described¹⁸. The cells were suspended in culture medium, composed of Medium-199 (Invitrogen, Grand Island, NY) supplemented with 0.6 mM $\text{CuSO}_4 \cdot 5\text{H}_2\text{O}$, 0.5 mM $\text{ZnSO}_4 \cdot 7\text{H}_2\text{O}$, 1.5 mM vitamin B12, 500 U ml^{-1} penicillin, 100 mg ml^{-1} streptomycin and 5 vol.% fetal bovine serum (FBS). The cardiac cells were seeded onto fibronectin/gelatin coated glass cover-slips at an initial cell density of $0.5\text{-}2 \times 10^5 \text{ cm}^{-2}$. The culture was maintained at 37 °C with 5% CO_2 with the first full medium change in 24 hours, and following change of 50% medium every other day. Electrical measurements were conducted after 3-4 days of culture. All animal procedures

conformed to US National Institutes of Health guidelines and were approved by Harvard University's Animal Care and Use Committee.

5.2.4 Patch-clamp recording

Patch pipettes were pulled from 1.5 mm diameter boron glass tubes (P-97 Flaming/Brown Micropipette Puller, Sutter Instruments). Pipettes were filled with intracellular medium (in mM, potassium gluconate 125, KCl 20, CaCl₂ 0.5, MgCl₂ 2, HEPES 10, EGTA 5, Na₂-ATP 2, pH 7.3), and the resistance was measured with 5 mV pulses to be ~7 MΩ. After a giga-seal was formed, the pipette was held at -70 mV before breaking the membrane to form a whole-cell patch. The data were recorded in current-clamp mode by setting I=0 with sampling rate of 20 KHz using Digi1440A and Clampex 10 software (MDS).

5.2.5 Intracellular recording

A free-standing nanowire probe was first exposed in ultraviolet light (430 nm, 120 s) to sensitize the photoresist protection layer before it was mounted on a micromanipulator (MP285, Sutter Instrument) for control during experiments. The probe tip was then immersed in deionized water in a petri-dish, followed by developer solution (MF-CD-26, MicroChem), which dissolved the protection on the tip. The solution was changed to 1× PBS for 1 h, and then incubated for 2 h with 1 mg/mL lipid vesicles of 1,2-dimyristoyl-sn-glycero-3-phospho- choline (DMPC, Avanti Polar Lipids Inc.) containing 1% 1-myristoyl-2-{12-[(7-nitro-2-1,3-benzoxadiazol-4-yl) amino] dodecanoyl}-sn- glycero-3-phosphocholine (NBD-lipid, Avanti Polar Lipids Inc.) as fluorescent reporter. As described previously, this latter step yields lipid layers on the nanowire surface³. Last, the solution was changed to Tyrode solution (in mM, NaCl 138, KCl 4, CaCl₂ 2, MgCl₂ 1, Na₂HPO₄

0.33, HEPES 10, glucose 10, pH 7.4), and cultured cardiomyocyte cell samples were introduced at 35 °C. A fixed 0.1 V voltage was applied between the source and drain of the probe using a battery source. The resulting current was input to a current/voltage preamplifier (Model 1211, DL Instruments) at sensitivity of 10^{-6} A/V, low-pass filtered (0–3kHz, CyberAmp 380, Molecular Devices) and digitized at 20 kHz sampling rate (Axon Digi1440A, Molecular Devices). A Ag/AgCl reference electrode was used to fix the extracellular solution potential at a constant value of 0 V in all recording experiments. With freshly made lipid solution (used within 1 hour), we have achieved >90% success rate of intracellular recording with lipid coated nanoFET probe (N=25).

5.3 Results and discussion

5.3.1 Free-standing probe design

Separation of a nanoelectronic detector element from much larger interconnections is necessary for internalization of the detector without damaging the cell of interest^{1-3,10}. To date, all approaches^{7-13,18} have focused on fabricating nanodevices on planar substrates, where the detector protrudes from the surface and target cells are brought into contact with the nanodevices by direct seeding and culture^{7-9,18} or manipulation of a culture substrate¹⁰⁻¹³ (**Fig. 5-1a**). These studies have enabled demonstration of new nanodevice concepts and multiplexed detection, but also have limitations, including, (1) device positions are determined during chip fabrication and cannot be reconfigured during an experiment, (2) it is difficult to target specific cells or subcellular regions and (3) minimally-invasive *in vivo* measurements are difficult. In comparison, a free-standing probe that can be manipulated in 3D (**Fig. 5-1b**) would allow targeting of specific cells cultured on substrates or within tissue, although the size of manipulator for such probes will limit multiplexing

compared to chip-based methods^{2,3}. In this regard, development of a general strategy to present nanoelectronic device elements, such as the kinked silicon nanowire nanoFET¹⁰, in free-standing probe structure could expand substantially the capabilities and applications of these devices in electrophysiology.

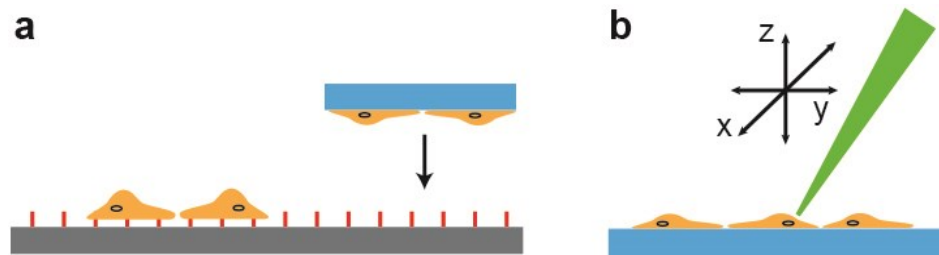


Figure 5-1. Intracellular recording methods. **a**, Schematic (side view) of typical recording approach using chip-based device arrays (red) anchored on a planar substrate (grey). Cells (yellow) are usually cultured directly on top of the devices or cultured on a separate substrate (blue), which would be moved into contact with the devices. **b**, Schematic of a free-standing probe, where the probe (green) moves freely in 3D space to target selected cells and/or cell regions.

5.3.2 Fabrication and assembly of free-standing nanowire probes

The realization of free-standing probes with nanoelectronic device tips requires bridging length scales from the nanoscopic to the macroscopic in a manner that yields robust electrical and mechanical properties. We focus on meeting these challenges for kinked silicon nanowire nanoFET tips as a general example of a two-terminal active nanoelectronic device. In this case, the nanowire arms of the kinked structure serve as nanoscale connections that must be electrically and mechanically connected to the macroscopic handle serving as input/output to measurement electronics. Our free-standing kinked nanowire probe fabrication involves two overall stages (**Fig. 5-2**): (1) lithographic patterning of a nanometer-to-millimeter probe-end and (2) mechanical assembly of the probe end to a millimeter-to-macroscale probe body.

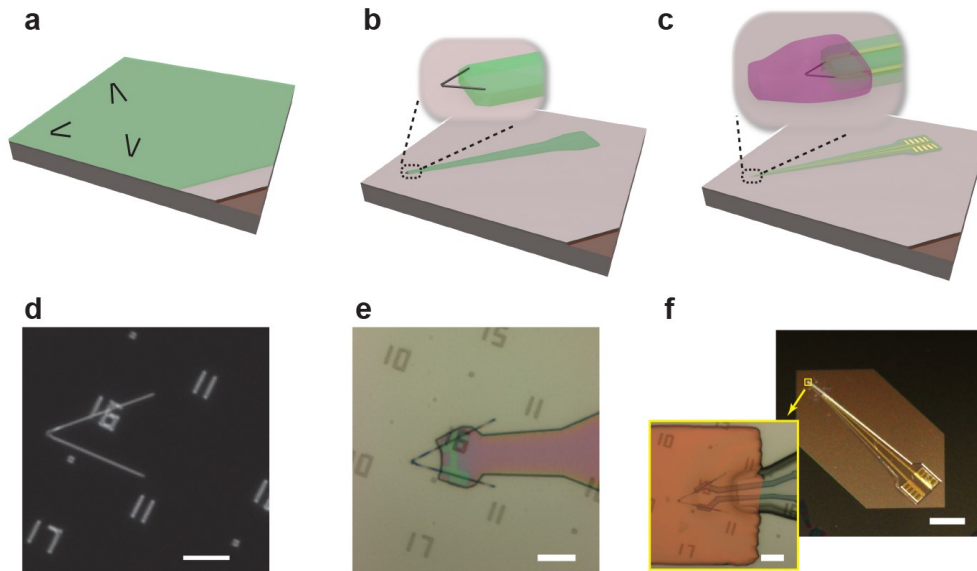


Figure 5-2. Fabrication of free-standing nanowire probes. **a**, Si substrate with 600 nm SiO₂ on surface (brown) coated with a Ni sacrificial layer (pink) and a SU8 polymer layer (light green), and showing deposited kinked silicon nanowires (black). **b**, A kinked nanowire with the desired orientation was identified and fixed on the substrate by EBL (inset), and bottom structure/passivation layer for the full probe body (light green) was defined by PL. **c**, Metal connections (golden) from the nanowire to the macroscopic contact pads, and top passivation layers were fabricated by EBL and PL steps (light green), and then the nanowire was protected by an additional photoresist cap (inset, pink). **d**, Dark-field optical image showing a selected kinked nanowire on top of the SU8 layer, as well as the metal alignment markers below the SU8 layer, which are used in registration of subsequent lithography steps. Scale bar: 10 μm . **e**, Bright-field optical image of the tip end that highlights the kinked silicon nanowire and the underlying patterned SU8 probe body. Scale bar: 10 μm . **f**, Digital camera image of a fully fabricated probe on the Ni sacrificial layer. Scale bar: 1 mm. The inset shows a bright-field optical image of the probe tip with the photoresist protection cap over the nanowire device. The photoresist protection cap is false-colored in orange for clarity. Scale bar: 10 μm .

Key steps in the probe-end fabrication are as follows (**Fig. 5-2a-c**). First, kinked Si nanowires with nanoFETs encoded synthetically at the kink tip¹⁵ were selectively deposited on a substrate coated with sacrificial nickel and SU8 photoresist layers (**Fig. 5-2a**). A representative optical image (**Fig. 5-2d**) shows the resulting kinked nanowire and lithography alignment markers. Second, EBL and PL were used to define the kinked nanowire tip region and the probe body in the SU8 layer, respectively (**Fig. 5-2b**). **Fig. 5-**

2e shows the kinked nanowire region after these steps. Metal interconnects and top SU8 passivation were fabricated, and a photosensitive protection cap was defined at the tip (**Fig. 5-2c**). This cap protects the nanowire tip from capillary forces and contamination during assembly to the probe body and storage prior to cell experiments. Images of a completed probe-end structure (**Fig. 5-2f**) show the overall probe structure and protection cap at the wired-up nanowire tip-end. The probe-end structures are easily fabricated in parallel. We processed 3 x 4 arrays of probes on substrates of about 3 x 3 cm² (**Fig. 5-3**), and larger arrays could be fabricated using EBL instruments capable of handling larger substrates.

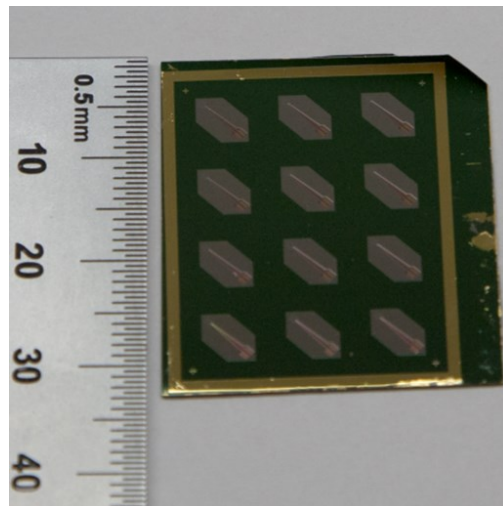


Figure 5-3. Parallel multi-probe fabrication. A 3 x 4 array of kinked nanowire probes fabricated in a single batch; the image was recorded prior to release and attachment of free-standing probe to the printed circuit board connector. A larger number of probes could be batch fabricated using larger substrates, where the size limitation in this demonstration was determined by the EBL instrument (JEOL JSM-7000F) sample chamber.

To complete the probe we assemble the probe-end structure to a printed circuit board (**Fig. 5-4a**). A silicon microlever shorter than the nanowire/SU8 probe structure was glued to the printed circuit board, and then the probe-end structure, released by Ni underlayer etching, was removed from solution (**Fig. 5-4b**), aligned, glued, and

electrically-connected to the microlever/printed circuit board. An image of an assembled probe (**Fig. 5-4c**) highlights the electrical connection and microlever support; a zoom of the tip region (**Fig. 5-4d**) shows the nanowire/SU8/metal interconnect structure and protection cap of the probe end.

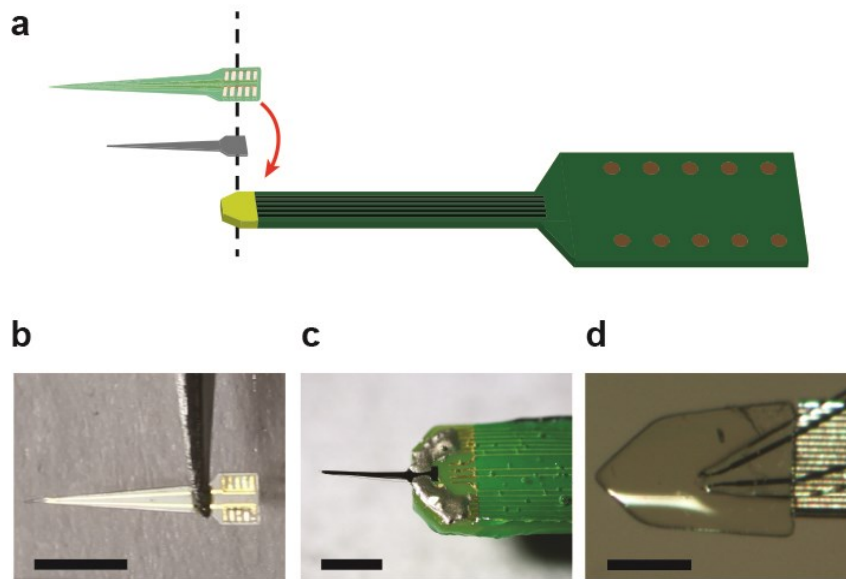


Figure 5-4. Assembly of free-standing nanowire probes. **a**, Schematic of the assembly of a probe onto a printed circuit board connector body (yellow and dark green). A thin Si lever support (grey) was first glued on the printed circuit board connector, and then the nanowire/SU8 probe body (light green) was aligned and attached on top. The length of the polymer probe is longer than the Si lever so that the kinked nanowire is fully suspended. For clarity, sizes are not to scale. **b**, Digital camera image of the nanowire/SU8 probe body released from the substrate after etching. Scale bar: 2 mm. **c**, Digital camera image of the fully assembled probe on the printed circuit board connector. Scale bar: 2 mm. **d**, Bright-field optical image of the suspending nanoFET probe on top of the Si lever with the photoresist protection cap. Scale bar: 100 μ m.

5.3.3 Intracellular recording using free-standing nanowire probes

We used the free-standing nanowire probes alone or with a second independent probe to interrogate live cells (**Fig. 5-5a**). All measurements were carried out in an inverted microscope with probes mounted in XYZ manipulators and temperature-regulated cell

medium (**Fig. 5-5b**). Prior to measurements, the photosensitive protection cap on the end of the nanowire probe was removed in solution, and for cell measurements the nanowire end was coated with phospholipid layers, as described previously¹⁰⁻¹².

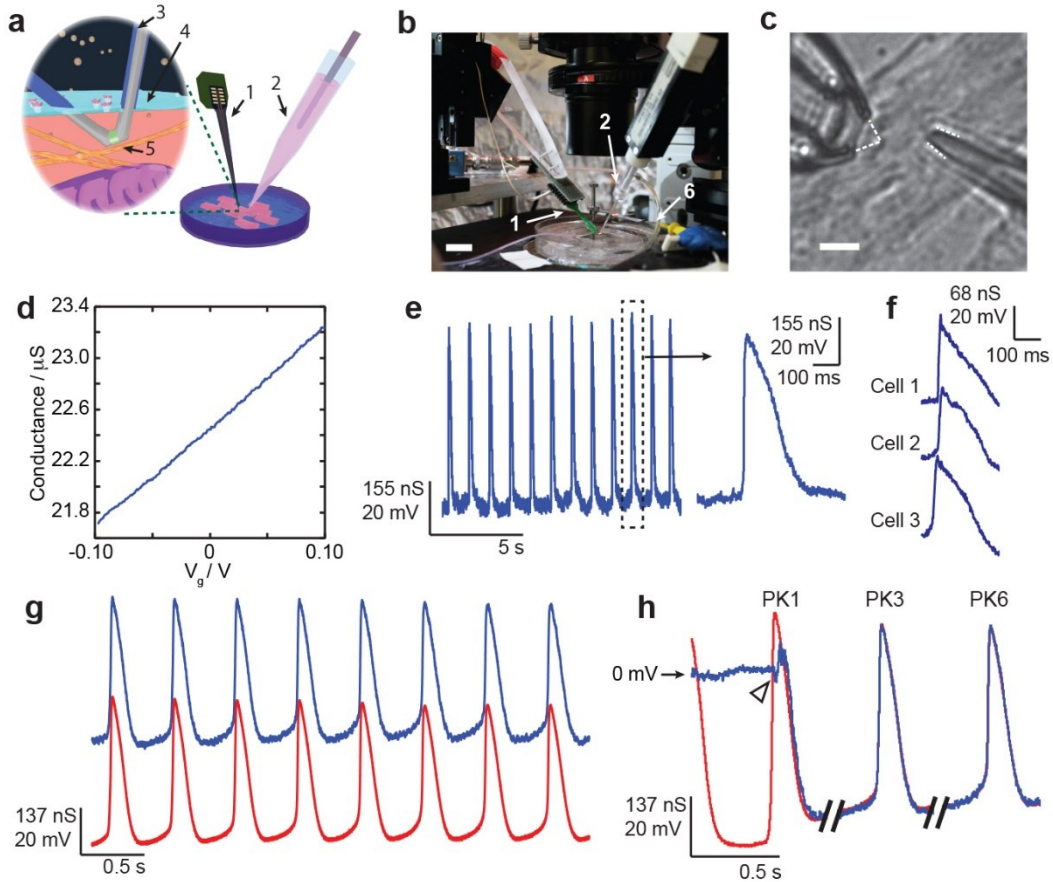


Figure 5-5. Intracellular recording using free-standing nanowire probes. **a**, Schematic illustrating general experiment set-up. A free-standing nanowire probe (1) is mounted on an XYZ micromanipulator to target selected cells and record intracellular signals, and a patch-clamp pipette (2), which is also mounted on a manipulator, can be used to monitor the same cell simultaneously. The nanowire is coated with a phospholipid layer (3) to facilitate penetration through the cell membrane (4) so that the nanoFET (5) is inside the cytoplasm. **b**, Digital camera image of the experiment setup where free-standing nanowire (1) and patch-clamp (2) probes are visible. An Ag/AgCl reference (water-gate) electrode (6) was used as reference. Scale bar: 2 cm. **c**, Differential interference contrast image of the kinked nanowire probe (left) and patch-clamp pipette (right) recording from the same cell. Scale bar: 5 μm . The white dashed lines highlight the kinked nanowire and micropipette inner diameter. **d**, Conductance vs. water-gate data for a typical free-standing nanowire probe recorded with S/D voltage of 0.1 V. **e**, Intracellular action potentials recorded from a spontaneously beating cardiomyocyte using the nanoFET probe (blue). Right: zoom-in of a single action potential. **f**,

(Continued) Representative intracellular action potential peaks recorded from three different cells using the same probe consecutively; the probe was not cleaned between trials. **g**, Simultaneous data recorded by a free-standing nanowire probe (blue) and patch-clamp (red, current-clamp mode, $I_{\text{clamp}}=0$) from the same spontaneously beating cardiomyocyte. For clarity, signals are offset vertically. **h**, Raw signals recorded from the nanoFET probe (blue) and the patch-clamp (red) as the nanoFET approaches the cell. The triangle marks the time when the nanoFET enters the cell. PK1, PK3 and PK6 mark the 1st, 3rd and 6th action potential peaks, respectively.

A differential interference contrast image showing the ends of a free-standing nanowire probe and patch-clamp micropipette recording from a single cultured cardiomyocyte cell (**Fig. 5-5c**) highlights the capability of targeting the nanowire probe to specific cell regions and its smaller tip size compared to a patch-clamp micropipette. The sensitivity of these nanoFET probes was characterized before and after cell measurements so that recorded conductance data can be presented as potential (millivolts) values. Representative data recorded in PBS solution (**Fig. 5-5d**) yields a sensitivity (7730 nS/V) similar to previous values for chip-based kinked nanowire devices¹⁰ and to the average (8500 ± 4300 nS/V) for probes in our studies. Significantly, the variation in nanoFET sensitivities before and after cell measurements was <10% and often only ~1%, which shows that the probes provide reproducible, quantitative potential data.

Data recorded with a phospholipid-modified free-standing nanowire probe from spontaneously beating rat neonatal cardiomyocytes (**Fig. 5-5e**) exhibit regular peaks with amplitude (67 mV), duration (260 ms) and shape characteristic^{19,20} of intracellular cardiac action potentials. The intracellular action potential peaks were observed 1-20 s after the phospholipid-modified nanoFET was brought into gentle contact with the cell membrane using the 40 nm step resolution of the manipulator, and they disappeared when the probe was retracted from the membrane. We were unable to record intracellular action potential

signals with unmodified nanoFET probes. These results are consistent with biomimetic membrane fusion^{10-13,21}, and the high positioning accuracy of our free-standing probes should enable future studies of targeting and internalization with specific ligand/receptor functionalized²²⁻²⁴ probe tips.

In addition, comparison of intracellular action potential peaks recorded sequentially from three cells using the same nanowire probe (**Fig. 5-5f**) shows that these similar action potential signals have amplitudes of 51, 46 and 56 mV for cells 1, 2 and 3, respectively. These recorded action potential amplitudes are consistent with the average values determined from independent nanoFET and patch-clamp probes, $55 \text{ mV} \pm 16 \text{ mV}$ ($N = 15$) and $58 \text{ mV} \pm 25 \text{ mV}$ ($N = 13$), respectively, on similar cultured cardiomyocytes (DIV3). These results show that our free-standing nanowire probes can be used in multiple measurements on arrays of cells or cell networks, which could improve the efficiency of such studies compared to patch-clamp measurements where the glass pipette is replaced for each try on a new cell.

We also carried out simultaneous measurements on the same cell using both kinked nanowire and patch-clamp probes (**Fig. 5-5a,c**). In these experiments, we first established intracellular recording with patch-clamp in the whole-cell current-clamp mode, and then brought the kinked nanowire probe into contact with the cell to establish the nanoFET intracellular signal. These data exhibit several key features. First, qualitative inspection of the simultaneous intracellular action potential signals from the nanoFET and patch-clamp (**Fig. 5-5g**) show that they are very similar in absolute amplitude and time-dependent shape. Second, analysis of the signal changes as the nanoFET enters the cell (**Fig. 5-5h**) reveals that, there was a ca. -50 mV baseline jump as the nanoFET crosses the cell membrane (**Fig.**

5-5h, triangle), and that, after this first entry peak, all subsequent action potential signals from the nanoFET and patch-clamp (**Fig. 5-5h**, blue and red, respectively) overlap identically with a 65 mV peak amplitude.

A small depolarization (~ 8 mV) in the resting potential of the patch-clamp was observed as the nanowire probe entered the cell, which is probably because of leakage of the patch electrode membrane seal and not nanoFET leakage, as follows. First, the patch-clamp recording is sensitive to the contact between the nanoFET and cell membrane, and we have observed that touching but not penetrating cell membranes with the nanoFET can lead to depolarization and/or loss of patch-clamp signals. Second, independent single probe experiments show that the mean stable action potential recording time for the nanoFET probe, five minutes ($N = 10$), is longer than that for the patch-clamp probe, 2.4 minutes ($N = 11$), using the same experimental set-up. Third, extended recording with a nanoFET probe (**Fig. 5-6**) yields full-amplitude 85 mV action potential signals over a five minute period with $<3\%$ loss of signal amplitude, thus demonstrating a high-quality membrane seal and minimal effect on the physiological status of the cell by nanoFET insertion.

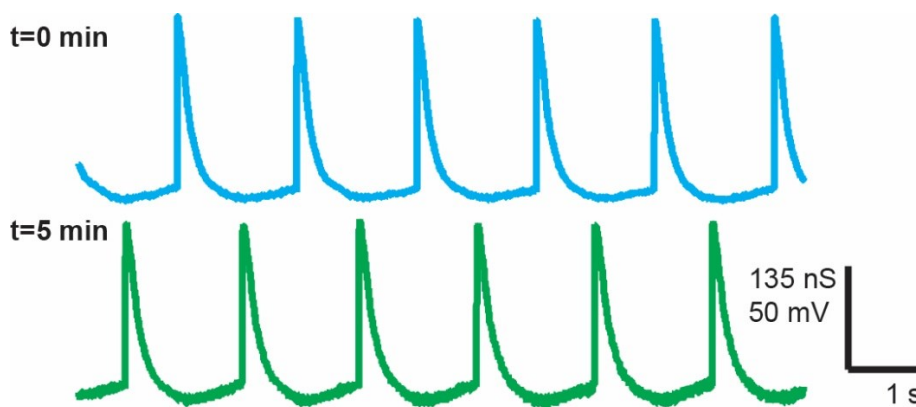


Figure 5-6. Stability of nanoFET intracellular recording. Initial trace (cyan; time, $t = 0$ min) and a subsequent trace (green) after 5 min of continuous measurement from the same beating cardiomyocyte cell. The $t = 0$ min trace corresponds to ca. 1 min following internalization of the nanoFET into the cell. The amplitude (mV)/frequency (Hz) of the

(Continued) action potentials in the $t = 0$ and 5 min traces are 85/0.6 and 83/0.6, respectively. The results demonstrate highly stable action potential recording using the nanoFET probes, and the absence of apparent leakage on the 5 min time scale, even for beating cells. In addition, these results are consistent with the average stable recording time, 5.4 min (N = 10), and are substantially longer than the average stable recording time we could achieve with the patch-clamp on the same culture of cells and manipulator setup, 2.4 min (N = 11).

Significantly, only two parameters intrinsic to the nanoFET are used to convert probe conductance to local potential: (1) the extracellular conductance baseline, which is assigned zero potential (**Fig. 5-5h**, black arrow), and (2) the sensitivity of the nanoFET. Hence, the agreement of both position and shape between the two traces is the first and only direct evidence to date for minimally-invasive intracellular recording by a nanodevice. Moreover, these data clearly differentiate our nanoelectronic probes from other intracellular-like recordings based on high seal resistance around extracellular electrodes and localized electroporation^{7-9,25}. In addition, the average amplitude of the action potentials, $55 \text{ mV} \pm 16 \text{ mV}$ (nanoFET, N = 15) and $58 \text{ mV} \pm 25 \text{ mV}$ (patch-clamp, N = 13), and rest potentials, $-37 \text{ mV} \pm 10 \text{ mV}$ (nanoFET) and $-43 \text{ mV} \pm 13 \text{ mV}$ (patch-clamp), obtained from single-probe recording experiments are indistinguishable statistically. Last, the highest amplitudes of action potentials reach 90 mV (**Fig. 5-7**) thus confirming the high quality of the nanoFET/cell membrane junctions.

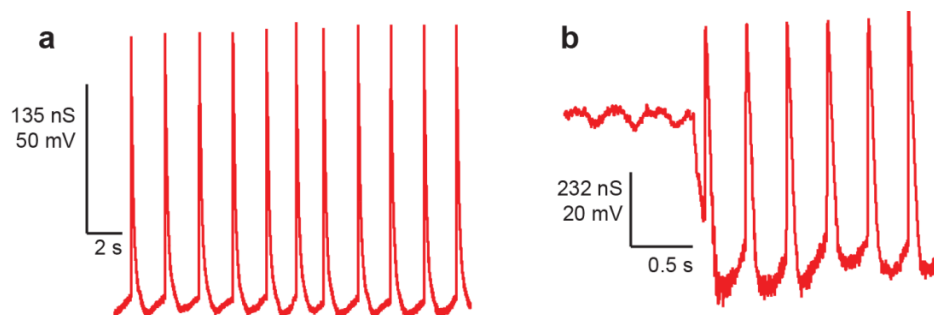


Figure 5-7. Full amplitude action potentials and resting potential recorded by nanoFET probes. **a**, Stable action potential signals from beating cardiomyocyte with amplitude of 90 mV. **b**, Baseline shift corresponding to a resting potential of -47 mV, with action potential amplitude of 70 mV. The data shown in **a** and **b** were recorded in separate experiments using distinct nanoFET probes and cells (both DIV3).

Our free-standing kinked nanowire probes were also used to characterize quantitatively the effects of ion-channel blockers on recorded intracellular action potentials. First, the L-type Ca^{2+} -channel blocker nifedipine was injected into the medium after a stable intracellular action potential recording was established from a cardiomyocyte cell. Monitoring of the nanoFET signal (**Fig. 5-8a**) shows a constant action potential peak amplitude and progressive decrease in the FWHM of 147, 130, and 102 ms at times 0, 60 and 110 s, respectively, after nifedipine injection. The decrease in action potential peak FWHM at constant peak amplitude are consistent with a decrease in Ca^{2+} current caused by nifedipine binding²⁶. Second, addition of Na^{+} channel blocker tetrodotoxin (TTX) monitored in a separate experiment (**Fig. 5-8b**) shows a rapid decrease in the initial fast rising (depolarization) edge and corresponding decrease in the peak amplitude of the action potential versus time. The slopes (V/s)/peak amplitudes (mV) were 3.42/44, 1.73/28, 0.78/20 and 0.53/13 for 0, 3, 12 and 22 s, respectively, after TTX addition, and are consistent with the suppression of the inward Na^{+} current caused by TTX binding²⁶. These results confirm that nanoFET probes record details of intracellular action potential changes

in a reliable and robust manner, and show that it can be a tool for drug screening and cell signaling studies in the future.

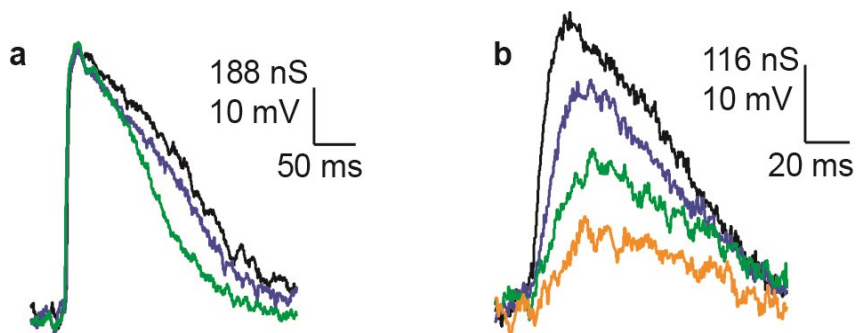


Figure 5-8. Ion-channel blocker tests using free-standing nanowire probes. a, Intracellular action potential peaks recorded from nanoFET at 0 s (black), 60 s (blue), and 110 s (green) after adding 10 mM nifedipine (5 μ l, DMSO solution) to the medium. **b,** Intracellular action potential peaks recorded from nanoFET at 0 s (black), 3 s (blue), 12 s (green) and 22 s (orange) after adding 1 mM TTX (1 ml, aqueous solution) to the medium.

5.3.4 Multiplexed recording with two nanoFET probes

We explored using two nanoFET probes in multiplexed recording experiments. For example, two distinct nanoFET probes mounted on independent manipulators (**Fig. 5-9a**) were used to target cultured cardiomyocyte cells precisely, including two adjacent cells with well-defined alignment (**Fig. 5-9b**) and a single cell (**Fig. 5-9c**). Targeting with submicron resolution was readily achieved using differential interference contrast imaging, and could be improved further using fluorescence imaging. Representative data recorded from two nanoFET probes as they are sequentially brought into contact and internalized by two adjacent cardiomyocytes (**Fig. 5-9d**) highlights several key points. First, following gentle contact of the phospholipid-modified probes with the cell (40 nm step resolution), both probes show a short (\sim 2 s) time delay before intracellular action potential peaks appeared, and stable full-amplitude action potentials developed after several additional

seconds. Second, the full-amplitude action potentials recorded with probe-1 and probe-2 (50 and 45 mV, respectively) are consistent with both independent patch-clamp measurements and the literature²⁷ for neonatal (versus adult) cardiomyocytes. The extracellular-to-intracellular baseline shifts can also be smaller for these neonatal cells (that is, -20 mV for probe-2 versus -43 mV for probe-1) but are consistent with the stage of our neonatal cell culture²⁷. These multiplexed studies further highlight the robustness of our free-standing nanowire probe fabrication and the potential to characterize action potential timing differences for precisely defined nanoprobe/cell configurations and structures too small for conventional patch-clamp measurements, such as dendritic spines²⁸. Moreover, the capability to specify with high-resolution the specific cells and/or cellular regions targeted by the nanoFET detectors represents an advantage compared to multiplexed recording with nanoelectronic probes fabricated on planar substrates. The physical dimensions of the manipulators used for targeting nanoFET probes will limit level of multiplexing compared to chip-based methods^{2,3}, although studies incorporating kinked nanowire structures with synthetically-encoded multiple nanoFET sensors¹⁶ could mitigate this by increasing the number of detectors on each probe, as shown below.

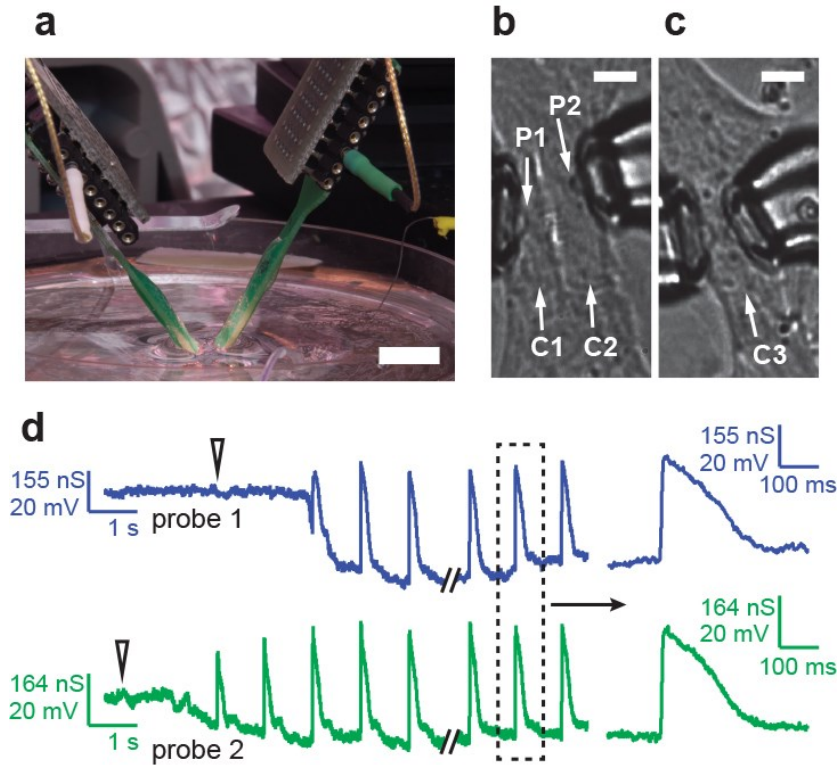


Figure 5-9. Multiplexed recording with two free-standing nanowire probes. **a**, Digital camera image of a measurement setup using two independent free-standing nanowire probes, where each probe is mounted on an independent XYZ micromanipulator. Scale bar: 1 cm. **b,c**, Differential interference contrast images of the kinked nanowire probes during multiplexed recording. Probes P1 and P2 are positioned at two adjacent cardiomyocytes C1 and C2, respectively (**b**). The two probes are positioned within submicron separation on the same cardiomyocyte cell, C3 (**c**). Scale bars, 10 μm . **d**, Multiplexed intracellular action potentials recorded with the dual-kinked nanowire probe setup from two adjacent cardiomyocytes (left). The triangles mark the time of contact between the nanowire tips and the cells. Zoom-ins of the action potentials marked by the dashed box are shown on the right.

5.3.5 Multiplexed recording with W-shaped kinked nanowire probe

In order to take advantages of the W-shaped kinked nanowires with parallel nanoFETs discussed in Chapter 3 for multiplexed intracellular recording, the free-standing probe fabrication procedures are adjusted to enhance overall yield. The four key steps of fabricating free-standing multiplexed nanowire transistor bioprobes using W-shaped

kinked nanowires are illustrated in **Fig. 5-10**. First, the fabrication substrate (Si with 600 nm SiO₂) with metal position markers defined by EBL (5nm Cr/45 nm Au, black crosses, **Fig. 5-10a**) was coated with a Ni sacrificial layer and an unexposed SU8 polymer layer. The W-shaped kinked nanowires on the growth substrate were then dispersed in ethanol by ultrasonication and transferred to the marker area using a micropipette (**Fig. 5-10a**). Once a single nanowire building block with the ideal shape as designed could be identified by a dark-field optical microscope (in red, inset, **Fig. 5-10a**), its location was then registered using the position markers (**Fig. 5-10a**). An example dark-field image of a selected W-shaped kinked nanowire among the position markers is shown in **Fig. 5-10e**.

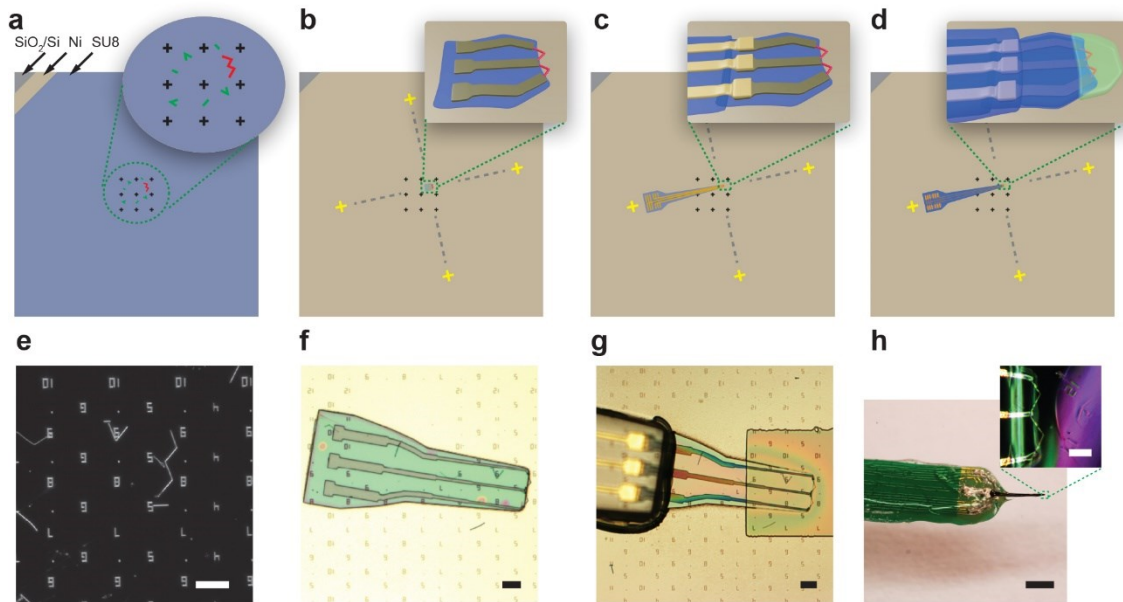


Figure 5-10. Key steps of fabricating free-standing probes with selected W-shaped Si kinked nanowire. **a**, Si substrate with 600 nm SiO₂ and metal markers (black crosses) coated with Ni sacrificial layer and SU8 polymer layer, where silicon kinked nanowires were deposited on the top. Inset: Magnified position marker area, where one W-shaped Si kinked nanowire with desired characteristics was selected (red) among the byproducts and nanowires that did not have the proper geometry (green). **b**, The head piece fabricated by EBL steps around the selected Si kinked nanowire (inset), which included the bottom SU8 layer (blue) and metal contacts (brown, 1.5 nm Cr/120 nm Pd/60 nm Cr). A set of alignment markers (yellow crosses) were defined by additional aligned PL steps to precisely designate the position and orientation of the head piece (dotted gray lines). **c**,

(Continued) The bottom SU8 layer (blue) of the main probe body and metal connections (golden, 5 nm Cr/200 nm Au) from the head piece to the macroscopic bonding pads were fabricated by PL using the new alignment markers. **d**, Top passivation layers over the head piece and the main probe body (blue) were fabricated by EBL and PL steps. The nanowire was then protected by a photosensitive protection cap (inset, green). **e**, Dark-field optical image showing a selected W-shaped Si kinked nanowire on top of the SU8 layer. The metal position markers are below the SU8 layer for the registration of subsequent lithography steps. Scale bar: 20 μm . **f**, Bright-field optical image of the head piece which highlights the Si kinked nanowire at the tip, the bottom SU8 passivation layer, and the metal contacts. Scale bar: 20 μm . **g**, Bright-field optical image of the probe tip with the top passivation layers and the photoresist cap over the nanowire device. The top passivation layer of the main probe body is over 50 μm thick (vs. 2 μm for the head piece) to provide stronger mechanical strength and therefore it is out of focus in the image. Scale bar: 20 μm . **h**, Digital camera image of a fully assembled probe on the printed circuit-board connector. The metal pins at the other end of the connector are not shown. Scale bar: 2 mm. Inset: Dark-field optical image of the suspending Si kinked nanowire nanoFET embedded in the photoresist protection cap at the tip of the probe. Scale bar: 10 μm .

Second, based on the position and orientation of the selected W-shaped kinked nanowire, a microscale head piece and a new set of alignment markers were fabricated before the construction of the main probe structure (**Fig. 5-10b**). Specifically, the SU8 layer adjacent to the arms of the nanowire was exposed by EBL to shape the bottom passivation layer with a typical dimension of 200 μm long by 50 μm wide, followed by additional EBL and metallization process to fabricate S/D metal electrodes (1.5 nm Cr/120 nm Pd/60 nm Cr) on top (inset, **Fig. 5-10b**). The contacts and the bottom passivation layer constituted the head piece, designating the position and orientation of the nanowire building block, as well as forming the initial contacts with the silicon nanowire. The optical image of a finished head piece is shown in **Fig. 5-10f**, highlighting the W-shaped kinked nanowire at the tip of the piece, and the three contact electrodes on top of the SU8 passivation layer. In addition, four outer markers were then fabricated by PL (yellow crosses, **Fig. 5-10b**). The center and orientation of the markers were aligned with the head piece through an

observation window on the photo mask, as indicated by the grey dotted line in **Fig. 5-10b**. Third, the bottom SU8 passivation layer for the main probe structure, which linked with the existing head piece, was fabricated by PL based on the new set of alignment markers, followed by the PL fabrication of the metal connections that scaled from the existing metal contacts on the head piece to the millimeter-scale bonding area (**Fig. 5-10c**). Last, top SU8 passivation layers with low internal stress¹⁷ of 2 μm and 50 μm thickness were coated over the head piece by EBL and the main probe structure by PL, respectively, using protocols as described above¹⁷. In addition, a photosensitive protection cap (inset, marked in green, **Fig. 5-10d**) was fabricated around the tip of the probe, similarly to the design described above, to protect the nanowire from the capillary force in the assembly procedures, and to keep it free of contaminations before use in the recording experiments.

We follow the same procedures to complete the assembly of the final probe for recording. The picture of a fully assembled probe is shown in **Fig. 5-10h**, which highlights the electrical contacts, the microlever support beneath the SU8 probe structure, the probe-end on the top, and the silicone insulation. The inset micrograph of **Fig. 5-10h** shows the magnified area of the tip of the probe-end, where the suspending W-shaped kinked nanowire is embedded in the protection cap with one common source contact at the center and two drain contacts on the side arms.

In addition, we have demonstrated the first multiplexed intracellular recording from the same cardiomyocyte cell using a single W-shaped kinked nanowire bioprobe. Specifically, the dual-nanoFET probe was mounted on a micromanipulator with a typical 60° angle from the horizontal plane for accurate positioning in 3D space. The UV-sensitive protection cap was first exposed in UV light and dissolved in MF-CD-26 (MicroChem) to

reveal the fresh surface of the nanowire device, followed by coating of the nanowire with phospholipid bilayers, using similar preparation procedures as described above. The recording experiment was then conducted in HEPES-based buffered recording medium with temperature regulated at 35 °C. Before introducing the cells, the sensitivities of both nanoFETs were obtained by the water-gate measurement. Briefly, a 0.1 V bias was applied on the common source electrode at the center with the drain electrodes at both sides connected to ground through two current preamplifiers with a sensitivity of 10^6 V/A. The conductance of both devices was monitored as the chemical potential of the recording medium was changed from -0.1 V to +0.1 V using a Ag/AgCl as the reference electrode. The typical results are shown in **Fig. 5-11a**, from which we can calculate the sensitivity of the nanoFETs as 10.8 $\mu\text{S/V}$ (red) and 19.2 $\mu\text{S/V}$ (blue), respectively. These results are consistent with the performance of the planar devices fabricated using the W-shaped nanowires synthesized with the same protocol¹⁶. The sensitivity data can then be used to convert the change of conductance of each device to the potential change at the surface of each nanoFET.

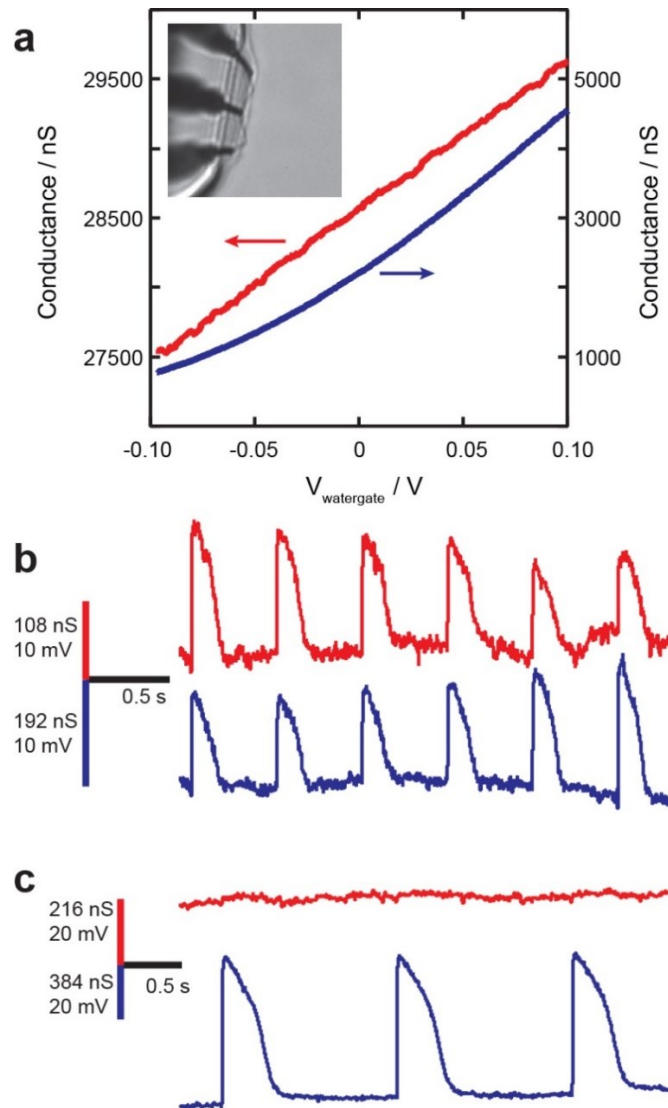


Figure 5-11. Multiplexed intracellular recording using the free-standing dual-nanoFET probe. **a**, Conductance versus water-gate data for a typical free-standing dual-nanoFET probe after removing the photoresist protection cap and coating with phospholipid bilayer, with S/D voltage of 0.1 V. Inset: Bright-field optical image of the probe in recording solution using an inverted microscope. The probe was mounted on the micromanipulator with a 60° angle from the horizontal plane. The suspending arms of the nanowire in the inset image appear shorter than their actual length due to the steep angle of the probe. **b**, Data recorded simultaneously from both nanoFETs in contact with the same spontaneously beating cardiomyocyte. Both devices showed signals with intracellular characteristics. **c**, Data recorded simultaneously from both nanoFETs while one nanoFET was in better contact with the spontaneously beating cardiomyocyte and leaving the other nanoFET deviating slightly from the cell. Only the nanoFET device in contact with the cell showed strong intracellular signal (blue).

Spontaneously beating cardiomyocyte cells cultured on a thin PDMS substrate were then introduced to the recording chamber on the inverted microscope; the probe was positioned close to a selected cell using the micromanipulator with submicrometer accuracy in the x-y plane (limited by imaging quality) and brought down to form gentle contacts with the cell with 40 nm step size in the z-distance. We have typically observed the devices picking up signals with intracellular action potential characteristics^{19,20} within 20 s after the contact was formed. Representative traces from both devices are shown in **Fig. 5-11b**, which gives simultaneously recorded signals from both nanoFETs, with amplitudes of 14 ± 2 mV and 10 ± 2 mV, and durations of 133 ± 6 ms and 129 ± 6 ms, respectively (n=6). We note that the amplitudes of both signals were smaller and less stable than the typical values of action potentials recorded using one single-kinked nanoFET bioprobe, and there were small variations in amplitudes and shapes between the signals from the two devices, although all signals were tightly synchronized by the fast rising edge ($\Delta t < 10 \mu\text{s}$). This indicates that the devices were not yet at the optimal position inside the cell for intracellular recording, and the sealing of the devices at the cell membrane was not stable. In order to further clarify these discrepancies, a control experiment was designed in which we tuned the lateral mounting angle of the probe on the manipulator $\sim 30^\circ$ toward the side arm of the W-shaped nanowire which has one nanoFET on it. As a result, the nanoFET on the side arm should form a better contact with the cell with a shallower access angle, while leaving the other device deviating slightly from the cell. As shown in **Fig. 5-11c**, only the device in contact with the cell gave pronounced intracellular action potential signals (blue trace) with amplitude of 52 ± 3 mV and duration of 129 ± 2 ms, which were consistent with previous reports¹⁰ and results shown above, while the other device was

silent (red trace). Therefore, we tentatively attribute the nonideal quality of the signals recorded with dual-nanoFETs from a single cell to the geometric limitations of the device in the current synthetic design. Namely, the channel length of the nanoFETs is ~ 500 nm, and the extending length of the nanowire from the edge of the SU8 passivation layer at the tip of the probe is 1-2 μm . When the devices were set with an angle to touch the cell together, both nanoFETs have to travel >250 nm from the cell surface to gain full access to the cytoplasm due to the 120° opening angles of the kinks. Furthermore, in practice, the error in nanowire arm length and misalignment in the orientation of the devices could require even longer travel distance to gain full intracellular signals from both devices, which makes the position control quite difficult to avoid damage to the cell and obtain stable recordings. Consequently, when we obtained reasonable level of signals from both devices before hurting the cell, the nanoFETs were most likely not fully inside cell yet, resulting in weaker signals. In addition, the relatively large 120° angles between the nanowire arms here compared to previously 60° angle in the case of a single-kinked probe and the close distance (<10 μm) between the devices led to larger cross section when both devices entered the cell and a higher probability of damage and leakage, which could also degrade the quality of signal. Nevertheless, we also note that the geometry of the probes could be optimized by a more elaborate synthetic design to address the existing issues by incorporating ultrasmall U-shaped kinked nanowire structures discussed in Chapter 3 and further reducing the diameter of the nanowire¹⁶. Importantly, the fabrication framework demonstrated in this section could still be applied without modification to the preparation of bioprobes based on the more complex nanowire building blocks.

5.4 Conclusion

We have demonstrated a robust approach for the fabrication of free-standing silicon kinked nanowire probes with encoded nanoFET detectors at the tip ends. These probes have been manipulated in 3D with submicron precision to target specific cells and/or cell regions and record stable full-amplitude action potentials from spontaneously beating cardiomyocytes. Simultaneous measurements from the same cell made with kinked nanowire and patch-clamp probes showed that the same action potential amplitude and temporal properties were recorded without corrections to the raw nanowire signal, which thus demonstrates the first direct evidence for a minimally invasive, true intracellular recording by a nanodevice. In addition, we demonstrated real-time monitoring of action potential changes as different ion-channel blockers are added to cells, and multiplexed recording from adjacent cells with precisely defined alignment and separation using two independent nanoFET probes. Moreover, we showed that the fabrication procedures can be adjusted for W-shaped kinked nanowires to achieve multiplexed recording with a dual-nanoFET probe from a single cell. The signal-to-noise ratio of our single nanoFET probe (~ 100) is comparable to or smaller than those of vertical nanowire arrays (~ 100 (ref. 8) and ~ 590 (ref. 7)), although the effective areas of these passive nanoprobe are >50 times larger than our nanoFET probes. Hence, a direct comparison of signal and noise between these experiments is difficult to make because the signal and bandwidth will be substantially degraded for these other devices when reduced to the same size as our current nanoFET probes.

Although future studies are needed to extend the performance and biochemical functionality of our free-standing nanowire probes, we believe this work opens up a number of interesting directions. First, our general approach for fabricating free-standing

probes could be applied to other nanoelectronic building blocks that have been used in chip-based format^{11-13,16}. For example, the use of U-shape kinked nanowire structures would yield ultra-small nanoFET detectors with very high aspect ratio¹⁶, and thus enhance capabilities for specific targeting, multiplexed experiments and deep tissue/cell insertion and detection with subcellular resolution. Second, the small detector size and absence of ion exchange for our nanowire probes could facilitate studies of high-input impedance cells, such as cystic artery²⁹, fibroblasts³⁰, and glial cells³¹. There are also areas in which the nanoFET probes are currently limited compared to patch-clamp technology, including the capability to deliver molecular and/or macromolecular reagents. Last, we believe that our approach could be scaled up in the future to make these novel 3D nanoelectronic probes accessible to a broad range of users in electrophysiology, bioelectronics and related fields.

5.5 Bibliography

1. Parpura, V. *Nature Nanotech.* **7**, 143 (2012).
2. Spira, M. & Hai, A. *Nature Nanotech.* **8**, 83 (2013).
3. Duan, X., Fu, T. M., Liu, J., & Lieber, C. M. *Nano Today* **8**, 351 (2013).
4. Dunlop, J., Bowlby, M., Peri, R., Vasilyev, D. & Arias, R. *Nature Rev. Drug Discov.* **7**, 358 (2008).
5. Molleman, A. *Patch Clamping: An Introductory Guide to Patch Clamp Electrophysiology*. (Wiley, New York, 2003).
6. Sakmann B. & Neher E. *Single-channel recording*. (Plenum Press, New York, 1995).
7. Xie, C., Lin, Z., Hanson, L., Cui, Y. & Cui, B. *Nature Nanotech.* **7**, 185 (2012).
8. Robinson, J. T. *et al.* *Nature Nanotech.* **7**, 180 (2012).
9. Hai, A., Shappir, J. & Spira, M. E. *J. Neurophysiol.* **104**, 559 (2010).
10. Tian, B. *et al.* *Science* **329**, 830 (2010).
11. Jiang, Z., Qing, Q., Xie, P., Gao, R. X. & Lieber, C. M. *Nano Lett.* **12**, 1711 (2012).

12. Duan, X. J. *et al. Nat. Nanotech.* **7**, 174 (2012).
13. Gao, R. X. *et al. Nano Lett.* **12**, 3329 (2012).
14. Morales, A. M. & Lieber, C. M. *Science* **279**, 208 (1998).
15. Tian, B., Xie, P., Kempa, T. J., Bell, D. C. & Lieber, C. M. *Nat. Nanotech.* **4**, 824 (2009).
16. Xu, L. *et al. Nano Lett.* **13**, 746 (2013).
17. Li, B., Liu, M. & Chen, Q. *J. Micro/Nanolith. MEMS MOEMS.* **4**, 043008 (2005).
18. Tian, B. *et al. Nat. Mater.* **11**, 986 (2012).
19. Bers, D. M. *Nature* **415**, 198 (2002).
20. Zipes, D. P. & Jalife, J. *Cardiac Electrophysiology: From Cell to Bedside.* (Saunders, Philadelphia, ed. 2, 2009).
21. Chernomordik, L. V. & Kozlov, M. M. *Nat. Struct. Mol. Biol.* **15**, 675 (2008).
22. Nicolas, J., Mura, S., Brambilla, D., Mackiewicz, N. & Couvreur, P. *Chem. Soc. Rev.* **42**, 1147 (2013).
23. Subbiah, R., Veerapandian, M., & Yun, K.S. *Curr. Med. Chem.* **17**, 4559 (2010).
24. Kotov, N. A. *et al. Adv. Mater.* **21**, 3970 (2009).
25. Hai, A., Shappir, J. & Spira, M. E. *Nature Methods* **7**, 200 (2010).
26. Szentandrassy, N. *et al. Curr. Med. Chem.* **18**, 3737 (2011).
27. Viatchenko-Karpinski, S. *et al. Proc. Natl. Acad. Sci. USA* **96**, 8259 (1999).
28. Davie, J. T. *et al. Nat. Protocols* **1**, 1235 (2006).
29. Akbarali, H. I., Wyse, D. G. & Giles, W. R. *Circ. Res.* **70**, 536 (1992).
30. Chilton, L. *et al. Am. J. Physiol. Heart Circ. Physiol.* **288**, H2931 (2005).
31. Clark, B. A. & Mobbs, P. *Eur. J. Neurosci.* **6**, 1406 (1994).

Chapter 6. Kinked p-n junction nanowire probes for localized cell stimulation

6.1 Introduction

To fully unveil the function and connection of cells in a tissue and to solve scientific challenges like mapping neuronal circuits in the brain, both cellular electrical recording and stimulation tools are essential¹⁻². Recently, nanoelectronic devices interfacing with biological systems have led significant progress in the studies of electrophysiological behavior at the cell and tissue levels³⁻¹⁵, including multielectrode array (MEA)^{4,7-9}, semiconductor nanowire FET^{5,10-14} and optogenetic based devices¹⁵. However, multifunctional probes that can both stimulate and record action potentials with sub-cellular spatial resolution and minimal invasiveness have not yet been demonstrated for several reasons. First, although metal based devices are easier to scale up and achieve stimulation with current injection method similar to the traditional patch-clamp, their size cannot be reduced to the nanoscale without significantly degrading the signal and bandwidth⁷⁻⁹, and thus limiting their spatial resolution. Second, although simple transistor or diode based devices have the advantages of minimal invasiveness and sub-cellular spatial resolution recording¹⁰⁻¹⁴, stimulation functionality has only been demonstrated on large devices by capacitive coupling¹⁶⁻¹⁷, which has diminishing effectiveness when shrunk in size. Finally, optogenetic method lacks cell specificity and localized influence¹⁵.

In these regards, nanoscale p-n diodes have advantages as they have different operational modes for differing functions: (1) in forward bias, an FET-like localized voltage sensor¹² and (2) in reverse bias, a nanoscale capacitor with localized electric field.

Recently, we demonstrated the synthesis, characterization and intracellular recording of Si p-n kinked nanowires¹². These nanowires can be rationally synthesized with controllable p-n junction length and position¹². In this chapter, we report the localized stimulation of voltage-gated ion channels with Si based p-n kinked nanowire probes, which combined with their FET-like recording function can achieve a complete tool for electrophysiology study with sub-cellular resolution.

6.2 Experimental

6.2.1 Kinked p-n nanowire synthesis

Kinked p-n silicon nanowires were synthesized by CVD through a gold nanoparticle-catalyzed VLS process as described previously^{12,18,19}. Specifically, 100 nm diameter gold nanoparticles (Ted Pella) were dispersed on Si substrates with 600 nm SiO₂ (Nova Electronic Materials, Flower Mound, TX). Growth of heavily boron-doped p-type arm was first carried out by feeding SiH₄ (1 sccm), B₂H₆ (10 sccm, 100 ppm in H₂), and H₂ (60 sccm) into the system for 15 min at a total pressure of 40 Torr and temperature of 450 °C. The growth was then paused for 15 s by rapidly evacuating the chamber to lowest pressure and shutting off the gas lines. SiH₄ (1 sccm), PH₃ (4 sccm, 1000 ppm in H₂), and H₂ (60 sccm) were then flown into the system at the same total pressure and temperature to grow a heavily doped n-type section for 30 s, forming the p-n junction. A second evacuation of 15 s followed, and finally the heavily doped n-type arm was allowed to finish in additional 15 min. This results in a ~200 nm long p-n junction¹². An intrinsic section can be synthesized between the p-arm and n-arm by feeding only SiH₄ (1 sccm) and H₂ (60 sccm) for 30 s to create a ~550 nm long p-n junction.

6.2.2 COMSOL multiphysics simulation

The simulation was performed by means of COMSOL Multiphysics finite-element-based electromagnetics solver (software version 4.2). We modeled the silicon nanowire as a cylinder with diameter 100 nm and p-n junction depletion region length 200-800 nm. The material of nanowire was chosen as standard solid Si from COMSOL material library. The arms of the nanowire were modeled as metallic doped Si, while the p-n junction depletion region was modeled as semiconductor intrinsic Si. On the surface of Si nanowire, a layer of 0.5 nm thick SiO₂ with dielectric constant 3.9 was added from COMSOL material library. The aqueous solution surrounding the nanowire was modeled as dielectric constant 80 and ionic strength 100 mM. The cell membrane was modeled as a 5 nm thick dielectric layer with dielectric constant 2.5 across the center of p-n junction perpendicular to the nanowire. In the calculation, the aqueous solution was grounded at infinity. The n-type arm of the silicon nanowire was given an initial potential value of 0 V. The p-type arm of the silicon nanowire was given an initial potential value of 0~-5 V as reverse bias for stimulation.

6.2.3 Free-standing probe fabrication

Free-standing kinked nanowire probes were fabricated using PL and EBL as described previously¹¹. Key steps used in the fabrication were as follows. (1) PL and metal deposition (100 nm, Ni) were used to define an array of sacrificial layer blocks on a Si substrate with 600 nm SiO₂ surface layer (Nova Electronic Materials, Flower Mound, TX). (2) Bottom passivation layer and main body of the probes was fabricated by spin coating SU8 2002 (2 μm, MicroChem) followed by PL. (3) Contact pads and interconnects to the tip region were patterned by PL, metal evaporation and lift-off (Cr/Au, 5/200 nm) on top

of the bottom SU8 of the probe body. (4) 500 nm thick layer of SU8 2000.5 (MicroChem) was deposited by spin coating, pre-baked at 65 °C for 2 min, and then kinked Si-nanowires dispersed in ethanol solution were deposited in the region near the end of each probe structure. (5) Chosen nanowires were immobilized on the surface by electron-beam irradiation of the SU8 in this region and post-baking (75 °C for 2 min) to yield a continuous SU8 passivation layer from the probe body defined by PL to the arms of the kinked nanowire. (6) Metal contacts linking the arms of the kinked nanowires to the larger PL-defined probe interconnects were defined by EBL and metallization (Cr/Pd/Cr, 1.5/120/60 nm) on the SU8. (7) Another 500 nm thick SU8 layer was deposited and patterned by EBL to passivate the metal contacts to the kinked nanowire arms while leaving the kinked nanoprobe exposed. (8) A 50 µm thick layer of low stress SU8 with SiO₂ nanoparticles (GLM 2060, Gersteltec) was patterned by PL as top passivation layer for the 4.5 mm long main body of the probe, and then post-baked at 57 °C for 3 h before development and final hard baking. (9) Last, 300 and 500 nm thick layers of LOR 3A and S1805 (MicroChem) were deposited by spin-coating on the surface, and a small region covering the nanowire tip end was defined by PL. (10) The probe was released from the substrate by etching the Ni layer (40% FeCl₃:39% HCl:H₂O=1:1:20) in a small petri-dish, and then the solution was exchanged with deionized water. (11) The resulting probe body was manually removed from the solution with tweezers, and then aligned and glued (Devcon 5-minute epoxy, ITW) to a printed circuit board connector (PCB_A16, NeuroNexus) on top of a 4 mm long, 15 µm thick silicon lever (raw A-style probe, NeuroNexus). (12) The metal pads on the probe and printed circuit board connector were electrically-connected using silver epoxy

(E415G, Epoxy Technology), cured at 55 °C for 3-4 h, and subsequently passivated with silicone elastomer (Kwik-Sil adhesive, World Precision Instruments).

6.2.4 CHO cell culture

Cryopreserved CHO cells with Nav 1.4 ion channels (Human Nav 1.4-CHO EZCells, ChanTest) were first quickly thawed in a 37 °C water bath. The cells were then transferred to a 15 ml conical tube with 10 ml media (Ham's F-12 nutrient mix, Life Technologies; with 10 vol.% fetal bovine serum) and centrifuged to remove DMSO. The centrifuged cells were dispersed into 20 ml media and seeded onto polylysine (0.5-1.0 mg/ml, MW 70,000 – 150,000, Sigma-Aldrich) coated glass cover-slips at an initial cell density of $1 \times 10^5 \text{ cm}^{-2}$. The culture was maintained at 37 °C with 5% CO₂ for 2-3 hours before electrical measurements. All the procedures conformed to US National Institutes of Health guidelines and were approved by Harvard University's Animal Care and Use Committee.

6.2.5 Brain slice preparation

Thalamocortical slices (300–500 μm) containing barrel cortex were prepared from C57BL/6 mice (postnatal day 8-14) with a vibratome (VT 1000S) using standard procedures²⁰. Slices were prepared in ice-cold artificial CSF (aCSF) containing (in mM) 83 NaCl, 2.5 KCl, 3.3 MgSO₄, 1 NaH₂PO₄, 26.2 NaHCO₃, 22 glucose, 72 sucrose, and 0.5 CaCl₂, and equilibrated with 95% O₂/5% CO₂. Slices were allowed to recover for 40 min at 37 °C and at room temperature (21–23 °C) thereafter. All physiological recordings were performed within 10 h of slice preparation. All animal procedures conformed to US National Institutes of Health guidelines and were approved by Harvard University's Animal Care and Use Committee.

6.2.6 Patch-clamp recording

Patch pipettes were pulled from 1.5 mm diameter boron glass tubes (P-97 Flaming/Brown Micropipette Puller, Sutter Instruments). Pipettes were filled with intracellular medium (in mM, potassium gluconate 125, KCl 20, CaCl₂ 0.5, MgCl₂ 2, HEPES 10, EGTA 5, Na₂-ATP 2, pH 7.3), and the resistance was measured with 5 mV pulses to be ~7 MΩ. After a gigaohm-seal was formed, the pipette was held at -70 mV before breaking the membrane to form a whole-cell patch. The data were recorded in voltage-clamp mode with sampling rate of 20 kHz using Digi1440A and Clampex 10 software (MDS).

6.2.7 Intracellular recording and stimulation

A free-standing p-n nanowire probe was first exposed in ultraviolet light (430 nm, 120 s) to sensitize the photoresist protection layer before it was mounted on a micromanipulator (MP285, Sutter Instrument) for control during experiments. The probe tip was then immersed in deionized water in a petri-dish, followed by developer solution (MF-CD-26, MicroChem), which dissolved the protection on the tip. The solution was changed to 1× PBS for 1 h, and then incubated for 2 h with 1 mg/ml lipid vesicles of 1,2-dimyristoyl-sn-glycero-3-phospho- choline (DMPC, Avanti Polar Lipids Inc.) containing 1% 1-myristoyl- 2-{12-[(7-nitro-2-1,3-benzoxadiazol-4-yl) amino] dodecanoyl}-sn-glycero-3-phosphocholine (NBD-lipid, Avanti Polar Lipids Inc.) as fluorescent reporter. As described previously, this latter step yields lipid layers on the nanowire surface¹⁰. Last, the solution was changed to Tyrode solution (in mM, NaCl 138, KCl 4, CaCl₂ 2, MgCl₂ 1, Na₂HPO₄ 0.33, HEPES 10, glucose 10, pH 7.4), and CHO cell samples were introduced at room temperature. A fixed forward 1 V voltage was applied between the source and drain

of the probe (Axon Digi1440A, Molecular Devices) for recording. The resulting current was input to a current/voltage preamplifier (Model 1211, DL Instruments) at sensitivity of 10^{-6} A/V, low-pass filtered (0–3kHz, CyberAmp 380, Molecular Devices) and digitized at 20 kHz sampling rate (Axon Digi1440A, Molecular Devices). An Ag/AgCl reference electrode was used to fix the extracellular solution potential at a constant value of 0 V in all recording experiments. Reverse bias voltage was applied between the source and drain of the probe (Axon Digi1440A, Molecular Devices) for stimulation measurement.

6.2.8 Confocal imaging

A confocal fluorescent microscope (FV1000, Olympus) was used to image the fluorescence intensity of di-8-ANEPPS voltage sensitive dye (Life Technologies) coated CHO cells during p-n nanowire probe stimulation measurement. Real-time fluorescent images of the cells were captured with a data rate of ~ 1 Hz using a 473 nm laser to excite the dye. A channel with a filter of 575–675 nm was recorded as an indication of cross membrane potential. Image analysis was done by selecting and averaging the images scanning over the stimulated cell within ~ 10 ms of the onset of stimulation.

6.3 Results and discussion

6.3.1 Kinked p-n junction nanowire for localized stimulation

As shown in the schematics (**Fig. 6-1a**, left), in reverse bias, a p-n kinked nanowire can generate localized electric fields within and around the p-n junction, with a similar configuration to a parallel capacitor. When the junction is internalized by a cell and positioned across the cell membrane, the electric field can induce a potential difference across the membrane and subsequently activate voltage-gated ion channels, such as Na^+

channels, on the membrane. The opening of Na⁺ channels can induce inward current and further polarize the cytosol, which might generate action potentials in excitable cells such as neurons or cardiomyocytes. In this way, an inward current peak and/or action potential of the excitable cells can be generated and controlled by reverse bias pulses applied to the p-n device (**Fig. 6-1a**, right). The amplitude and localization of the electric field is readily controlled by the amplitude of reverse bias. The mechanism of stimulation with p-n kinked nanowire is fundamentally different from current injection and has the advantages of (1) no direct solution exchange with cytosol and (2) the capability for down scaling the stimulated area by the probe.

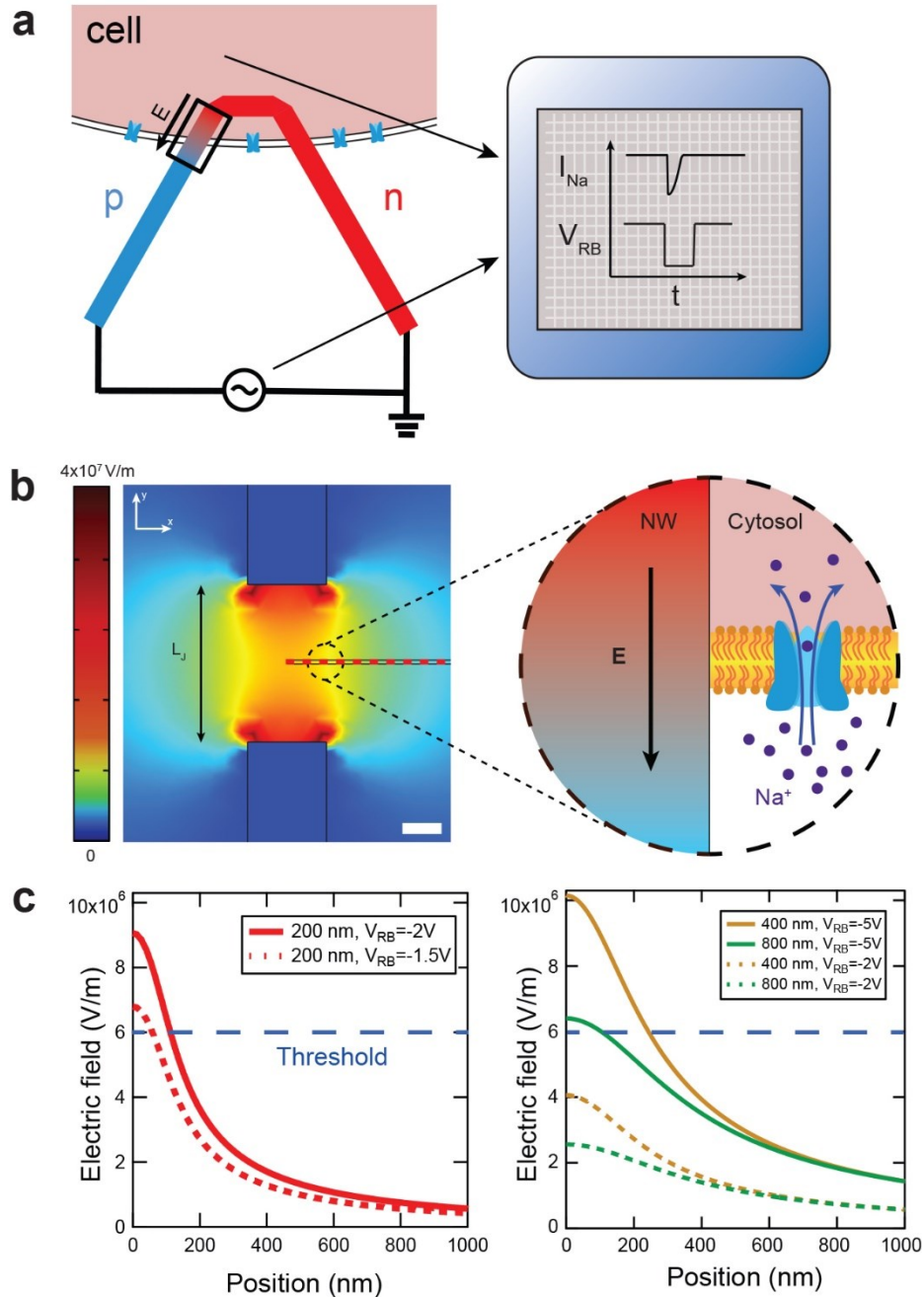


Figure 6-1. p-n junction kinked nanowire for localized stimulation. **a**, p-n kinked nanowire probes can work as nano-stimulators in reverse bias and induce Na^+ current with V_{RB} pulse. Gradient color segment highlights reverse biased p-n junction. Black arrow highlights electric field direction. **b**, (Left) Simulation plot of electric field amplitude along y-direction (E_y) around p-n junction as shown in the black box for a p-n kinked nanowire with junction length 200 nm and $V_{\text{RB}}=-2\text{V}$. L_J marks the length of the p-n junction. Scale bar: 50 nm. (Right) Schematics of activation of Na^+ ion channel with electric field from p-n nanowire. **c**, (Left) Line profiles along the red dashed line in **b** for 200 nm junction and reverse bias amplitudes of -2 V (red line) and -1.5 V (dashed red

(Continued) line). Blue dashed line highlights the threshold of amplitude to activate Na⁺ channels. (Right) Line profiles for different junction lengths at different reverse bias amplitudes. Blue dashed line highlights the threshold of amplitude to activate Na⁺ channels.

We used finite-element-based electromagnetics solver to simulate the electric field generated by reverse biased p-n kinked nanowire at the onset of the pulse (**Fig. 6-1b,c**). The 2D mapping of electric field amplitude in y-direction under -2 V reverse bias (**Fig. 6-1b**) shows several features: (1) electric field is generated not only within but also around the kinked nanowire, which can activate Na⁺ channels on the membrane close to the nanowire; (2) the electric field is localized around the p-n junction, no field leaking through nanowire arms; (3) the amplitude of the field decays quickly with increased distance from the nanowire. Line profiles along the simulated position of membrane are plotted in **Fig. 6-1c** for different reverse bias amplitudes and p-n junction lengths to study the dependence of electric field amplitude on these two parameters. For 200 nm long p-n junction that we used for cell stimulation in this chapter, the line profiles (**Fig. 6-1c**, left) show that -2 V reverse bias can generate electric field large enough to create over 30 mV potential change across membrane needed to activate Na⁺ ion channels²¹ and the stimulation threshold for V_{RB} is between -1.5 V and -2 V. Line profiles for different junction lengths (**Fig. 6-1c**, right) show the trend that under the same V_{RB} , longer junctions induce weaker electric field and thus require larger stimulation threshold (~-5V for 800 nm junction). We note that shorter junction has the advantages of lower stimulation threshold and more localized electric field.

6.3.2 Device fabrication and characterization

Si kinked p-n nanowires with 80-100 nm diameter and ~200 nm junction length were synthesized and fabricated into free-standing probes using methods discussed in previous work¹¹⁻¹². Free-standing probe configuration has the advantage of high resolution targeting and the capability of working together with patch-clamp on the same cell to examine the cell response to stimulation. A representative optical image (**Fig. 6-2a**) shows the resulting free-standing probe with a p-n kinked nanowire at the tip in solution. To characterize the electrical performance of the device, I-V data were measured both in the dry state and in PBS solution. Typical dry state I-V from -5 V to +5 V show clear rectification with no junction breakdown in reverse bias and an onset of current flow of 0.6 V in forward bias (**Fig. 6-2b**). I-V in solution (**Fig. 6-2c**) from -2 V to +2 V shows similar result with no leakage or breakdown. Representative conductance versus water-gate potential data recorded in PBS solution (**Fig. 6-2d**) yield a sensitivity of 294 nS/V. To study the limit of reverse bias amplitude that can be applied to the probe, detailed high-resolution I-V measurement in reverse regime was carried out. A representative result of 200 nm junction device shown in **Fig. 6-2e** demonstrates that reverse bias up to ~-3 V can be applied without leakage, which is enough for the activation of Na⁺ ion channels according to simulation. We note that the leakage at ~-3 V in solution could only be attributed to leakage of SU8 passivation of probe or SiO₂ passivation of p-n junction, and not the reverse breakdown of p-n junction because the dry state I-V showed that it did not happen up to -5 V. To further study the cause of leakage and the corresponding electric field amplitude, we performed reverse bias measurement on p-n kinked nanowires with two different junction lengths of 200 nm and 550 nm and compared the breakdown voltage in the plotting of **Fig. 6-2f**. The results show that: (1) the breakdown voltages for 550 nm

junctions ($-7.80 \text{ V} \pm 0.78 \text{ V}$, $N=3$) are much higher than 200 nm junctions ($-2.38 \text{ V} \pm 0.79 \text{ V}$, $N=3$), and (2) the linear fitting between junction length and breakdown voltage (**Fig. 6-2f**) agrees with SiO_2 breakdown condition in literature²²⁻²³ at the highest electric field amplitude point in simulation (**Fig. 6-2e**, inset). These two features show that the reverse bias breakdown is not due to SU8 leakage but probably rather due to SiO_2 breakdown leakage. We note that higher reverse bias limit could be achieved with better oxide coating and passivation of nanowire²⁴.

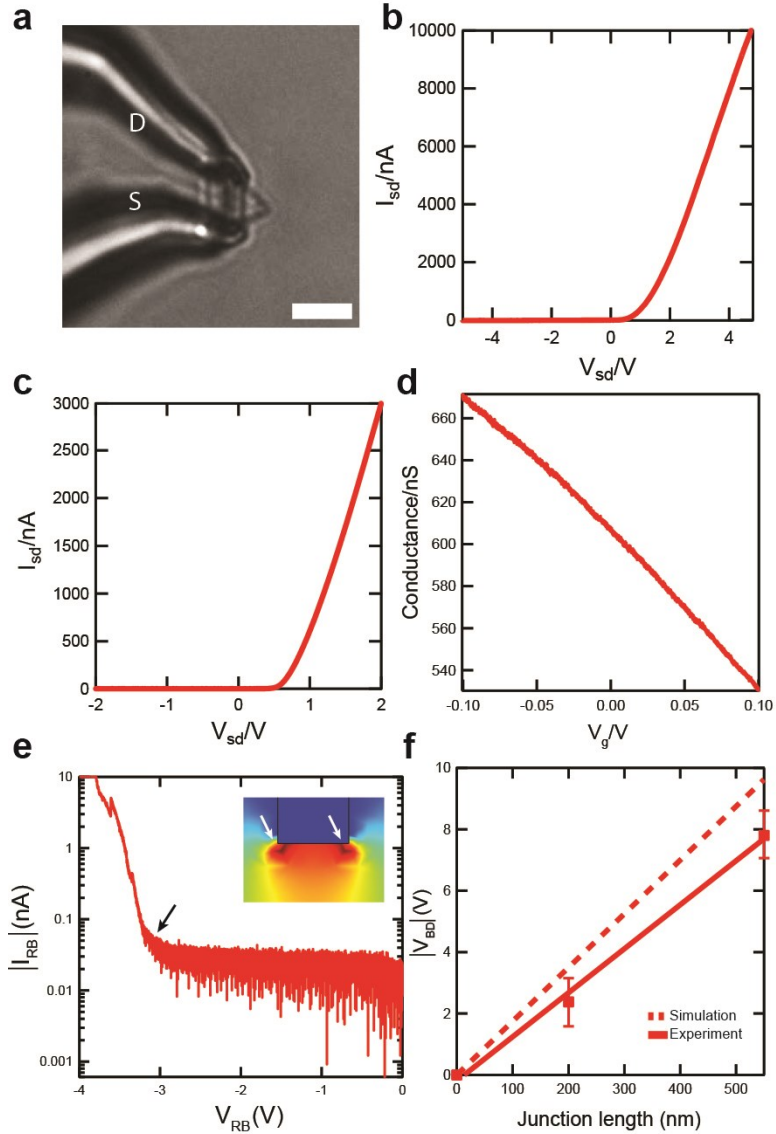


Figure 6-2. p-n kinked nanowire freestanding probe characterization. **a**, Differential interference contrast image of a p-n kinked nanowire freestanding probe in solution. Scale bar: 10 μ m. **b**, I-V data from a representative p-n probe at dry state. **c**, I-V data from a representative p-n probe in solution. **d**, Conductance versus water-gate potential data for a typical free-standing p-n nanowire probe recorded with forward bias of 1 V. **e**, Reverse bias performance from a representative p-n probe in solution. Black arrow highlights the breakdown of SiO₂. Inset: the simulation plot with highest electric field on the nanowire surface where SiO₂ breakdown is mostly likely to happen, the white arrows highlight the highest field spots. **f**, Experimental and simulation results of breakdown voltage versus junction length. Red dashed line is simulation result, red data points and solid line fitting are experimental results.

6.3.3 Localized stimulation on CHO cells

The schematics in **Fig. 6-3a** illustrate the procedure we used to interrogate live CHO cells with free-standing p-n probes. First, the p-n kinked nanowire operating at 1 V forward bias as a p-type FET¹² was manipulated to form a gentle contact with the cell membrane (**Fig. 6-3a**, I). Second, we approached the probe very slowly to facilitate the internalization of the kinked nanowire until the recording of half full-amplitude resting potential from the p-n probe was observed, which corresponds to the positioning of the p-n junction across the membrane (**Fig. 6-3a**, II). Third, reverse bias pulses with 15 ms duration and different amplitudes were applied to the p-n device to activate the Na⁺ ion channels on the membrane (**Fig. 6-3a**, III). The sensitivity of the p-n probes was characterized before cell measurements so that recorded resting potential data could be calculated as potential values.

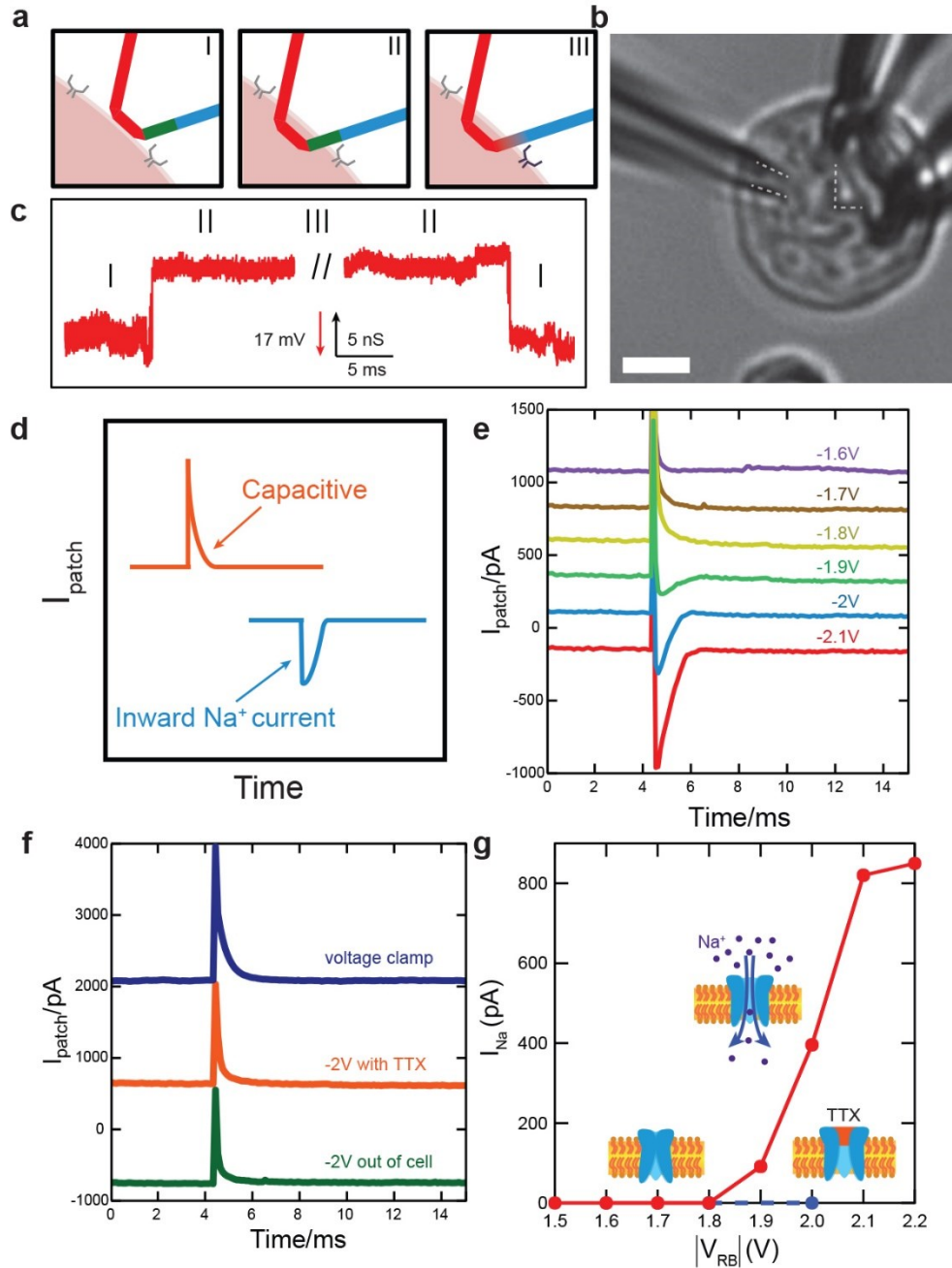


Figure 6-3. Localized stimulation using p-n kinked nanowire probes on CHO cell. **a**, Schematics of (I) p-n probe contacts a CHO cell with Na^+ ion channels (silver), (II) p-n junction partially internalized, (III) activation of Na^+ ion channels (purple) using reverse biased p-n junction when cross membrane. Green and gradient color segments highlight forward and reverse biased p-n junctions respectively. **b**, Differential interference contrast image of a p-n probe and a patch-clamp pipette on a CHO cell. The white dashed lines highlight the kinked nanowire and micropipette inner diameter. Scale bar: $5 \mu\text{m}$. **c**, Electrical recording of resting potential from a p-n junction nanowire at different stages shown in **a**. **d**, Schematics of capacitive peak compared with inward Na^+ current peak

(Continued) measured with voltage-clamp. **e**, Voltage-clamp recording of inward Na^+ current stimulated by p-n probe with different amplitude of stimulation. **f**, Control experiment traces of stimulation. **g**, Stimulated inward Na^+ current peak amplitude versus reverse bias voltage applied to a p-n probe for stimulation. Insets: schematics of closed and opened Na^+ ion channel on the cell membrane corresponding to different Na^+ current peak amplitude and experiment setup.

During the measurement, we first established a voltage-clamp holding at -70 mV on the CHO cell to monitor the responsive Na^+ inward current stimulated by the nanowire probe. Then we approached p-n probe onto the same cell as shown in a representative differential interference contrast image (**Fig. 6-3b**). The resulting conductance trace of the p-n probe is shown in **Fig. 6-3c**. The baseline corresponds to stage I, when the p-n diode is entirely out of the cell during approaching or retreating; the sharp jump up and down of conductance shows the process of internalization (stage I to stage II) or probe withdrawal from the cell (stage II to stage I), respectively. The resting potential measured by the p-n probe in stage II (**Fig. 6-3b**) is calculated as ca. -34 mV, which is half the holding potential of the voltage-clamp and it means that p-n junction is positioned across the cell membrane. During stage III, when reverse bias pulses were applied for stimulation, the conductance of the p-n probe was not measured. We note that the resting potential of the cell is stable before and after the stimulation, which shows that the cell membrane is not damaged during the process. All measurements were carried out in an inverted microscope with probes mounted in XYZ manipulators and a temperature-regulated cell medium. The kinked nanowire was coated with phospholipid layers prior to cell measurement as described previously¹⁰.

The cross membrane current signals recorded by voltage-clamp in stage III can be dissected into two components as illustrated in **Fig. 6-3d**. The capacitive peaks are induced

by the sharp onset of reverse bias pulse on the patch-clamp electrode, while inward Na^+ peaks are caused by the activation of Na^+ ion channels²⁵⁻²⁷. The voltage-clamp recording traces measured with stimulation amplitudes from -1.6 V to -2.1 V are analyzed using standard pulse protocols²⁸ and shown in **Fig. 6-3e**. The traces consist one (for -1.6 V to -1.8 V) or both (for -1.9 V to -2.1 V) of these components. The data (**Fig. 6-3e**) exhibit two key features. First, the V_{RB} threshold of stimulation is ~ -1.9 V: only with pulses above or equal to -1.9 V, inward Na^+ peak with ~ 1 -2 ms duration can be stimulated near the onset of the pulse. Second, stimulated inward current peak amplitude increases with higher V_{RB} amplitude. To confirm the nature of the signals and that the inward current peaks are indeed Na^+ signals stimulated by the probe, we conducted three control experiments as follows (**Fig. 6-3f**). First, applying voltage pulses to the patch-clamp electrode in solution resulted in similar capacitive peaks measured by voltage-clamp itself. Second, Na^+ channel blocker tetrodotoxin (TTX) was added into the solution during stage III and after that -2 V stimulation pulse could not induce inward current peaks. Third, when the p-n kinked nanowire was retreated out of the intracellular environment but still very close to the cell, -2 V stimulation pulse could not induce inward current peaks. These results confirm that: (1) the capacitive peak is due to the artifact of voltage pulse, (2) the inward current peak is signal from Na^+ ion channels and (3) the signals are stimulated by the p-n junction instead of S/D electrodes of the probe.

The relationship between stimulation pulse amplitude and stimulated Na^+ current peak amplitude is summarized and plotted in **Fig. 6-3g**. The plot shows an onset threshold at ~ -1.9 V V_{RB} and an increased stimulation amplitude with increased V_{RB} above that. The peak amplitude tends to saturate at ~ 800 pA near 2.1 V due to the limited area of electric

field. Using the conductance of a single Na^+ ion channel²¹ and the density of ion channels on the CHO cell, we can calculate the stimulated area corresponding to the ~ 400 pA current peak for -2 V pulse as $\sim 10\%$ of the cell, which demonstrates the localized nature of the stimulation.

6.3.4 Stimulation on voltage sensitive dye modified CHO cells

To further confirm the localized nature of our stimulation method, stimulation response measurements were conducted on voltage sensitive dye (VSD) modified CHO cells under confocal fluorescence microscope. The cells were first seeded on glass substrate and coated with di-8-ANEPPS VSD. The fluorescence intensity of di-8-ANEPPS dye in red channel (575-675 nm) has been demonstrated to change linearly with the cross membrane potential with sensitivity $\sim 10\%/100$ mV²⁹⁻³¹, and therefore can be used to visualize the stimulated depolarization of cell membrane. Glucose-based oxygen scavenger was added to the solution prior to measurement to reduce photo-bleaching³². After the internalization of the nanowire probe (stage II), reverse bias pulse trains with different amplitudes were applied to the probe simultaneously with confocal fluorescence imaging. The resulting averaged confocal images (**Fig. 6-4a**) show two features. First, images corresponding to reverse bias pulses with amplitudes of -1.5 V and -1.7 V (**Fig. 6-4a**) show no change in fluorescence intensity, which is the same as the case when no pulse was applied; while -1.9 V and -2 V images show a clear decrease of intensity near the kink position of nanowire probe, which corresponds to cellular depolarization. Second, the region with decreased fluorescence intensity is highly localized around the kink of nanowire and this area increases in size with increased stimulation amplitude. The intensity line profiles across the probe tip position plotted in **Fig. 6-4b** further confirm the

observations. In addition, quantitative calculations based on the line profile for -2 V stimulation show that: (1) the peak amplitude of the membrane potential change induced by stimulation is ~ 100 mV and (2) the affected area with decreased fluorescence intensity is $\sim 7\%$ of the cell. These results are consistent with the voltage-clamp measurements discussed in the last section.

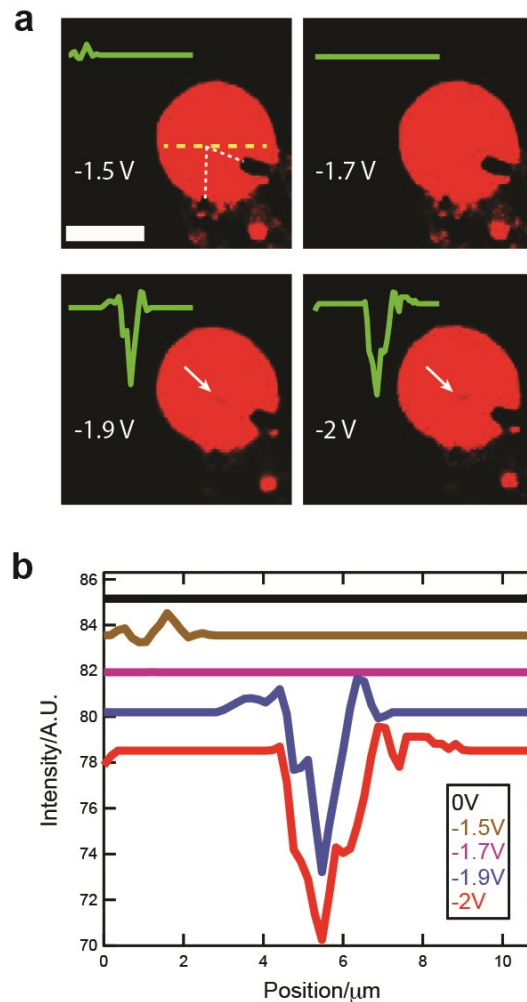


Figure 6-4. Stimulation on VSD modified CHO cells. a, Confocal images of VSD modified CHO cells and p-n probe with different reverse bias amplitudes. The position of the nanowire is registered by superimposition of the differential interference contrast image of the probe and highlighted by white dashed lines. Insets: line profiles of fluorescence intensity along yellow dashed line. White arrows highlight the stimulated

(Continued) area. Scale bar, 10 μ m. **b**, Line profiles of fluorescence intensity along yellow dashed line in **a** at different reverse bias amplitudes.

6.3.5 Stimulation of neurons

We also carried out stimulation measurements on neurons of mice brain slices. In order to further reduce invasiveness to the cell and achieve even higher flexibility, an extracellular configuration was used for stimulation without nanowire phospholipid coating (**Fig. 6-5a**). Instead of positioning the nanowire across the cell membrane, we just dimpled a neuron with kinked nanowire tip to form tight interface. Electric field at the edge of the p-n junction can penetrate across the membrane at reverse bias and function as stimulation (**Fig. 6-5a**). Similar to CHO experiments, a free-standing p-n junction kinked nanowire probe and a patch pipette were both setup on a neuron (**Fig. 6-5b**). The patch-clamp was used to monitor intracellular potential. We applied square-shaped reverse bias trains on the p-n junction with 1 ms single pulse duration at 500 Hz for 500 ms train duration. We varied the amplitude of the pulses as -0.5 V, -1 V and -1.5 V. We plotted averaged response of 5 patch-clamp traces (**Fig. 6-5c**), which show that a \sim 2 mV depolarization could be induced with -1.5 V pulse trains, while lower amplitude showed almost no response. Moreover, we observed that when the resting potential of the neuron was closer to the action potential threshold, a -1.5 V pulse train was enough to activate multiple action potential firing events (**Fig. 6-5d**). Pulse trains with -0.5 V and -1 V amplitudes still showed no response. These results highlight three key points: (1) the relationship between stimulation amplitude and response is nonlinear with a \sim -1.5 V threshold; (2) single unit neuron action potentials can be stimulated and controlled with a p-n kinked nanowire probe; (3) an extracellular non-invasive stimulation scheme is achieved. We note that higher stimulation voltage amplitude

might induce more significant effects. Additional efforts are being taken to further explore control experiments and optimization of stimulation conditions.

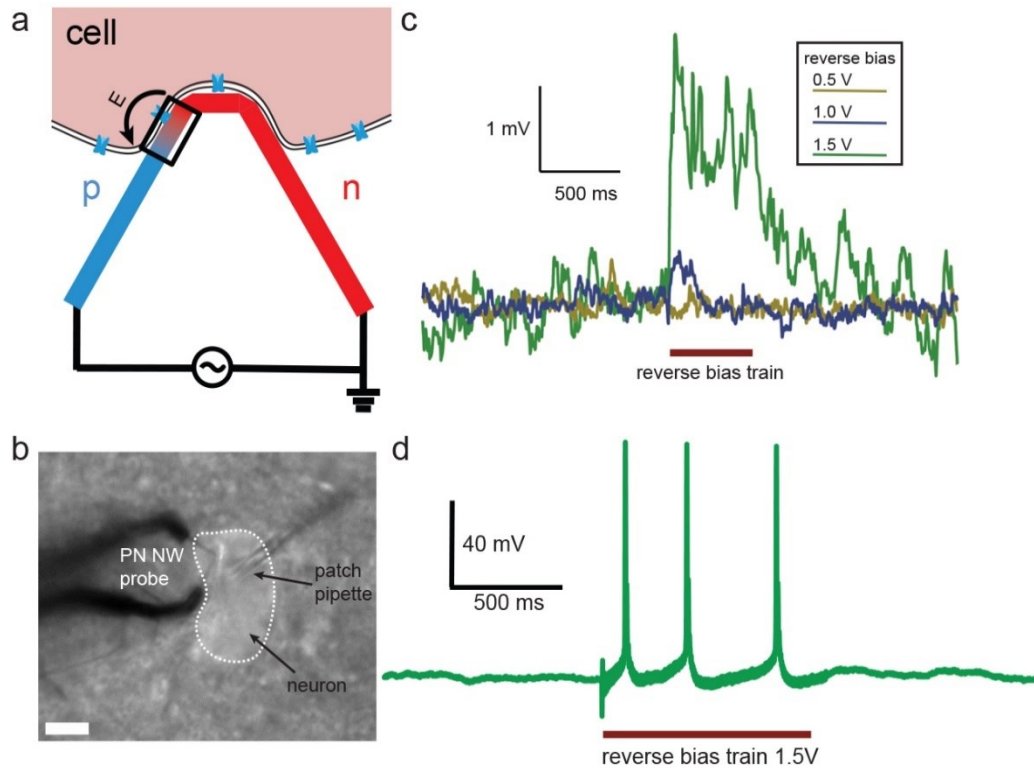


Figure 6-5. Stimulation of neurons. **a**, p-n kinked nanowire probes can also work as extracellular nano-stimulators at reverse bias when the tip dimples the cell. Gradient color segment highlights reverse biased p-n junction. Black arrow highlights electric field direction. **b**, Optical image of a p-n junction kinked nanowire free-standing probe stimulating a neuron with a patch pipette monitoring the intracellular potential. Scale bar: 10 μm . **c**, Averaged intracellular potential traces of a neuron measured by patch-clamp during p-n junction nanowire stimulation with different reverse bias amplitude. **d**, Intracellular neuron action potentials measured by patch-clamp during p-n junction nanowire stimulation.

6.4 Conclusion and outlook

We have demonstrated multifunctional bioprobes with the capability of both recording and stimulating intracellular signals using p-n kinked nanowires. Reverse biased p-n junction was shown to generate localized electric field across the membrane of CHO

cells and activate Na⁺ ion channels on the membrane. The effective stimulated area on the cells was visualized using VSD to be as localized as only ~7% of the cell membrane. Moreover, an extracellular non-invasive stimulation method was achieved to depolarize neurons and generate action potentials. These p-n kinked nanowire nano-stimulators reported in this chapter can be readily implemented into a variety of device schemes other than free-standing probes, such as on-substrate bend-up device arrays¹⁰ and flexible nanowire nanoelectronic scaffolds¹³, to study electrophysiology of different types of cells and tissues. Although additional work remains to optimize the performance of the probes, we believe that the capability of applying such localized electric fields opens up several exciting opportunities. For example, an applied electric field may yield a sustained depolarization within localized areas or neural processes, where the precision of the local field is not expected to influence multiple neurons. The ability to affect subtle details of neural firing while maintaining neural recording could be exploited for testing microcircuitry, e.g., the examination of PSP strengths. Further, it has been shown that over time microstimulation of only one or a few cells has the potential to modify behavioral output³³. Moreover, for brain machine interfaces, using nanodevices for selective stimulation could allow the brain to remap different percepts.

6.5 Bibliography

1. Alivisatos, A. P. *et al. Science* **339**, 1284 (2013).
2. Bock, D. D. *et al. Nature* **471**, 177 (2011).
3. Parpura, V. *Nature Nanotech.* **7**, 143 (2012).
4. Spira, M. & Hai, A. *Nature Nanotech.* **8**, 83 (2013).
5. Duan, X., Fu, T. M., Liu, J., & Lieber, C. M. *Nano Today* **8**, 351 (2013).

6. Dunlop, J. *et al. Nature Rev. Drug Discov.* **7**, 358 (2008).
7. Xie, C. *et al. Nature Nanotech.* **7**, 185 (2012).
8. Robinson, J. T. *et al. Nature Nanotech.* **7**, 180 (2012).
9. Hai, A., Shappir, J. & Spira, M. E. *J. Neurophysiol.* **104**, 559 (2010).
10. Tian, B. *et al. Science* **329**, 830 (2010).
11. Qing, Q. *et al. Nature Nanotech.* **9**, 142 (2014).
12. Jiang, Z., Qing, Q., Xie, P., Gao, R. X. & Lieber, C. M. *Nano Lett.* **12**, 1711 (2012).
13. Tian, B. *et al. Nat. Mater.* **11**, 986 (2012).
14. Duan, X. J. *et al. Nat. Nanotech.* **7**, 174 (2012).
15. Kim, T. *et al. Science* **340**, 211 (2013).
16. Ghezzi, D. *et al. Nature Photon.* **7**, 400 (2013).
17. Schoen, I. & Fromherz, P. *Appl. Phys. Lett.* **87**, 193901 (2005).
18. Morales, A. M. & Lieber, C. M. *Science* **279**, 208 (1998).
19. Tian, B., Xie, P., Kempa, T. J., Bell, D. C. & Lieber, C. M. *Nat. Nanotech.* **4**, 824 (2009).
20. Agmon, A. & Connors, B. W. *Neuroscience* **41**, 365 (1991).
21. Catterall, W. A. *et al. Pharmacol Rev.* **57**, 397 (2005).
22. Verweij, J. F. & Klootwijk, J. H. *Microelectronics Journal* **27**, 611 (1996).
23. Bartzsch, H. *et al. Surface and Coatings Technology* **174**, 774 (2003).
24. Zhou, W. *et al. Nano Lett.* **14**, 1614 (2014).
25. Sheets, M. F. & Hanck, D. A. *Journal of Physiology* **514.2**, 425 (1999).
26. Gellens, M. E. *et al. Proc. Natl. Acad. Sci. USA* **89**, 554 (1992).
27. Chahine, M. *et al. Am. J. Phys.* **271**, 498 (1996).
28. Molleman, A. *Patch Clamping: An Introductory Guide to Patch Clamp Electrophysiology.* (Wiley, 2003).
29. Chemla, S. & Chavane, F. *Journal of Physiology – Paris* **104**, 40 (2010).

30. Bedlack, R. S. *et al. Neuron* **9**, 393 (1992).
31. Vignali, S. *et al. Journal of Neuroscience Methods* **192**, 240 (2010).
32. Selvin, P. R. & Taekjip, H. *Single-Molecule Techniques: A Laboratory Manual*. (Cold Spring Harbor Laboratory Press, New York, 2008).
33. Houweling, A. R. & Brecht, M. *Nature* **451**, 65 (2008).